Simulation of Local Electrochemistry in Solid Oxide Fuel Cell Microstructures by High Performance Computation

Submitted in partial fulfillment of the requirements for
the degree of
Doctor of Philosophy
in
Department of Materials Science and Engineering

Yu-Ting Hsu

B.S., Department of Materials Science and Engineering, University of Illinois at Urbana-Champaign 2012

Carnegie Mellon University
Pittsburgh, Pennsylvania

March 2019

Acknowledgments

I am grateful for the support of so many colleagues and mentors here at Carnegie Mellon University (CMU). I would like to especially thank Rubayyat Mahbub, another doctoral student of the same research group, for the intellectual discussion of our solid oxide fuel cell (SOFC) research, as well as the countless tasks he has helped me with. Many important decisions regarding my research would not have been made without the guidance of Dr. Paul Salvador, Dr. Shawn Litster, and Dr. Anthony Rollett, each of whom provided his own specialized experience and knowledge that rather complement each other quite well.

External collaboration with the National Energy Technology Laboratory (NETL) has brought a new horizon for me to learn of so many other interesting projects in the field of SOFC. I would like to especially thank Dr. William Epting, a former graduate student at CMU, for his guidance when I began my doctoral research and his continued support when he graduated and transitioned to NETL.

As a significant part of this work relies on using an open-source code library (MOOSE), I would like to acknowledge the technical support from the MOOSE developers at the Idaho National Laboratory, as well as the

other computational scientists in the MOOSE community. This work used the Joule supercomputer at NETL, and the Bridges system, which is supported by NSF award number ACI-1445606, at the Pittsburgh Supercomputing Center. Jeremy Stout and Roberto Gomez have kindly assisted me with the installation/implementation of the MOOSE framework in Joule and Bridges, respectively. Finally, I want to thank Dr. Alexander Lindsay for his instructions on specific kernel implementation in MOOSE.

This work was performed in support of the National Energy Technology Laboratory's ongoing research in solid oxide fuel cells under RES contract DE-FE0004000. This project was supported in part by an appointment to the Internship/Research Participation Program at the NETL, U.S. Department of Energy, administered by the Oak Ridge Institute for Science and Education. The authors acknowledge the use of the computing workstation at Materials Characterization Facility at Carnegie Mellon University supported by grant MCF-677785. This work was also supported in part by a CMU ProSEED/EQT Foundation Grant.

The doctoral committee consists of the following members:

- Prof. Paul A. Salvador (Chair)
- Prof. Shawn Litster
- Prof. Anthony D. Rollett
- Prof. Gregory S. Rohrer
- Dr. Harry W. Abernathy

Thesis advisor: Paul A. Salvador, Shawn Litster Yu-Ting Hsu

Abstract

Recent progress in micro-scale three-dimensional (3D) characterization techniques such as focused ion beam–scanning electron microscopy (FIB-SEM) and X-ray nanotomography has brought unprecedented opportunities in linking material microstructure to performance and properties. The link between average electrode microstructure and average performance in research-grade solid oxide fuel cells (SOFCs) can be established using effective medium theory, or continuum modeling, where effective performance parameters are calculated based on effective microstructural properties. However, microstructural degradation and failure in commercial-grade SOFCs have not been adequately captured using mean parameters from effective medium theory. This work aims to quantify distributions of electrochemical parameters throughout the microstructure in heterogeneous electrodes to establish links between microstructure and degradation, failure, and performance.

In the initial stages of this work, a novel high-throughput computational methodology was developed and implemented, on which the remaining goals could be carried out. Using an open-source finite element framework (MOOSE, Idaho National Laboratory) on high performance computing platforms (Joule, National Energy Technology Laboratory, and Bridges, Pittsburgh Supercomputing Center), a numerical transport-and-reaction model was constructed and applied to morphology-preserving microstructural meshes. The model computes local distributions of electrochemical parameters that are coupled

to morphological features such as interfaces and triple phase boundaries. Using a scriptable commercial meshing software (Simpleware ScanIP), the microstructural meshes were obtained from the plasma-sourced FIB-SEM characterization of a commercial SOFC electrode, as well as synthetic microstructures generated using DREAM.3D that model specific types of heterogeneities known to exist within SOFC commercial cathodes. Results using the commercial microstructure are shown and discussed, which demonstrate the capabilities of the computational workflow and remove elements of infeasibilty for the future work.

A series of computational investigations, on both physical and synthetic microstructures, are described to correlate local microstructural features to local electrochemical performance distributions. Comparisons to conventional modeling approaches (effective medium theory, or continuum modeling) bring forth additional insight/observation capabilities unique to the novel methodology of this work. Furthermore, a synthetic infiltration algorithm was developed to model how nanoscale catalysts dispersed on the internal pore walls affect performance, to model a well-known experimental practice. The results shed light into the design and fabrication of optimal electrodes in fuel cells.

By combining physical and synthetic microstructures in simulations, specific microstructrual traits can be examined for the distributions in nano-, micro-, and meso-scale performance characteristics, providing a new framework to include in degradation model and enable more comprehensive statistical analyses/evaluations for the future work.

Contents

List of Tables

List of Figures

1 Introduction

1.1 Solid Oxide Fuel Cell Fundamentals

1.1.1 Basic Electrochemistry

Fuel cells are electrochemical devices that directly convert the chemical energy of a reaction (using fuel as the reactant) to electrical energy [91, 99]. In the simplest case, pure hydrogen can be used as the fuel, and pure oxygen the oxidant, resulting in

$$H_2 + \frac{1}{2} O_2 \longleftrightarrow H_2O \tag{1.1}$$

as the net reaction. This overall reaction is simply the hydrogen combustion reaction. But fuel cells do not involve direct combustion. Instead, the overall reaction is separated into two electrochemical half reactions: oxidation and reduction. To achieve this, the fuel and the oxidant are physically separated, as shown in Fig. 1.1.1, and the reaction energy is directly converted into electrical energy. This is an important distinction from direct

combustion. When direct combustion is used in conventional power generation, multiple conversion steps lead to indirect chemical-to-electrical energy conversion, such as a chemical-to-thermal energy conversion (e.g., combusting coal to boil water) followed by mechanical to electrical energy conversion (e.g., driving a turbine with steam). The chemical-to-electrical "shortcut" in fuel cells not only allows for high efficiency in the overall use of fuel supplies, but also reduces emission of carbon dioxide and toxic by-products that are more abundant from coal and oil combustion. Efficiency and environmental friendliness are a common driver to research and development on fuel cells.

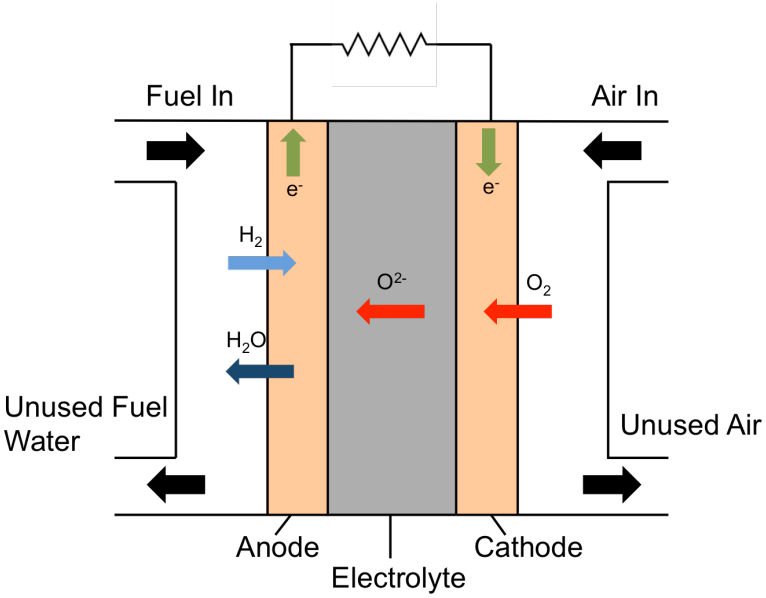

Figure 1.1.1: Schematic of a simple SOFC operation at the macroscopic scale. Arrows indicate general flux direction of the annotated species. Adapted from Fuel Cell Handbook [116].

All fuel cells consist of three primary components: anodes, cathodes, and electrolytes. There are many different types of fuel cells, the names of which are based on the electrolyte component and the ionic species that transports through the electrolyte. A solid oxide fuel cell (SOFC) consists of ceramic oxide components and conducts oxide ions through the solid electrolyte (see Fig. 1.1.1). SOFCs are of interest in distributed electrical power generation,

including chemical-to-electrical conversion, as well as combined chemical-to-electrical and chemical-to-thermal (e.g., for hot water supply) conversion. All electrochemical reactions and transport in this work will be discussed in the context of SOFCs.

At the anode, fuel is oxidized to yield electrons. Using pure hydrogen as the fuel, the hydrogen oxidation reaction (HOR) at the macroscopic scale is

$$\mathrm{H_2} + \mathrm{O^{2-}} \longleftrightarrow \mathrm{H_2O} + 2\,\mathrm{e^-}. \tag{1.2}$$

One distinctive advantage of SOFCs is fuel flexibility. A variety of hydrocarbon fuels such as natural gas, diesel reformate, and biogas can be utilized for power generation [99, 131]. In such cases, the anode electrochemistry is more complex but is beyond the scope of this work.

At the cathode, oxygen is reduced to yield oxygen ions. Macroscopically, the oxygen reduction reaction (ORR) is

$$\frac{1}{2}\,\mathrm{O_2} + 2\,\mathrm{e^-} \longleftrightarrow \mathrm{O^{2-}}. \tag{1.3}$$

The ORR is currently a focus of this work and will be thoroughly discussed with more details.

Within the electrolyte, electromigration of oxygen ions (or oxygen vacancies) takes place. SOFCs utilize an oxide material with a high oxygen conductivity (related to high oxygen vacancy concentrations) for the electrolyte component. The electrolyte also serves to separate electrically the anode and the cathode; as such, electrolytes have negligible electronic conductivity, forcing electrons to flow through an external circuit. Note that the electrolyte is designed to be dense and non-porous, which maintains physical separation of the fuel and oxidant, avoiding direct combustion.

The aforementioned HOR and ORR are only appropriate for describing the cell electrochemistry at the macroscopic scale. At the microscopic scale, the HOR and ORR may be broken down into multiple more elementary sub-reaction and transport steps.

1.1.2 Electrode Composition and Microstructure

Recall both the HOR and ORR involve a gas species, oxygen ions, and electrons. This suggests the electrochemistry at the electrodes (i.e., anode and cathode) is inherently complex. For optimal performance,[1] three rules apply to an electrode. An electrode needs to

- allow facile transport rate of gas molecules, ions, and electrons concurrently,
- allow sufficient, direct percolation of all three species from supply sites to reaction sites,
- and maximize the number of reaction sites within the electrode volume.

As such, a typical electrode contains multiple highly interconnected phases with fine morphological features at the micro-scale. This characteristic is related to two aspects of the electrodes: composition and microstructure.

The chemical composition of an electrode is important for a cell's baseline performance. For example, electronic transport requires the presence of a metallic conductor. Without a proper composition, an electrode may not conduct gas, ions, or electrons at all. An electrode may consist of three or two phases for species transport. In a three-phase electrode, the phases are the gas conducting phase (GCP), the ion conducting phase (ICP), and the electron conducting phase (ECP). In a two-phase electrode, the phases are the GCP and the mixed-ionic-and-electronic-conductor (MIEC) phase. Note that the best GCP is essentially a void space, or a pore. Table 1.1.1 lists some of the state-of-the-art materials for typical SOFC components in the context of a three-phase electrode.[2][3]

[1] Here, performance may refer to, macroscopically, a cell's capability to output electrical current/voltage at a given voltage/current state. In other words, at a constant voltage, higher current is considered better performance. Conversely, at a constant current, higher voltage is considered better performance.

[2] LSM: Strontium-doped Lanthanum Manganite, or $La_{1-x}Sr_xMnO_{3-\delta}$. LSCF: Lanthanum Strontium Cobalt Ferrite, or $La_{1-x}Sr_xCo_{1-y}Fe_yO_{3-\delta}$. YSZ: Yttria-stabilized Zirconia, or $Zr_{1-y}Y_yO_{2-y/2}$. GDC: Gadolinium-doped Ceria, or $Ce_{1-x}Gd_xO_{2-\delta}$.

[3] Under certain conditions, some cathode materials (especially LSCF) exhibit observable ionic and electronic conductivities and may be considered as MIECs.

Table 1.1.1: Notable state-of-the-art materials for SOFC components

	Cathode	Electrolyte	Anode
ECP	LSM, LSCF	-	Ni
ICP	YSZ, GDC, LSCF	YSZ, GDC	YSZ
GCP	Pore	-	Pore

An electrode's microstructure is equally important to, if not more than, its chemical composition. The term *microstructure* here refers to the physical morphology of an electrode at the micro-scale. While an electrode's composition governs baseline transport rate, its microstructure governs the effect of morphology on transport rate and reaction kinetics. For example, a large, straight pore channel would allow for faster oxygen gas diffusion and any associated reaction kinetics than a thin, tortuous pore channel would. For a three-phase electrode, designing the microstructure for fast ionic, electronic, and gas conduction while maintaining a high number of reaction sites becomes non-trivial. As previously mentioned, typical electrode microstructures are complex, containing highly interconnected phases and dense, fine morphological features across the micro-scale. This complexity is illustrated in Fig. 1.1.2 (from Fig. 3 of the work by Epting et al. [26]),[4] which shows three-dimensional microstructures of a commercially manufactured SOFC. Many of the technical terms mentioned in the caption will be introduced in later sections. For now, the figure serves to demonstrate the complexity of SOFC microstructures. This complexity largely impacts the local electrochemistry (i.e., performance) [2].

1.2 SOFC Microstructure

1.2.1 Three-dimensional Characterization Techniques

Understanding the complexity of the electrode microstructures is key to understanding the local electrochemistry within the electrodes. Characterizing and quantifying the electrode microstructures is currently an active research

[4]The microstructures shown here are one example of the characterized SOFC microstructures in the literature. Other works will be mentioned in a later section.

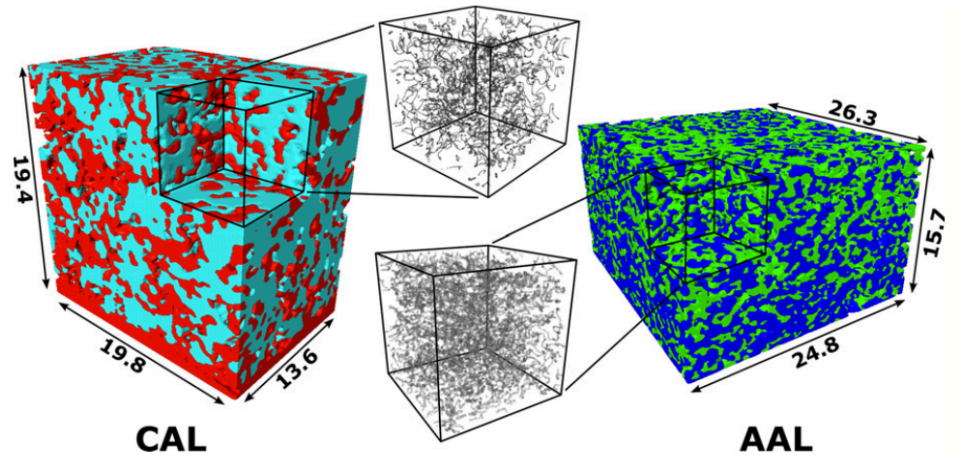

Figure 1.1.2: Three-dimensional rendering of segmented SOFC microstructures characterized by X-ray nanotomography (from the work by Epting et al. [26]). Volume dimensions are shown in μm. CAL denotes cathode active layer. AAL denotes anode active layer. The cut-out volumes show spatial distribution of triple phase boundaries. For the CAL, red is LSM and cyan is YSZ. For the AAL, green is nickel and blue is YSZ. The pore phase is transparent. Many of the technical terms mentioned here will be introduced in later sections.

field. Recent progress in micro-scale three-dimensional (3D) characterization techniques, such as focused ion beam–scanning electron microscopy (FIB-SEM) and X-ray nanotomography, has allowed new opportunities in studying material properties and performance with respect to the 3D microstructure.[5] Such techniques are especially useful for the study of SOFCs, whose electrode microstructures are necessarily complex, as discussed earlier. In fact, key microstructural features of three-phase electrodes (discussed in a later section) are only clearly manifested through 3D characterization with nano-scale resolution. As such, the 3D electrode microstructure serves as the foundation for understanding SOFC electrochemistry and transport kinetics at the micro-scale.

The 3D characterization techniques discussed here refer to imaging methods that aim to capture intensity-based phase (chemical composition) con-

[5]Works involving gallium FIB serial sectioning include, but are not limited to [16, 22, 23, 37, 51, 54, 56, 57, 61, 63, 87–89, 95, 96, 106, 110, 118, 123, 124]. Works involving X-ray nanotomgraphy include, but are not limited to [13, 18, 26, 38, 41, 60, 69, 77, 81, 95, 109, 110, 117].

trast. The result of the characterizations is a 3D reconstruction of image data, which consists of voxels of grayscale intensity. A voxel is essentially a volumetric pixel. Each voxel holds a physical dimension and an intensity value that corresponds to the signal intensity from the detector of the imaging instrument. The variation of the grayscale intensity in the voxels represents phase contrast. For example, dark gray may represent a pore in an SEM micrograph, light gray an LSM phase, and white a YSZ phase.

The image data, in grayscale form, is segmented to produce a spatial distribution of different phases. Segmentation refers to image processing techniques that partition the grayscale intensity distribution into phase distributions. This process assigns each voxel of the reconstructed image to a phase/composition. As such, a segmented 3D reconstruction consists of voxels that hold a physical dimension and phase value. Most of the microstructure properties that are discussed in the literature are quantified from segmented reconstructions.

1.2.2 3D Microstructure Properties

Some of the commonly reported SOFC microstructure properties are introduced below. The word *parameter* is used interchangeably with the word *property*. Note that these properties are discussed in the context of 3D characterizations. In other words, they are quantified from voxelized, segmented reconstruction data.

The *volume fraction* is simply the volume of a constituent phase divided by the total volume of a multi-phased microstructure. The value of a volume fraction ranges from 0 to 1. It is one of the most common and straightforward quantities measured from an SOFC microstructure. The volume fraction of a given phase needs to exceed a percolation threshold to ensure species percolation through a microstructure volume. For example, a 3D simple cubic lattice with six-connectivity (six nearest neighbors) has a percolation threshold of about 0.31 [120].

The *triple phase boundary* (TPB) is the intersection of all the three phases (GCP, ECP, and ICP) in a three-phase electrode. Geometrically, the TPBs are curved lines in a 3D volume. Given a characterized microstructural vol-

ume, the TPB density is often defined as the measured TPB line length divided by the total volume, expressed in the unit of $\mu m/\mu m^3$. The importance of the TPBs can be explained with a simple example; given a three-phase electrode, where the GCP, ECP, and ICP only conduct oxygen gas, electrons, and oxygen ions, respectively, the ORR can only take place at the TPBs, where the three reaction species come into close contact with one another. Thus, the TPB density is a measure of the potential electrochemical activity of a given microstructure. Fig. 1.2.1 illustrates examples of TPBs in a two-dimensional (2D) image of a three-phase microstructure. Note that the TPBs appear to be points in the 2D image, but are lines in 3D space. As discussed later, the TPBs may not be the only reaction sites for the HOR/ORR, especially if the cathode contains an MIEC phase [50, 75, 105].

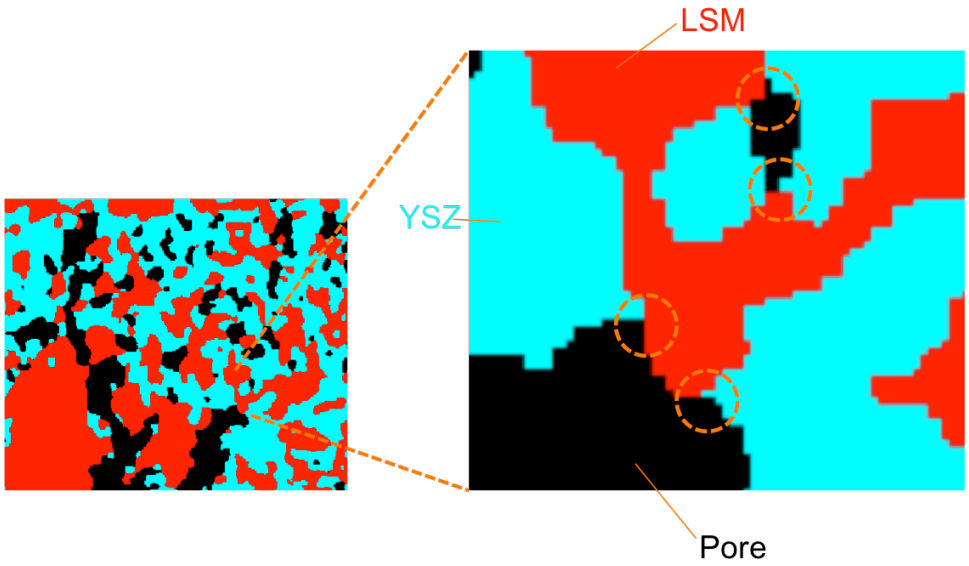

Figure 1.2.1: Image of an example of a three-phase electrode microstructure containing TPBs. The TPBs are circled in the magnified region on the right.

The *surface area* is usually referenced with respect to the interfacial area between two specific phases (e.g., GCP and ECP) or sometimes to the total interfacial area bounding an individual phase. Surfaces adjacent to the TPB

in a three-phase electrode may be important to specific sub-steps in the overall reaction, but are sometimes ignored. In an electrode containing an MIEC, the GCP/MIEC surface area represents an important reaction site for the ORR because all three reactants are present. In a three-phase electrode with an MIEC, the TPB and 2PB reactions contribute in parallel to the ORR. In a two-phase electrode with an MIEC, the presence of TPBs is largely absent (except at the MIEC/electrolyte interface[6]), and the 2PB surfaces are the the primary reaction sites. Surface areas are usually reported as the surface area per unit volume of electrode.

The *particle size* usually refers to the diameter of particles (or grains) of a specific phase in a given microstructure. The qualitative definition of the particle size is built upon the understanding that the electrodes are fabricated by sintering ceramic or composite powders of specific initial particle sizes. The particle size is often used to normalize the size of a characterized volume for comparisons to other microstructural data having different particle sizes. For example, a cubic microstructure volume may have an edge length of $L = 9.7d$, where d denotes the particle size.

The *tortuosity* (as well as the *tortuosity factor*) generally describes how tortuous a pathway is for a species to transport between two locations in the microstructure. This pathway generally refers to the path between the starting location (typically a source/supply site) and the destination (typically a reaction site). While the tortuosity may be defined with only geometric considerations, the definition of the tortuosity factor is related to effective transport coefficients (diffusivity and conductivity) that pertain to physical transport in porous media [24]. A higher tortuosity suggests a longer pathway for a species to travel from the source site to the reaction site, leading to slow kinetics. As such, low tortuosity is favored for electrochemistry. There is little consensus in the literature on both the qualitative and the quantitative definitions of the tortuosity. For example, four different quantitative methods of measuring the tortuosities (or tortuosity factors) are described in [37, 51, 123].

[6]The intersection of pore, MIEC, and electrolyte may be considered as TPBs.

1.3 Modeling SOFC Electrochemistry

Simulating SOFC electrochemistry based on the 3D microstructures can help us understand the link between cell performance and microstructure. Much of the current foundation has been built using effective medium theory (EMT) approximations of the electrode microstructures for continuum modeling [1, 10, 12, 15, 21, 100, 113, 114], which appears to capture the average electrochemical property with reasonable accuracy. Using simulations of electrochemistry directly on the specific microstructure, we can avoid the potentially incorrect assumptions of electrode homogeneity built into EMT models. Such simulations, which are the focus of this work, not only can provide an improved understanding of the local mean properties (and the volumes required to achieve it), but also yield full distributions of relevant electrochemical parameters both within specific simulation volumes and across many different simulation volumes. To address degradation modes away from the mean performance, generating such distributions in performance metrics is essential.

1.3.1 Effective Medium Models

In effective medium models, the complex microstructure of an electrode is homogenized, i.e., the microstructure morphology is lost, and there is no distinct spatial phase separation. All quantitative formulations of electrochemical processes (e.g., transport and reaction mechanisms) are defined in this homogenized domain. Depending on the model assumptions and the geometry of the problem, an analytical solution may be obtained. The domain may also be subject to numerical discretization and approximation techniques such as finite element (FE) and finite volume (FV) methods. In such cases, a numerical solution is obtained to give relevant electrochemical parameters. Note that most of the inputs for effective medium modeling are effective/averaged properties (introduced earlier) quantified from a subvolume of a measured microstructure. The solutions from the effective medium models are also effective quantities. Here the word *effective* is synonymous with the word *averaged*. These average performance parameters, e.g., operation voltage and current density, of SOFCs have been related to the model

inputs, e.g., phase volume fractions, tortuosity, etc., determined over an appropriate microstructural domain.

1.3.2 Meshed Microstructure Models

Contrary to the effective medium models, the approach adopted by this work spatially preserves morphologies of volume, surface, and linear features in the SOFC microstructure. Several authors have carried out similar approaches, with voxel-based meshes used in finite volume methods [6, 7, 63, 65, 93, 104, 108, 134], voxel-based lattices used in Lattice-Boltzmann methods (LBMs) [38, 51, 55, 61, 89, 111], and smoothed unstructured meshes used in finite element methods [4, 8, 9, 42, 81, 105]. Quantitative formulations of electrochemical processes may be defined only in certain phase volumes and surfaces. Due to the complex geometry of the microstructural mesh, it is essentially impossible to obtain a closed-form solution. Therefore, a numerical solution has to be computed. The numerical solution consists of spatial distributions of electrochemical quantities in the computational domain. Since the microstructure is not homogenized, local electrochemistry, coupled with local morphological features, can be visualized and analyzed.

Note that the meshed microstructure models do not use the effective microstructure properties. Instead, the model directly operates on the meshed microstructure, which inherently contains information regarding volume fraction, surface area, tortuosity, etc., all of which are not explicitly computed.

1.4 Thesis Objective

1.4.1 Durability, Reliability, and Degradation

The advantages of SOFCs include high fuel flexibility, no moving parts, capability to recycle high temperature waste heat, and no use of precious metal catalyst [91, 99]. All these features indicate that SOFCs are suitable for long term, large scale stationary power plant applications. However, widespread commercialization of SOFCs is still limited by several challenges, of which the notable ones are low durability and poor reliability [116]. Durability refers to a cell's useful performance lifetime before eventual degradation and

failure, whereas reliability refers to cell-to-cell performance variation and any associated degradation rate. Both durability and reliability are tied to degradation in performance. It is suggested that well over 40,000 hours, or over four to five years, of operation is needed for SOFCs to be a viable, economical option to compete with the current conventional power generation industry [54, 132]. Yet this requirement is rarely met by cost-competitive commercial SOFCs due to unacceptable degradation over a much shorter time scale. This work aims to lay a foundation towards engineering SOFCs exhibiting decreased degradation. Since most degradation mechanisms in fuel cell electrodes have been found to be closely correlated to physiochemical reactions and transport phenomena in the microstructure (e.g., chromium poisoning in the cathode or nickel coarsening in the anode) [2, 66, 132], this work is concerned with how microstructural distributions influence local property distributions. As an initial step towards this end, we develop herein a high-throughput simulation approach to capture distributions of performance properties within fully resolved 3D electrode microstructures, and then use it to model/understand heterogeneous electrodes.

1.4.2 Microstructural Heterogeneity

Commercially fabricated cells suffer from unacceptably low durability and poor reproducibility, both of which can be related to the electrode microstructures and are likely due to their cost-constrained, large-scale manufacturing. Inconsistency is also seen in the electrode microstructures, where local variation of the physical features are expected over a wide range of length scales (from microns to hundreds of microns) [26, 83]. We define the extent of this local variation as microstructural heterogeneity.

There is no real consensus on a quantitative definition of microstructural heterogeneity. Heterogeneity refers to a state of being composed of dissimilar elements, which electrodes must be because they contain two or three phases. Thus, statistical metrics are obvious quantitative descriptors for heterogeneity, such as the distributions of specific microstructural features, including as particle size and volume fraction, in given local volumes. This work considers the distribution width (e.g., standard deviation) of relevant

microstructural properties and simulated performance metrics as the primary indicator of heterogeneity (from the mean value, or expected value of a homogeneous medium). In [48], the distribution standard deviations of local TPB densities and volume fractions across subvolumes were measured and used to adequately distinguish heterogeneous microstructures from uniform ones. However, there lacks a comprehensive (and quantitative) mapping of local phase distributions (and variations) to a detailed view of performance (or even degradation) in the literature.

Microstructural heterogeneity has not been extensively discussed in the literature. Currently, most fundamental research on SOFC microstructures is based on homogeneous research-grade cells that are fabricated in-house with highly optimized, small-scale methods. For homogeneous cells, the microstructure properties and electrochemical activity are fairly uniform and can be described with good statistical accuracy over a length scale of 5–15 µm, or about ten times the average particle size [16, 43, 44, 51, 57, 90, 125]. Such a scale is often referred to as the representative volume element (RVE), or the minimum volume scale that can statistically describe an effective (i.e., averaged) property (with user-defined tolerance). As mentioned earlier, effective medium modeling has been used to describe in-house cells' effective performance parameters with reasonable accuracy.

Commercial cells, however, have not been widely studied under effective medium modeling. Considering their heterogeneous microstructures, the electrochemistry may not be appropriately described by using effective properties. This statement is supported by the fact that degradation or failure events have been observed to occur locally and non-uniformly in the microstructure [80, 121]. More specifically, degradation sites tend to be highly localized at certain regions or morphological features (surfaces, TPBs), which the effective medium modeling approach does not capture due to domain homogenization. As such, we may expect substantial variation in local electrochemistry. Since effective medium modeling only outputs effective performance using effective microstructure properties, we place an emphasis on computing spatially-resolved electrochemistry from morphology-preserving meshes. Since the electrochemistry is resolved spatially, local variation of electrochemistry may be captured and analyzed.

1.4.3 Hypothesis

In summary, recent advances in 3D characterization techniques and effective medium modeling demonstrate that there is a reasonably accurate description of average performance using microstructure-based effective properties from relatively homogeneous cells. However, effective medium modeling has not adequately addressed microstructural degradation, which is one of the current challenges to widespread SOFC commercialization. First, commercial cells and their heterogeneities are not actively discussed. Second, microstructural degradation persists in commercial- and research-grade cells. Based on the observation that degradation is non-uniform and highly localized throughout microstructure, there is likely a substantial variation in local electrochemistry in commercial cells. To this end, we propose the following main hypothesis regarding local electrochemistry in SOFCs:

- Distributions of local electrochemical values can be quantified using simulations based on microstructural morphology-preserving meshes, which can be described by the average, standard deviation, and tails of such distributions.[7]

This hypothesis is further specified with respect to the computational method used in this work. Here the term electrochemistry is used interchangeably with performance. Thus, local electrochemistry means localized electrochemical activity, or simply localized performance metrics (often the electrical current density) in a certain region of interest. Thus, the hypothesis states that given a subvolume (region) of heterogeneous microstructure, meshed microstructure modeling is more likely to accurately compute local electrochemistry than continuum modeling can. And this statement is largely dependent on microstructural heterogeneity. Finally, part of the thesis objective is to quantify the extent of heterogeneity with which data analysis is consistent with the hypothesis.

[7] It is believed that degradation can be related to these distributions, but will not be tested herein.

1.4.4 Testing the Hypothesis

The necessary work to test the aforementioned hypothesis may be broken down into numerous separate studies, each of which may roughly correspond to an academic journal publication with a self-contained testable sub-hypothesis, an experiment (computational) design, and supporting results. Details regarding these studies are laid out at the end of the third chapter.

2

Methodology

2.1 Workflow Overview

A computational workflow is presented with an emphasis on the development of a microstructure-based electrochemical simulation framework suitable for high performance computing (HPC) resources. The key steps of the workflow are to acquire, process, mesh, and simulate solid oxide fuel cell (SOFC) cathode microstructures in a high-throughput fashion. The advantages of the workflow are:

- High-resolution, large-scale microstructure acquisition
- Straightforward image-based volumetric meshing that conforms to complex, multi-phased microstructures
- Computation of local electrochemical fields in morphology-resolved microstructures at considerable length scales
- Modular nature of user-defined physics; addition or modification of physics requires minimal programming effort

- Implementation on HPC platforms, leading to fast, high-throughput computations

The overall workflow—which is mostly computational, with only one experimental step: PFIB characterization—consists of the following general sequential steps:

- Segmented Microstructure Acquisition
- TPB Phase Labeling
- Pre-Mesh Processing
- Volumetric Meshing
- HPC Simulation

Fig. 2.1.1 presents a flowchart for the workflow. Each step may be broken down into multiple sub-steps, and their details will be described in later sections. The last step of the workflow, HPC Simulation, will be emphasized and separately detailed in a comprehensive manner. There may be additional details (e.g. toy mesh) in later sections that are not directly related to the steps in Fig. 2.1.1.

2.2 Microstructure Acquisition

2.2.1 Commercial SOFC Sample Overview

Part of this work focuses on commercial-grade SOFCs. Currently, the electrode microstructure studied here originated from 25 mm anode supported SOFC button cells supplied by a commercial manufacturer (Materials and Systems Research, Inc., Salt Lake City, UT), which will be referred to as MSRI. The MSRI cells consist of five component layers, which are described below from the cathode end to the anode end:

- Cathode current collector (CCC): Designed to be macro-porous for facile gas transport towards the cathode active layer. The CCC also contains LSM for fast electronic transport.

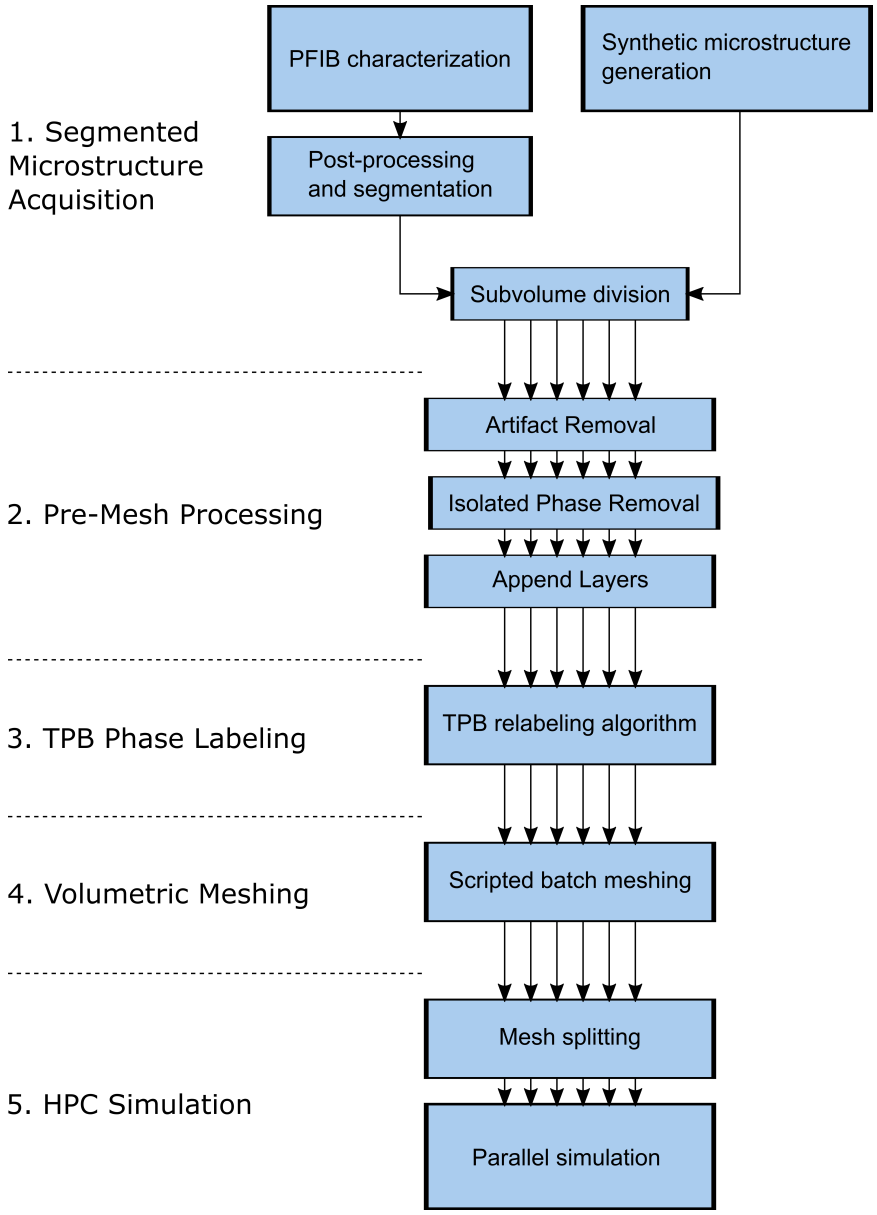

Figure 2.1.1: General flowchart of the computational workflow (except the PFIB characterization, which is an experimental method). Use of multiple arrows in parallel represent the flow of multiple subvolumes of microstructures data processed in parallel.

- Cathode active layer (CAL): Micro-porous, where most of the electrochemical activity (oxygen reduction) takes place.
- Electrolyte (EL): Non-porous layer through which the oxide ions transport to the anode side.
- Anode active layer (AAL): Micro-porous, where most of the electrochemical activity (fuel oxidation) takes place.
- Anode support layer (ASL): Designed to be macro-porous for facile gas and electronic transport and is the mechanical support of the entire cell – it is the thickest layer.

The compositions and layer thicknesses of the MSRI cells are summarized in Table 2.2.1. The scope of this work is restricted to studying the active layers (CAL and AAL). Our numerical model developed thus far only addresses the ORR at the cathode. Therefore, future sections only focus on CAL microstructure and electrochemistry.

	MSRI Cell Composition	Layer Thickness
CCC	LSM/pore	45 µm
CAL	LSM/YSZ/pore	10-15 µm
EL	YSZ	10 µm
AAL	Ni/YSZ/pore	10-15 µm
ASL	Ni/YSZ/pore	>700 µm

Table 2.2.1: MSRI cell composition by layers

2.2.2 FIB-SEM Characterization

The characterization workflow is implemented with the Helios PFIB DualBeam (plasma FIB, or PFIB) and the 3D acquisition package AutoSlice and View (FEI Company, Hillsboro, OR). Details of PFIB characterization are described elsewhere [83]. The typical scale for PFIB characterization is about 150–200 µm, which is roughly an order of magnitude larger than that of gallium FIB-SEM and X-ray nanotomography (10–30 µm).[1] Large-scale

[1] While X-ray nanotomography may be able to capture with about 60 µm of field of view, the light intensity generated from lab-based power source does not penetrate more than

tomography techniques (e.g., synchrotron computed tomography) developed thus far typically have limited resolution and therefore cannot capture the fine morphological features in electrode microstructures. Fig. 2.2.1 shows the MSRI microstructures characterized by the PFIB. The figure is part of our publication on meso-scale characterization of heterogeneous microstructures [48].

The scale of the microstructures from PFIB characterization is substantial, with small voxels on the order of 50 nm spanning across a (lateral) domain of 150–200 µm. Processing an entire volume from a PFIB scan at once can be time-consuming and intractable. Therefore, we typically divide an entire microstructure into multiple subvolumes for further work. The initial PFIB microstructural characterization methods were developed by me, with help from Noel Nuhfer, and were then passed to Rubayyat Mahbub. All of the data presented here were collected by me or myself in collaboration with Rubayyat Mahbub.

2.2.3 Synthetic Microstructure

In addition to physical microstrucures reconstructed using PFIB-SEM, synthetic microstructures are also used in this work. The construction of the synthetic microstructures are grain-based, and have been carried out. The 3D microstructrure software *Dream.3D* (BlueQuartz Software, Springboro, OH) constructs polycrystalline microstructures with user-defined grain size distributions and phase volume fractions (among other input conditions less relevant to this work). Details regarding the construction algorithm are described in [39]. In this work, microstructural heterogeneity based on different grain size distributions is considered. Depending on the standard deviation of the distribution, a series of microstructures with varying heterogeneity can be generated. To generate larger volumes, simulated annealing methods were used to stitch subvolumes together [48]. Two examples of the synthetic microstructures are shown in Fig. 2.2.2, which is also part of our publication [48]. Note that despite the microstructure generation is based on grains, the

about 45 µm of typical SOFC ceramic materials. Further post-scan processing reduces the size of the captured microstructure.

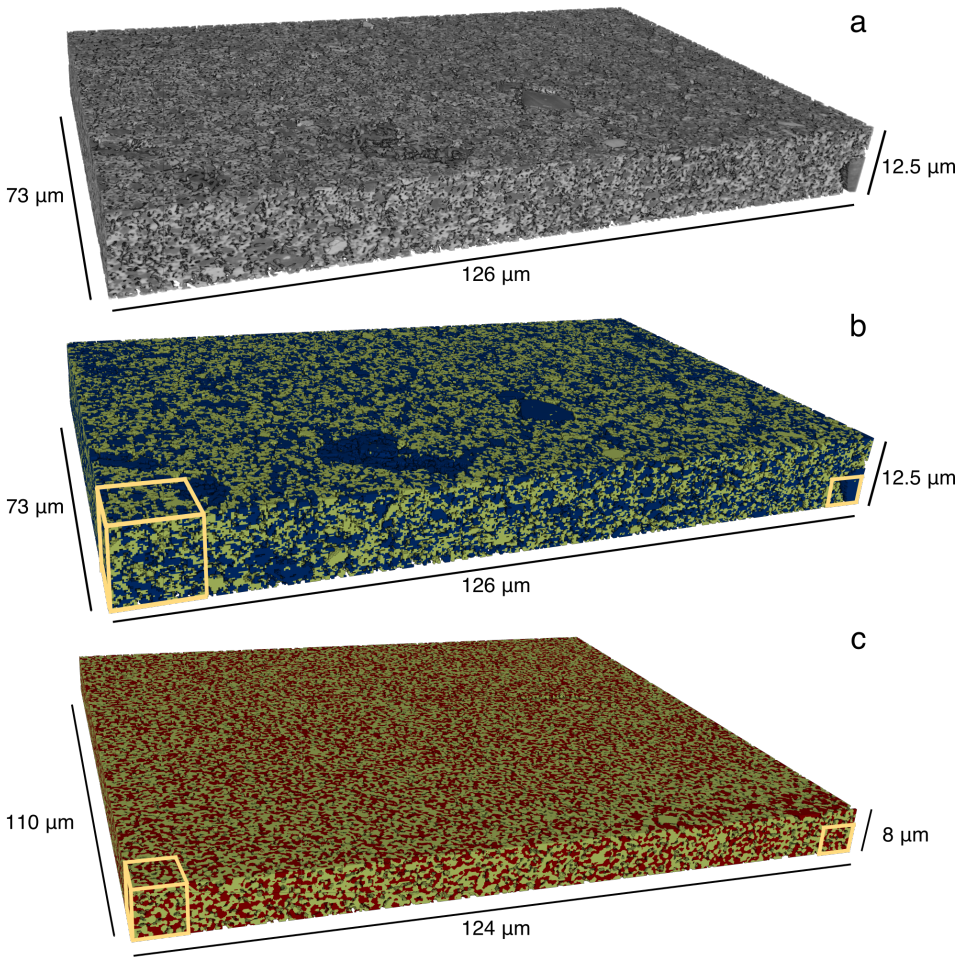

Figure 2.2.1: MSRI microstructures characterized by the PFIB. (a) Grayscale cathode. (b) Segmented cathode. (c) Segmented anode. The yellow boxes provide a measure of scale for a subvolume size of t^3 μm^3 (left) (t represents the thickness of an electrode) and of 5^3 μm^3 (right). Colors in segmented microstructures represent different phases. The pore phase is not shown here (transparent). The voxel dimension is 55 x 55 x 50 nm^3.

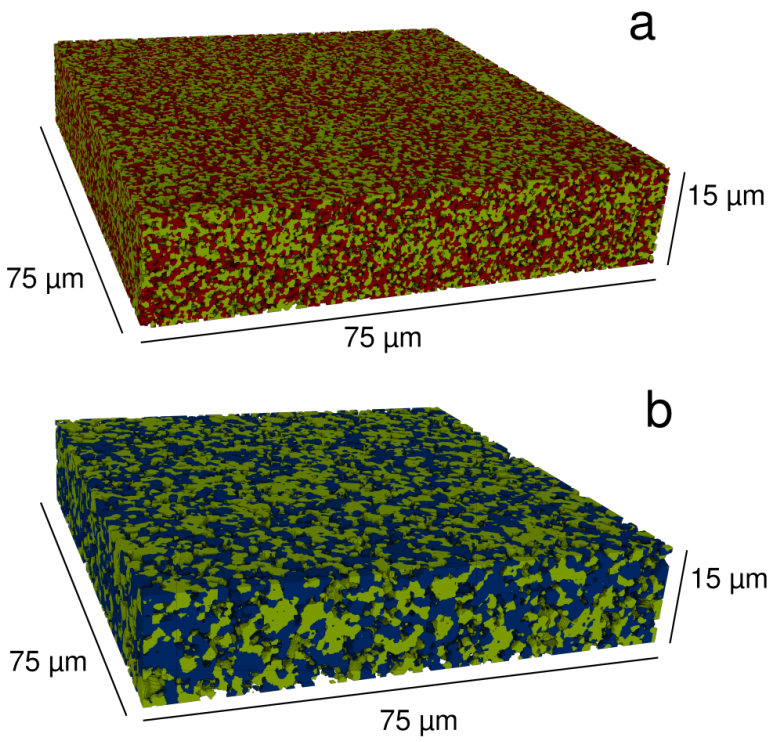

Figure 2.2.2: Synthetic three-phase microstructures generated by Dream.3D. The two microstructures shown here have different standard deviations as input for the grain size distribution. (a) corresponds to a standard deviation of 0.15 μm, whereas (b) corresponds to 0.6 μm. Colors represent different phases. The pore phase is not shown here (transparent). The voxel dimension is 125 x 125 x 125 nm^3.

colors in the figure indicate different phases. It can be seen that a higher standard deviation in grain size distribution results in higher heterogeneity.

The purpose of using synthetic microstructures is to test the effects of specific variations on local electrochemical performance quantities. In particular, we may establish when assumptions in effective medium theories for microstructural homogeneities diverge from actual microstructural features, and their effects on local properties. Comparison of the synthetic microstructures given in Fig. 2.2.2 with experimental PFIB microstructure given in Fig. 2.2.1 are discussed in [48]. It should be noted that the work on synthetic microstructure generation is done by a collaborator, William

K. Epting, who is affiliated with the National Energy Technology Laboratory (Pittsburgh, PA). He is currently developing more heterogeneous microstructures that capture mesoscale heterogeneity found in experimental microstructures and these may be included in future work as necessary.

2.3 Mesh Generation

Once an appropriate segmented 3D microstructure is available, the next step is to mesh the microstructure such that:

- it preserves the microstructural morphology,
- is appropriate for the physics to be simulated,
- can be used in our computational framework,
- and can be carried out in a high-throughput fashion (hundreds of meshed microstructures can be experimented upon).

To develop the discretized computational method, we used two types of meshes: (1) a basic mesh with simplified geometries that model specific features in a microstructure, and (2) a microstructural mesh based on physical and synthetic electrode microstructures. The basic mesh, which will be referred to as the *toy mesh*, is constructed from scratch by user design. The microstructural mesh is based on a pre-existing microstructural data. For both types, there are three material phases (since the MSRI active cathode is a three-phase electrode) and a quasi-material phase at the TPBs. The details of the quasi-material phase, or the TPB phase, will be discussed in a later section, but was generated to simplify the computation of TPB physics.

2.3.1 Toy Mesh

An open-source FE mesh generator, Gmsh [35], is used to create the toy meshes. Using either Gmsh's graphical user interface or its own scripting language, meshes with simple geometries may be created with basic shapes. The toy meshes serve testing and debugging purposes during the development of our numerical model. Due to the simplicity of their geometry, the

toy meshes help to visually validate the physical correctness of the model during development. Fig. 2.3.1 illustrates a simple cylindrical toy mesh that has been used frequently for model testing and benchmarking. The TPB phase is located along the center axis of the cylinder and is at the intersection of the outer three material phases (which hold equal volumes). Note that the TPB phase has been converted from an ideal lineal morphological feature to a volumetric feature with a small cross-sectional area and a very long axial dimension (an effective lineal feature). The justification for defining the TPBs as a volumetric morphological feature is explained in Sec. 2.4. Since the toy meshes can be customized, they may also be used to provide well-controlled parametric studies that model geometry-specific electrochemistries.

2.3.2 Microstructural Mesh

The microstructural mesh provides the computational domain for simulating SOFC operation coupled with the microstructural morphologies. Using this approach, we may quantify the effect of the microstructure on the local electrochemistry.

It is important to note that the microstructural meshes are based on pre-existing microstructural data. As discussed earlier, this work focuses on experimental and synthetic microstructures that have three-phase electrodes. Prior to meshing, the three-phase microstructures are converted to a four-phase microstructures, where the TPBs are converted from lineal features to a volumetric quasi-phase (the fourth phase). The TPB quasi-phase generation is carried out using an in-house relabeling algorithm that operates on segmented image data. Recall that segmented image data is represented as 3D image with each voxel labeled as one of the three material phases. The algorithm relabels the four voxels at the intersection of the three phases as a new TPB phase, the fourth phase. Fig. 2.3.2 illustrates how the algorithm relabels the microstructure data, where the four voxels adjacent to the intersection of the pore (blue phase), LSM (orange phase), and YSZ (green phase), are relabeled as the TPB (yellow) phase. A 2D slice image from the MSRI cathode microstructure is shown in Fig. 2.3.3, both with and

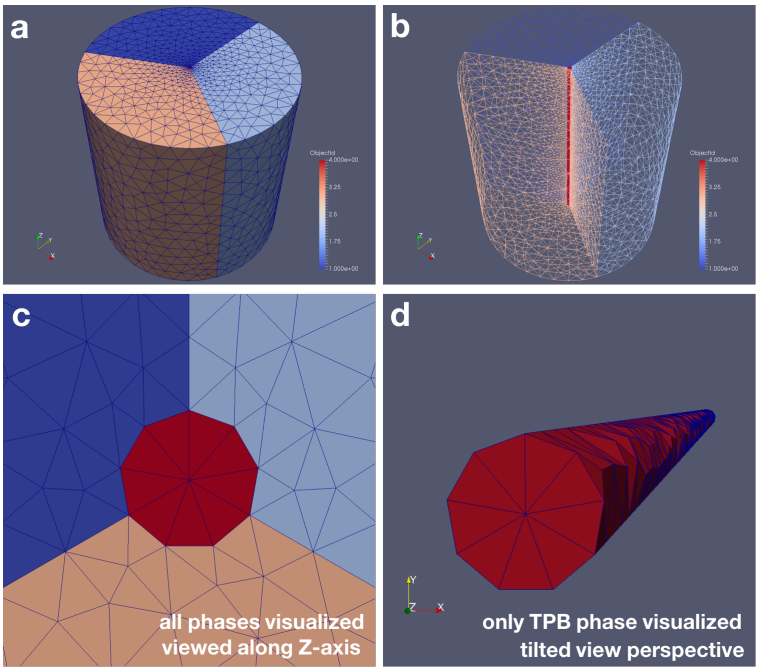

Figure 2.3.1: Visualization of the toy mesh used for testing purposes. This toy mesh has a cylindrical geometry. The entire mesh is visualized with (a) surface and edge rendering and (b) wireframe rendering. The tetrahedral elements can be seen in (a) and the thin TPB phase elements (in red color) can be seen in (b). The colorbar denotes phase ID numnber. Four colors (phases) are shown in the meshes. Additionally, (c) and (d) visualize the TPB elements in greater detail, with the same rendering mode as (a). The three material phases are transparent in (d).

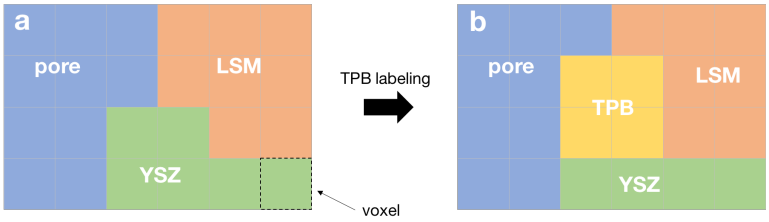

Figure 2.3.2: 2D Schematic for the TPB labeling algorithm. There are three phases in the original image (a). The voxels adjacent to the the three-phase intersection are relabeled as the TPB phase (b).

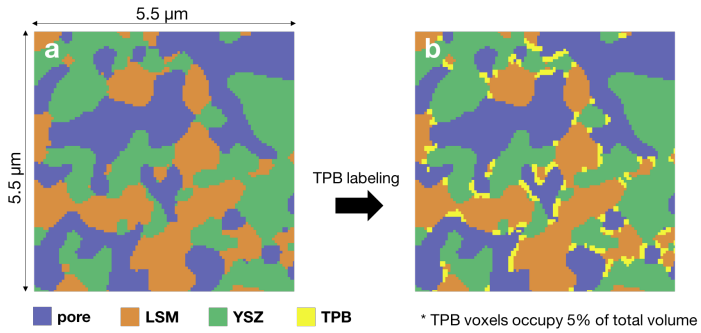

Figure 2.3.3: 2D image from the segmented MSRI cathode microstructure before (a) and after (b) TPB labeling.

without the TPB voxels. For most of the 3D datasets used in this work—whose voxel size is about 25–30 nm—the TPB voxels typically occupy about 0.5–4 % of the total volume. The voxel size can be changed by re-sampling the original microstructure data matrix. The simplest way of re-sampling without requiring any interpolation in order to reduce the voxel size (and therefore the TPB width) is to double (or triple) the resolution of the data matrix. For instance, an original voxel size of 50 nm becomes 25 nm after matrix doubling. All the 3D datasets used in this work have an original voxel size ranging from 50 to 65 nm (and 25–30 nm after matrix doubling or tripling). This size of the TPB volume is deemed acceptable to represent the 3D microstructure because the numerical result of our model is reasonably comparable to that of a well-established continuum model, as will be

discussed in the third chapter.

It should be noted that the TPB relabeling algorithm takes place at the end of a series of processes applied to the microstructure image data. These processes condition the microstructures for later numerical modelling. The processes are listed below:

- Artifact Removal: Sequential Dilation of Phases
- Isolated Phase Removal: Relabel Voxels
- Append Layers: Attach Electrolyte to Bottom[2]

Artifact Removal refers to the process of removing very small isolated features (phases) that are one-to-two voxels wide. These may be artifacts in the experimental data sets from imaging/processing, or outlier small grains in the synthetic data sets. These features should not impact performance but complicate the numerical stiffness. *Sequential dilation* refers to a series of morphological dilation operations that expand phases in a specific order using a structuring element. Similar to morphological opening and closing, it has the effect of removing very small isolated phases with sizes on the order of the structuring element. Details regarding the effect of sequential dilation was also described in [26]. The sequential dilation was typically carried out using a spherical structuring element with a two-voxel radius.

Isolated Phase Removal refers to the process of relabeling isolated phases, or those phases that are not connected (defined by nearest-neighbor connectivity) to the simulation boundaries. These isolated phases arise either by real isolation or by dividing the microstructure to a finite volume. In the current instantiation of ERMINE, these isolated phases cause non-physical solutions. Thus, a voxel labeled as GCP or ECP that has no connection to the top plane of the cathode is re-labeled as an inert phase that has no involvement in the SOFC electrochemistry. Similarly, an ICP voxel that has no connection to the bottom plane of the cathode is re-labeled as an inert phase. Relabeling the isolated phases also results in removal of isolated TPB lineal features (often called inactive TPBs).

[2]The *bottom* of the microstructure refers to the electrolyte side of the domain, whereas the *top* refers to the cathode side of the domain. Note that the entire domain is in a half-cell configuration (since we only model ORR).

Append Layers refers to the process of appending other cell components, such as an electrolyte, an anode, current collectors, etc. The current instantiation of ERMINE is coded for ORR electrochemistry in the cathode and the electrolyte; a cathode layer, an electrolyte layer, and an ideal counter electrode plane are considered for the entire computational domain. Thus, a thin electrolyte layer was appended to the bottom of the cathode by simply attaching artificial voxels all labeled as the ICP. The presence of the thin electrolyte layer also helps better satisfy the boundary condition at the counter electrode (bottom of electrolyte) by smoothing local gradients at the cathode/electrolyte interface. Finally, the appended electrolyte represents the physical SOFC better.

The aforementioned pre-meshing processes are relatively fast compared to the actual meshing procedure and therefore is not a limiting step for the overall high-throughput workflow. For example, 700 subvolumes, each of which is 5 x 5 x 5 μm^3 in size, can be processed within a day.

We use a commercial mesh generation software (Simpleware ScanIP+FE 7.0, license acquired in 08/2016, Synopsys, Inc., Mountain View, CA) and apply its proprietary meshing algorithms [133] to the four-phase microstructure. The outcome is an unstructured mesh consisting of tetrahedral elements representing the microstructure. Fig. 2.3.4 shows how the morphologies are well preserved after meshing the original microstructure. Some microstructural properties of the meshed microstructure in Fig. 2.3.4b, which can be directly measured by ScanIP, are similar to that of the original voxelized microstructure in Fig. 2.3.4a (measured by using in-house Matlab codes described elsewhere [26]). For example, the TPB line length can be measured by summing the lengths of the mesh element edges located at the triple junctions in a three-phase domain (TPB phase not yet labeled). It may not be possible to measure the TPB length of a meshed four-phase microstructure in ScanIP because the TPB is no longer a line entity.

Fig. 2.3.5 visualizes an example of an actual computational domain, which is a four-phase microstructural mesh of an individual subvolume. The cathode size is approximately 10 x 10 x 7 μm^3, to which a 10 x 10 x 3 μm^3 electrolyte was appended. Note that the mean particle size of the cathode

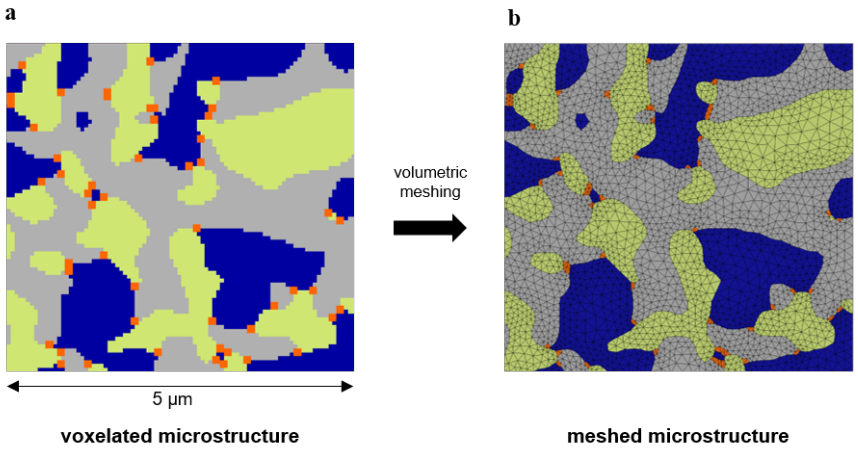

Figure 2.3.4: Visualization of Simpleware ScanIP Meshing. A cathode microstructure subvolume from the PFIB characterization is shown (a) before and (b) after the meshing algorithm. It can be seen that surfaces are well preserved after the meshing. The colors indicate phase contrast.

is 0.46 µm. The phases shown are pores (gray), LSM (blue), YSZ (green), and the TPBs (orange) (which are the GCP, ECP, ICP, and TPB, respectively). Isolated phases are transparent (readily observed as craters on the edges). (a) highlights the whole domain, without rendering of the mesh element edges: note that the meshed TPBs are difficult to discern owing to their size. (b) shows only the TPB phase, throughout the whole volume. (c) highlights the mesh elements near the top front corner of the cathode, where the TPBs are also more readily seen. (d) highlights how the TPBs are distributed on the ICP in 3D.

Since ScanIP allows Python scripting for interfacing with the software codes, an automatic batch meshing workflow has been implemented. In other words, a user may submit multiple subvolumes of microstructure data into a queue for meshing with customized parameters. Each meshing procedure is a parallel process using multiple CPU cores, and the queue may be processed serially or in parallel.[3] Currently, the software is installed on a workstation

[3]Processing the queue is not automatic, but manually by the user. For example, when meshing small subvolumes that do not require substantial CPU resources, a queue of 100 subvolumes may be broken down into two queues, each with 50 subvolumes, by utilizing

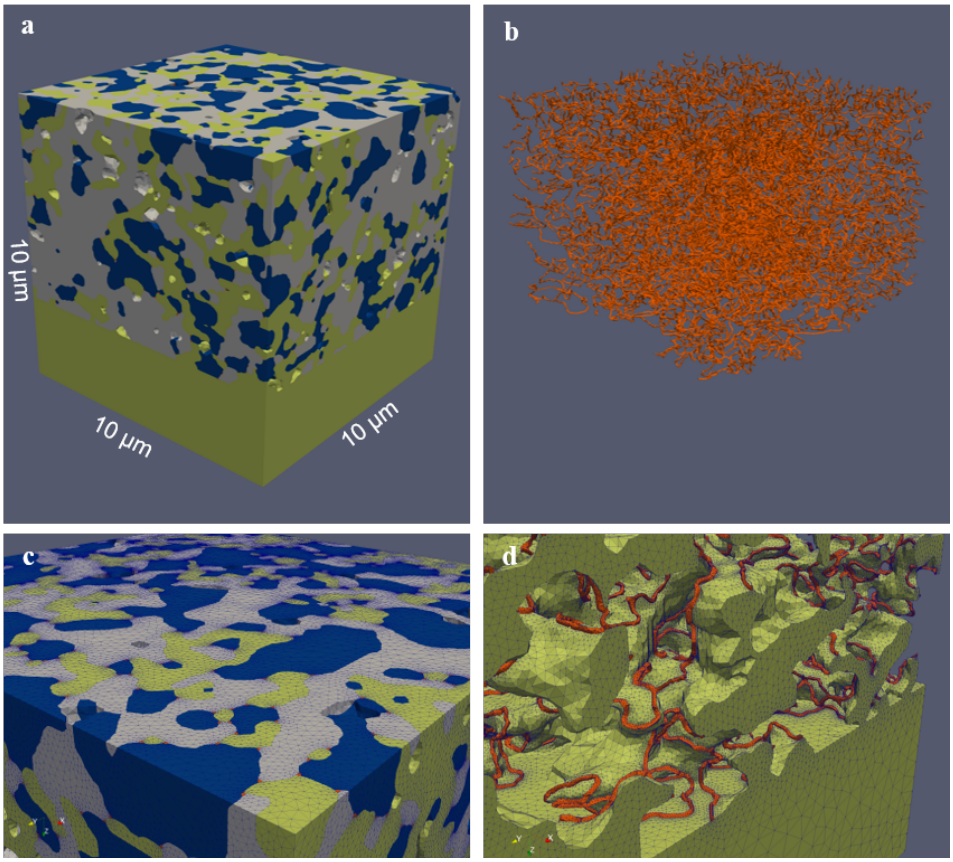

Figure 2.3.5: Rendered images of the unstructured tetrahedral mesh based microstructures derived from a subvolume of a commercial cell cathode from PFIB serial sectioning. (a) All four phases are visualized in this edge rendered image, without mesh elements. The phases shown are pores (gray), LSM (blue), YSZ (green), and the TPBs (orange). Isolated phases are transparent (readily observed as craters on the edges). (b) TPB phase visualized as a surface rendered image. A magnified region of (a) is shown in (c), with the mesh elements rendered. (d) A magnified surface and edge rendered image highlighting the TPB mesh on the YSZ mesh. In this particular subvolume, the numbers of tetrahedral elements for the pore, LSM, YSZ, and TPB phases are respectively 10.8, 8.9, 6.4, and 3.3 million, which are typical numbers for the subvolume scale in the figure.

with 32 cores, which can accommodate up to two or three meshing procedures simultaneously. Typically, the meshing runtimes are about 10 minutes, 20 minutes, 40 minutes, and 1-2 hours for cubic microstructure volumes with edge lengths of 5, 7.5, 10, and 12.5 µm, respectively. However, the runtime may vary significantly depending on the microstructure morphology. The scripts (written in Python) for batch meshing, along with the meshing parameters, are available at https://github.com/tim-hsu/scanip-scripts.

2.4 Numerical Model

2.4.1 Model Overview

Very broadly, our numerical model is a reaction-and-transport model that simulates electrochemistry in SOFC electrode microstructures at operating conditions. The operating conditions are states that deviate from the thermodynamic equilibrium state, or the reversible state. We define both global and local deviations from the reversible state. These deviations exist over different length scales. We are particularly interested in understanding how local deviations (at the microscopic scale) are manifest across a microstructure given a specific global deviation (at the macroscopic scale).

Deviations from global equilibrium are associated with effective, experimentally measured parameters that relate to an electrode's (or a cell's) overall performance (e.g., a cell's voltage and current). Specifically, we define the global reversible equilibrium point to be the open circuit (OC) state: a state in which no global net current is measurable. The reversible cell voltage (E_{model}) is defined as the open circuit voltage (OCV), which is fixed by the oxygen partial pressures at OC on either side of the cathode-electrolyte domain. The oxygen partial pressures at OCV are model parameters that govern boundary conditions. The global deviation from OCV during cell operation is defined to be the cell overpotential (η_{model}). In potentiostatic operation of an SOFC, the global driving force is the cell overpotential, which is also a model parameter that affects boundary conditions. The mathematical description of the boundary conditions will be discussed later.

two ScanIP sessions on the workstation.

The deviations from local equilibrium, on the other hand, are related to the driving forces that dictate local reaction/transport rates at the microscopic scale. The local driving forces are formulated mathematically over the entire mesh, and are related to the global driving forces, the microstructural network, materials parameters, and transport/reaction models implemented. They obviously vary locally within the microstructure. We impose formulations regarding local driving forces that, in turn, dictate how the model computes the electrochemical steady state. The resultant electrochemical steady state is represented by numerical values (or other mathematical expressions based on the numerical values) of relevant field variables computed throughout the microstructural mesh.

In summary, we introduce a global driving force to the model as boundary conditions and, based on specific rules formulated with respect to the local driving forces (reaction and transport), the model outputs an electrochemical steady state represented by local numerical field variables.

This work focuses on the cathode side of the fuel cell for several reasons: (1) In general, the cathode ORR is more sluggish than the anode HOR (assuming hydrogen gas as fuel for the anode side). (2) For the commercial cell microstructures observed, the cathode appears a lot more heterogeneous than the anode. (3) The development time for the work only allows detailed implementation on one side of the fuel cell.

The model assumes a mesh domain consisted of three volumetric material phases and one volumetric quasi-material phase. The three material phase are the GCP, the ECP, and the ICP. The quasi-material phase is the TPB phase. For the MSRI cathode, the ECP is lanthanum strontium manganite (LSM), or $(La_{1-x}Sr_x)_{1-\epsilon}Mn_{1-\epsilon}O_{3-\delta}$, where x, ϵ, and δ denote the strontium substitution level, the cation vacancy level (assuming equivalent Sr and Mn vacancy populations), and the oxygen vacancy level, respectively. We assume the cation vacancy levels to be close to zero, i.e, $\epsilon = 0$. We use the following reference state for LSM (which establishes a reference for individual species thermodynamic activity): the reference forumla unit is $La_{La}^{3+}Mn_{Mn}^{3+}(O_O^{2-})_3(e_{vb}^{-1})_1(h_{cb}^{0})_1$, where the subscripts vb and cb denote valence band and conduction band. The oxygen ion conducting phase is yttria-stabilized zirconia (YSZ), or $Zr_{1-y}Y_yO_{2-y/2}$, where y denotes the yt-

trium substitution level. The reference formula unit for YSZ is $Zr_{Zr}^{4+}(O_O^{2-})_2$. The TPB quasi-material phase, located at the intersection of pores, LSM, and YSZ, is rendered as a network of thin strings. The TPB volume contains all field variables defined for each of the three material phases.

Since we aim to model reaction and transport as driven by local driving forces at the micro-scale (from submicrons to tens of microns), only microscopic driving forces are considered in the domain. Both atomistic and large scale driving forces are disregarded. With proper consideration of the relative magnitudes of the possible driving forces, we make the following simplifying assumptions:

- The solids phases (LSM and YSZ) are considered as rigid bodies (non-deforming), thus containing no pressure/stress gradients.

- Inside pores, diatomic oxygen gas transport is governed by Fickian diffusion (driven by concentration gradients). Pressure gradients are disregarded due to the small length scale over which oxygen gas travels in the domain.

- Inside LSM, oxide ion transport is governed by Fickian diffusion. Potential gradients are disregarded due to the relatively high electronic conductivity of LSM. In other words, a constant potential is assumed in LSM. (Future instantiations may lift this assumption, but requires a further inclusion of the Poisson equation and other materials parameters in LSM).

- Inside YSZ, oxide ion transport is governed by drift, or driven by electrical potential gradients. Concentration gradients are disregarded due to the relatively high concentration of oxide vacancies and high mobility of the oxide ions in YSZ. In other words, a constant oxide ion/vacancy concentration is assumed in YSZ.

2.4.2 Global Equilibrium and Deviation

The global parameters with respect to the global equilibrium and deviation are explained in further details here. Using the mesh from Fig. 2.3.5, we

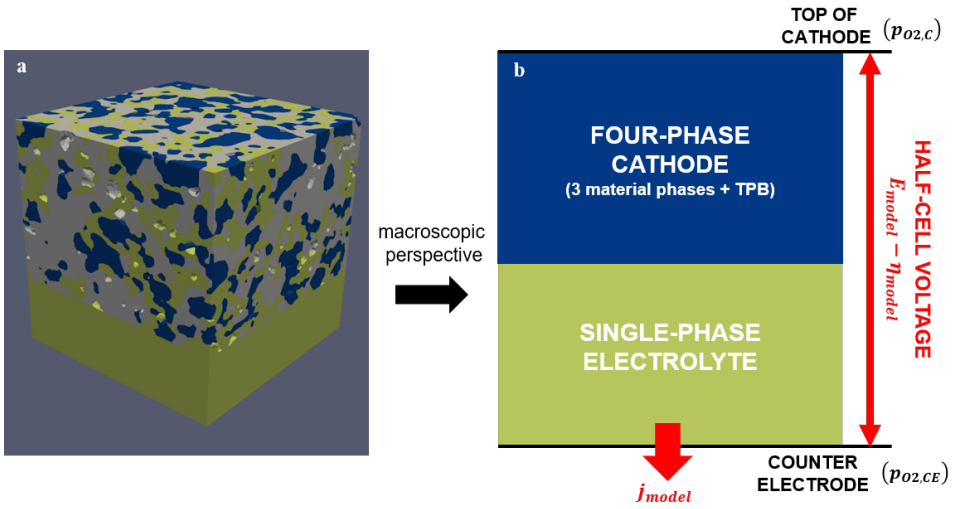

Figure 2.4.1: Schematic of the global parameters of the numerical model with respect to the computational domain geometry. (a) represents the actual mesh domain with microscopic details. (b) shows the global parameters in the macroscopic perspective.

may view the mesh domain in macroscopic perspective and introduce the global parameters, as shown in Fig. 2.4.1.

At OCV (i.e., no global net current), there exists a reversible potential drop, E_{model}, from the top of the domain to the bottom of the domain. This is determined from the oxygen partial pressures at either side of the cathode-electrolyte domain, according to

$$E_{model} = -\frac{RT}{4F} \ln \frac{p_{O_2,CE}}{p_{O_2,C}}, \tag{2.1}$$

where $p_{O_2,CE}$ is the oxygen partial pressure at the counter electrode and $p_{O_2,C}$ the oxygen partial pressure at the top of the cathode. The present model is potentiostatic: we provide a global overpotential, η_{model}, as the global driving force enabling current flow, and the global current density, j_{model}, at the bottom of the domain is determined as an output. Specifically, j_{model} is an averaged quantity from the distribution of the local current density measured at the counter electrode (bottom plane of the domain). The cell voltage, written as $\phi_{LSM} - \phi_{CE}$, is the voltage difference between

the LSM potential and the counter electrode potential.[4]

When the cell is at global equilibrium, there is no net driving force, making $\eta_{model} = 0$ and $j_{model} = 0$, and the cell voltage is simply

$$\phi_{LSM} - \phi_{CE} = E_{model}. \tag{2.2}$$

When the cell is at a state where $\eta_{model} \neq 0$, the cell voltage then becomes

$$\phi_{LSM} - \phi_{CE} = E_{model} - \eta_{model}. \tag{2.3}$$

For simplicity, ϕ_{CE} is defined to be zero, thus the LSM potential is determined by

$$\phi_{LSM} = E_{model} - \eta_{model}. \tag{2.4}$$

2.4.3 ORR Pathways

The present model simulates ORR in a cathode microstructure occurring via two parallel pathways – the TPB pathway and the MIEC (or 2PB) pathway. We consider the reactions involved in both pathways to be local in the microstructure. It is important to reinforce that η_{model} (together with E_{model}) dictates the overall driving force to the global domain, but local equilibrium dictates local reaction rate throughout the domain.

In the MIEC pathway, the ORR occurs via two interfacial reactions sequentially. Oxygen gas is first reduced and incorporated into LSM as oxide ions via the surface exchange (se) reaction at the pore/LSM interface, written as

$$\mathrm{O_{2(g),p}} + 2\,\mathrm{V_{O,L}^{\bullet\bullet}} + 4\,\mathrm{e_{vb,L}^{x}} \longleftrightarrow 2\,\mathrm{O_{O,L}^{x}} + 4\,\mathrm{h_{vb,L}^{\bullet}} \tag{2.5}$$

in (a modified) Kröger–Vink notation. The subscripts p and L (pore and LSM, respectively) denote the phase at which the species is defined. The MIEC pathway is completed when oxide ions in LSM are then transferred into YSZ via the charge transfer (ct) reaction occurring at the LSM/YSZ

[4]Since the potential drop in LSM is assumed to be neglibible, the LSM potential is equivalent to the cathode potential (specifically at the top of the cathode).

interface:

$$\mathrm{V}_{\mathrm{O,Y}}^{\bullet\bullet} + \mathrm{O}_{\mathrm{O,L}}^{\mathrm{x}} \longleftrightarrow \mathrm{V}_{\mathrm{O,L}}^{\bullet\bullet} + \mathrm{O}_{\mathrm{O,Y}}^{\mathrm{x}}, \tag{2.6}$$

where the phase subscript Y denotes YSZ. Both of these interfacial reactions are modeled as reaction fluxes across the aforementioned interfaces, coupling the separate phases.

In the TPB pathway, the ORR occurs in a single step in the TPB quasi-material volume. The TPB reaction is

$$\mathrm{O}_{2(\mathrm{g}),\mathrm{p}} + 2\,\mathrm{V}_{\mathrm{O,Y}}^{\bullet\bullet} + 4\,\mathrm{e}_{\mathrm{vb,L}}^{\mathrm{x}} \longleftrightarrow 2\,\mathrm{O}_{\mathrm{O,Y}}^{\mathrm{x}} + 4\,\mathrm{h}_{\mathrm{vb,L}}^{\bullet}, \tag{2.7}$$

where oxygen transfers from pores to YSZ, and electrons transfer from LSM to YSZ (on oxide ions). It is important to mention that the TPB ORR, or simply the TPB reaction, is modelled as a volumetric reaction rate. Numerically, this volumetric rate acts as a source/sink term defined over the TPB mesh elements. Geometrically, the TPBs in electrode microstructures may be viewed as lineal morphological features. However, it is not straightforward to define a reaction over one-dimensional lines that do not occupy any physical volume. Therefore, we define the TPB reaction to occur in small finite volumes along the TPBs. This definition necessitates labeling the TPB voxels and generating the TPB mesh elements, as described in Sec. 2.3.

Fig. 2.4.2 is a visual representation of the ORR pathways in the MSRI three-phase cathode composition. Note that only the oxygen species is shown, along with the involvement of electrons. As mentioned before, oxide ion transport is equivalent to oxide vacancy transport.

2.4.4 Local Equilibrium and Deviation – Bulk Transport

For all the aforementioned reactions (Eq. 2.5, 2.6, and 2.7) involved in the ORR pathways, the reaction kinetics depend on bulk transport of reactants to the reaction sites. Here we address the formalism for the bulk transport in each phase.

We begin with the perspective of irreversible thermodynamics. Given

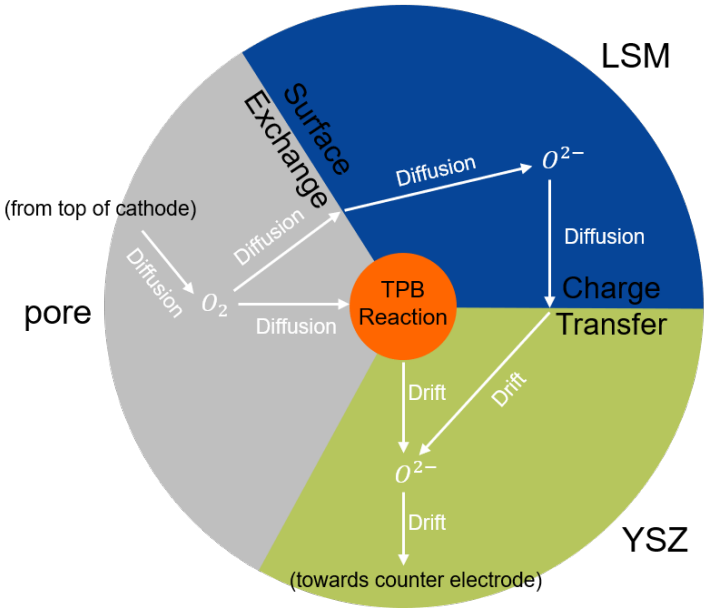

Figure 2.4.2: Schematic of the ORR pathways in MSRI three-phase composition. Arrows indicate general directions of oxygen fluxes via the pathways.

a species transport (or a reaction), when near equilibrium conditions are assumed, the net driving force is close to zero, and a linear relationship between the rate/flux and its driving force may be considered [84]:

$$J = \beta X, \tag{2.8}$$

where J is the transport/reaction rate, β is the linear coefficient, and X is the general net driving force. In the case of chemical reaction, the reaction rate is linearly proportional to the chemical affinity,

$$J_r = \beta_r A \propto -\Delta_r G = -\Delta_r G^0 - RT \ln(Q_r). \tag{2.9}$$

In the case of transport, $\Delta_r G^0 = 0$, and the transport rate may be expressed as

$$J_t = \beta_t(-\nabla \tilde{\mu}) = -\beta_t \nabla \mu - \beta_t z F \nabla \phi, \tag{2.10}$$

which, depending on the condition, can be further reduced to diffusion or drift. For example, in the absence of electrical potential gradient, the ex-

pression for the transport rate is simplified to Fick's law,

$$J_t = -\beta_t \nabla \mu = -\beta_t \nabla(\mu^0 + RT \ln \frac{c}{c^0}) = -\frac{\beta_t RT}{c} \nabla c = -D \nabla c. \tag{2.11}$$

Note that a dilute or ideal solution is assumed for the expression above. Since $D = \beta_t RT/c$, one can easily convert between concentration gradient and chemical potential gradient, as shown in

$$J_t = -D \nabla c = -\frac{Dc}{RT} \nabla u. \tag{2.12}$$

On the other hand, in the absence of chemical potential gradient, the expression for the transport rate is simplified to Ohm's law,

$$J_t = -\beta_t z F \nabla \phi = -\frac{\sigma}{zF} \nabla \phi. \tag{2.13}$$

We can see that β_t is in both Fick's law and Ohm's law described above, and the diffusivity can be related to the conductivity by

$$\sigma = \frac{c(zF)^2 D}{RT}. \tag{2.14}$$

In this document, the capital letter J stands for molecular flux/reaction rate ($\mathrm{mol/s\,cm^2}$), and the small letter j stands for electric flux/reaction rate ($\mathrm{A/cm^2}$). For electrochemical reactions involving charge transfer, molecular flux can be converted to electric flux by

$$j = zFJ. \tag{2.15}$$

For bulk transport phenomena such as oxygen diffusion and ionic drift, we consider empirical linear flux-force relationships, which are commonly accepted and extensively used. Specifically, the oxygen gas diffusion flux in pores is described by

$$J_{O_2} = -D_{O_2} \nabla c_{O_2}, \tag{2.16}$$

where the oxygen gas diffusivity, D_{O_2}, is a calculated model parameter, and c_{O_2} is oxygen concentration in pores. The equation above is further converted

into

$$J_{O_2} = -\frac{D_{O_2}}{RT}\nabla p_{O_2} \tag{2.17}$$

by the ideal gas law. p_{O_2}, or the oxygen partial pressure in pores, is a field variable in pores and the TPB phase to be solved numerically.

We calculate D_{O_2} as a combined diffusivity from the molecular binary diffusivity, D_{ij}, and Knudsen diffusivity, D_{iK}

$$\frac{1}{D_{O_2}} = \frac{1}{D_{ij}} + \frac{1}{D_{iK}}. \tag{2.18}$$

From the Chapman-Enskog theory, the binary diffusivity of oxygen in nitrogen is estimated as [45]

$$D_{ij} = \frac{0.0018583T^{\frac{3}{2}}}{P_{total}\sigma_{ij}^2\Omega}\left(\frac{1}{M_i} + \frac{1}{M_j}\right)^{\frac{1}{2}}, \tag{2.19}$$

where D_{ij} is the binary diffusivity (cm^2/s), T is the temperature (K), P_{total} is the total pressure (atm), σ_{ij} is the collision diameter of the two species (Å), Ω is the dimensionless collision integral based on the interaction of the two species, and M is the molecular weight (g/mol). Details regarding σ_{ij} and Ω can be found in [5, 20]. The Knudsen diffusivity is estimated as [19]

$$D_{iK} = \frac{d_P}{3}\sqrt{\frac{8RT}{\pi M_i}} = 4580 d_p\sqrt{\frac{T}{M_i}}, \tag{2.20}$$

where d_p is the mean pore diameter (cm), T is the temperature (K), and M is the molecular weight (g/mol).

In LSM, the oxide ion transport flux is also described by Fickian diffusion,

$$J_O = -D_O\nabla c_O, \tag{2.21}$$

where the oxide ion diffusivity, D_O, is a referenced parameter, and c_O is the concentration of the oxide ions in LSM. We may express c_O in terms of vacancy site fraction, as shown in

$$c_O = \frac{3 - [\mathrm{V}_\mathrm{O}^{\bullet\bullet}]}{a^3 N_A}. \tag{2.22}$$

Here we assume the LSM crystal structure is cubic with a lattice constant of a, and there is one formula unit per unit cell. N_A is the Avogadro's number. The oxide ion diffusion flux can then be rewritten as

$$J_O = \frac{D_O}{a^3 N_A} \nabla [\mathrm{V_O^{\bullet\bullet}}]. \tag{2.23}$$

Here $[\mathrm{V_O^{\bullet\bullet}}]$, or the oxide vacancy site fraction, is a field variable in LSM and the TPB phase to be solved numerically.

In YSZ, the oxide ionic current flux is described as

$$j_i = -\sigma_i \nabla \phi_{YSZ}, \tag{2.24}$$

where the oxide ionic conductivity, σ_i, is a referenced parameter, and ϕ_{YSZ}, or the YSZ potential, is a field variable in YSZ and the TPB phase to be solved numerically.

2.4.5 Local Equilibrium and Deviation – Reaction Rates

For local reaction rates occurring at certain morphological features, we consider the possibility that the local driving forces are farther from equilibrium, where the reaction rate may no longer be linearly proportional to the driving force. Given a general reaction expressed by

$$\sum_{r=1}^{R} \mathrm{v_r S_r} \rightleftharpoons \sum_{p=1}^{P} \mathrm{v_p S_p}, \tag{2.25}$$

where r, p represent reactants and products, respectively, and $v_{r,p}$ represent molar coefficients of chemical (or quasi-chemical) species $S_{r,p}$. The reaction rate is assumed to follow the laws of chemical kinetics and consists of forward (f) and backward (b) reaction rates

$$J = k_f \prod_{r=1}^{R} [S_r]^{v_r} - k_b \prod_{p=1}^{P} [S_p]^{v_p}, \tag{2.26}$$

where k_f and k_b are forward and backward reaction rate coefficients, respectively, and $[S_i]$ is the concentration of the ith species. These rate coefficients

are, according to the transition state theory, exponentially proportional to an activation energy:

$$k_f = k'_f \exp\left(-\frac{\Delta G_f^\dagger}{RT}\right), \tag{2.27}$$

$$k_b = k'_b \exp\left(-\frac{\Delta G_b^\dagger}{RT}\right), \tag{2.28}$$

where k'_f and k'_b are constants and $\Delta G_{f,b}^\dagger$ are the (positive definite) free energy barriers under the given thermodynamic state. The dagger symbol (†) denotes involvement of the transition states. For heterogeneous electrochemical reactions that involve local potential differences, we consider the activation energy as influenced by the local electrical potential difference (denoted by the *tilde* overhead), as well as the symmetry factor, α, of the activation energy profile, as shown in

$$\widetilde{\Delta G_f^\dagger} = \Delta G_f^\dagger - \alpha z F \Delta\phi, \tag{2.29}$$

$$\widetilde{\Delta G_b^\dagger} = \Delta G_b^\dagger + (1-\alpha) z F \Delta\phi, \tag{2.30}$$

where $\Delta\phi$ is the local potential difference. The rate coefficients can then be rewritten as

$$k_f = k'_f \exp\left(-\frac{\Delta G_f^\dagger}{RT}\right) \exp\left(\frac{\alpha z F \Delta\phi}{RT}\right), \tag{2.31}$$

$$k_b = k'_b \exp\left(-\frac{\Delta G_b^\dagger}{RT}\right) \exp\left(\frac{-(1-\alpha) z F \Delta\phi}{RT}\right). \tag{2.32}$$

The expression above may be further reduced to

$$k_f = k''_f \exp\left(\frac{\alpha z F \Delta\phi}{RT}\right), \tag{2.33}$$

$$k_b = k''_b \exp\left(\frac{-(1-\alpha) z F \Delta\phi}{RT}\right). \tag{2.34}$$

At equilibrium, $\Delta\phi$ becomes the reversible potential, $\Delta\phi_{rev}$, and the forward reaction rate is equal to the backward reaction rate

$$k_f'' \exp\left(\frac{\alpha z F \Delta\phi_{rev}}{RT}\right) \prod_{r=1}^{R} [S_r]_0^{v_r} = k_b'' \exp\left(\frac{-(1-\alpha) z F \Delta\phi_{rev}}{RT}\right) \prod_{p=1}^{P} [S_p]_0^{v_p}, \tag{2.35}$$

where the subscript 0 denotes a reference equilibrium state. Rearranging the expression above leads to

$$\Delta\phi_{rev} = \frac{RT}{zF} \ln\left(\frac{k_b'' \prod_{p=1}^{P} [S_p]_0^{v_p}}{k_f'' \prod_{r=1}^{R} [S_r]_0^{v_r}}\right). \tag{2.36}$$

At non-equilibirum, we define the overpotential, η, to be the difference between the actual potential and the reversible potential, as shown in

$$\eta = \Delta\phi - \Delta\phi_{rev}. \tag{2.37}$$

Thus, the reaction rate may now be expressed as

$$J = k_f'' \prod_{r=1}^{R} [S_r]^{v_r} \exp\left(\frac{\alpha z F(\eta + \Delta\phi_{rev})}{RT}\right) - k_b'' \prod_{p=1}^{P} [S_p]^{v_p} \exp\left(\frac{-(1-\alpha) z F(\eta + \Delta\phi_{rev})}{RT}\right). \tag{2.38}$$

After factoring out $\Delta\phi_{rev}$ and some algebraic manipulation, we may rewrite the reaction rate in the form of the Butler-Volmer equation

$$j = j_0 \left\{ \frac{\prod_{r=1}^{P} [S_r]^{v_r}}{\prod_{r=1}^{R} [S_r]_0^{v_r}} \exp\left(\frac{\alpha z F \eta}{RT}\right) - \frac{\prod_{p=1}^{P} [S_p]^{v_p}}{\prod_{p=1}^{R} [S_p]_0^{v_p}} \exp\left(\frac{-(1-\alpha) z F \eta}{RT}\right) \right\}, \tag{2.39}$$

where j_0 is the exchange current density.

For the surface exchange reaction, since the interaction between the oxygen gas and the LSM surface does not involve charge transfer across the pore/LSM interface, there is no associated potential difference. Thus, the reaction rate may be expressed as

$$J = r_0 \left\{ \frac{\prod_{r=1}^{P} [S_r]^{v_r}}{\prod_{r=1}^{R} [S_r]_0^{v_r}} - \frac{\prod_{p=1}^{P} [S_p]^{v_p}}{\prod_{p=1}^{R} [S_p]_0^{v_p}} \right\}, \tag{2.40}$$

where r_0 is the exchange rate. We can treat the reaction rate as linearly dependent on the oxygen concentration deviation from an effective, equilibrium concentration at the LSM surface.

$$J \approx r_0 \left(\frac{c_{O,eq} - c_O}{c_{O,eq}} \right). \tag{2.41}$$

Alternatively, one can derive the expression above using linear irreversible thermodynamics. We first go back to

$$J = k_f \prod_{r=1}^{R} [S_r]^{v_r} - k_b \prod_{p=1}^{P} [S_p]^{v_p}. \tag{2.42}$$

At equilibrium, $J = 0$, and the forward reaction rate is equal to the backward reaction rate:

$$k_f \prod_{r=1}^{R} [S_r]^{v_r} = k_b \prod_{p=1}^{P} [S_p]^{v_p}, \tag{2.43}$$

and the equilibrium constant is simply

$$K = \frac{k_f}{k_b} = \frac{\prod_{p=1}^{P} [S_p]^{v_p}}{\prod_{r=1}^{R} [S_r]^{v_r}}. \tag{2.44}$$

Under non-equilibrium conditions, the reaction rate can be expressed as

$$J = k_f \prod_{r=1}^{R} [S_r]^{v_r} \left\{ 1 - \frac{k_b}{k_f} \frac{\prod_{p=1}^{P} [S_p]^{v_p}}{\prod_{r=1}^{R} [S_r]^{v_r}} \right\} = k_f \prod_{r=1}^{R} [S_r]^{v_r} \left\{ 1 - \frac{Q}{K} \right\}, \tag{2.45}$$

where Q is the reaction quotient. Since the overall Gibbs free energy change of the reaction is

$$\Delta_r G = RT \ln \frac{Q}{K}, \tag{2.46}$$

the reaction rate then becomes

$$J = k_f \prod_{r=1}^{R} [S_r]^{v_r} \left\{ 1 - \exp \frac{\Delta_r G}{RT} \right\}. \tag{2.47}$$

If the reaction is near equilibrium or $|\Delta_r G| \ll RT$, linearization $\exp(x) \approx$

$1 + x$ applies, and the reaction rate is linearly proportional to the chemical affinity:

$$J = -k_f \prod_{r=1}^{R} [S_r]^{v_r} \frac{\Delta_r G}{RT} = -k_b \prod_{p=1}^{P} [S_p]^{v_p} \frac{\Delta_r G}{RT} = \frac{r_0}{RT} A = -\frac{r_0}{RT} \Delta_r G, \quad (2.48)$$

where r_0 is the exchange rate and A is the chemical affinity. We consider such condition for the surface exchange reaction, whose rate is linearly driven by the difference in the free energy. Recall that the surface exchange reaction is

$$\frac{1}{2}\,\mathrm{O}_{2(\mathrm{g}),\mathrm{p}} + \mathrm{V}_{\mathrm{O,L}}^{\cdot\cdot} + 2\,\mathrm{e}_{\mathrm{vb,L}}^{\mathrm{x}} \longleftrightarrow \mathrm{O}_{\mathrm{O,L}}^{\mathrm{x}} + 2\,\mathrm{h}_{\mathrm{vb,L}}^{\cdot} \quad (2.49)$$

We describe the change in Gibbs free energy with simplified notation that only addresses the material phase for each electrochemical potential:

$$\Delta_r G = \tilde{\mu}_O^L + 2\tilde{\mu}_h^L - 1/2\tilde{\mu}_{O_2}^p - \tilde{\mu}_{V_O}^L - 2\tilde{\mu}_e^L. \quad (2.50)$$

Since the overall reaction is not dependent on the potential, only the chemical potential terms remain:

$$\Delta_r G = \mu_O^L + 2\mu_h^L - 1/2\mu_{O_2}^p - \mu_{V_O}^L - 2\mu_e^L. \quad (2.51)$$

At local equilibrium, we have

$$\mu_O^L + 2\mu_h^L = 1/2\mu_{O_2}^p + \mu_{V_O}^L + 2\mu_e^L. \quad (2.52)$$

we can convert the oxygen gas chemical potential into the effective, equilibrium oxygen ion, $\mu_{O,eq}^L$, in LSM (as determined by $\mu_{O_2}^p$ in pores):

$$\mu_{O,eq}^L = 1/2\mu_{O_2}^p + \mu_{V_O}^L + 2\mu_e^L - 2\mu_h^L, \quad (2.53)$$

and the change in the free energy becomes

$$\Delta_r G = \mu_O^L - \mu_{O,eq}^L. \quad (2.54)$$

Assuming dilute case or ideal species (no self-interaction), the reaction rate can be expressed in terms of concentrations:

$$J = -\frac{r_0}{RT}(\mu_O^L - \mu_{O,eq}^L) = -\frac{r_0}{RT} RT \ln\left(\frac{c_O}{c_{O,eq}}\right). \tag{2.55}$$

When c_O is close to $c_{O,eq}$, linearization $ln(x) = 1 - x$ applies, and the rate is now

$$J \approx -r_0\left(\frac{c_{O,eq} - c_O}{c_{O,eq}}\right). \tag{2.56}$$

The expression above also matches the common empirical form for oxygen surface exchange:

$$J_{se} = -k_{se}(c_{O,eq} - c_O), \tag{2.57}$$

where k_{se} is the exchange coefficient, $c_{O,eq}$ is the equilibrium oxygen ion concentration in LSM, and c_O is the oxygen ion concentration in LSM. Using Eq. 2.22, the equation above is expressed in terms of the oxygen vacancy site fractions:

$$J_{se} = \frac{k}{a^3 N_A}\left([\mathrm{V}_\mathrm{O}^{\bullet\bullet}]_L - [\mathrm{V}_\mathrm{O}^{\bullet\bullet}]_p\right), \tag{2.58}$$

where $[\mathrm{V}_\mathrm{O}^{\bullet\bullet}]_L$ is the oxygen vacancy site fraction in LSM and $[\mathrm{V}_\mathrm{O}^{\bullet\bullet}]_p$ is the effective oxygen vacancy site fraction as determined by oxygen concentration in pores. Note that $[\mathrm{V}_\mathrm{O}^{\bullet\bullet}]_L$ is the field variable coupled with Eq. 2.23. We refer to Poulsen's work [103] for determining the value of $[\mathrm{V}_\mathrm{O}^{\bullet\bullet}]_p$ at a given p_{O_2} in the atmosphere. Poulsen modelled the LSM defect chemistry based on several assumed defect generation mechanisms. Various defect populations were computed as a function of p_{O_2}, as shown in Fig. 2.4.3 (figure directly cropped from the referenced work). A linear function for $[\mathrm{V}_\mathrm{O}^{\bullet\bullet}]_p$ is roughly estimated in the range of $-15 < \log(p_{O_2}) < 0$ with the naked eye. This function serves to compute $[\mathrm{V}_\mathrm{O}^{\bullet\bullet}]_p$ at a given p_{O_2}, or vice versa.

For the charge transfer reaction, we resume to Eq. 2.39 as the starting point. Concentration changes may affect the reaction rate by altering the pre-exponential concentration terms ($[S_{r,p}]$) and the overpotential (η) in Eq. 2.39. We assume the pre-exponential concentration terms have negligible effect relative to the overpotential such that, effectively, the chemical con-

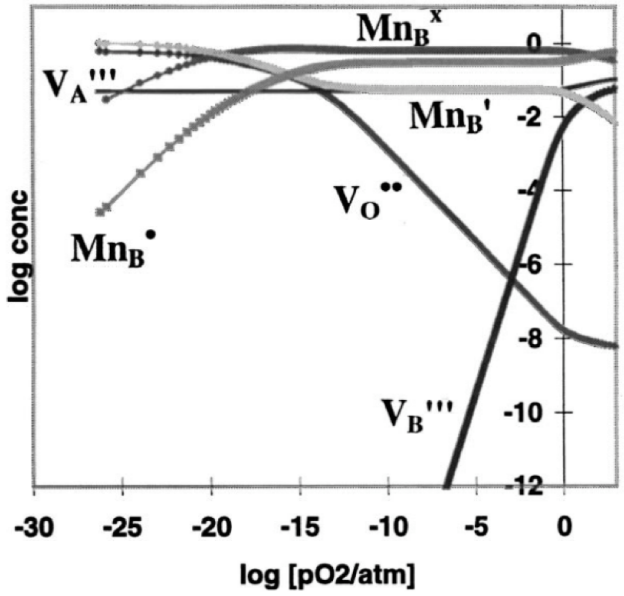

Figure 2.4.3: Figure 6 of the referenced work by Poulsen [103]. Various defect populations in $(La_{0.9}Sr_{0.1})_{0.95}MnO_{3\pm\delta}$ were computed as a function of p_{O_2}.

centrations are close to equilibrium ($Q \approx K$), as shown in

$$\frac{\prod_{r=1}^{P}[S_r]^{v_r}}{\prod_{r=1}^{R}[S_r]_0^{v_r}} \approx 1, \tag{2.59}$$

$$\frac{\prod_{p=1}^{P}[S_p]^{v_p}}{\prod_{p=1}^{R}[S_p]_0^{v_p}} \approx 1. \tag{2.60}$$

When this assumption is included into Eq. 2.39, the output is the Butler-Volmer equation for non-elementary equations. Thus, the current density of the charge transfer reaction at a given overpotential is

$$j_{ct} = j_{0,ct}\left\{\exp\left(\frac{\alpha z F \eta_{ct}}{RT}\right) - \exp\left(\frac{-(1-\alpha) z F \eta_{ct}}{RT}\right)\right\}, \tag{2.61}$$

where the overpotential is

$$\eta_{ct} = E_{ct,rev} - (\phi_{LSM} - \phi_{YSZ}). \tag{2.62}$$

The reversible potential, $E_{ct,rev}$, is dictated by local equilibrium at the LSM/YSZ interface. The expression for the reversible potential is

$$E_{ct,rev} = -\frac{RT}{4F} \ln \frac{p_{O_2,CE}}{p_{O_2,LSM}}, \tag{2.63}$$

where $p_{O_2,LSM}$ is the *effective* p_{O_2} in LSM based on the local value of $[\mathrm{V}_\mathrm{O}^{\bullet\bullet}]$ (in LSM). $p_{O_2,LSM}$ is calculated using the linear function based on Poulsen's work mentioned earlier.

The TPB phase, located at the intersection of the pores, LSM, and YSZ, consists of small mesh elements and appear to be an entanglement of thin strings throughout the cathode microstructure. All 3 field variables $(p_{O_2}, [\mathrm{V}_\mathrm{O}^{\bullet\bullet}], \phi_{YSZ})$ are defined in the TPB phase. Numerically, the TPB volume contains the source term that describes local ORR at the TPBs. Similar to our treatment of the charge transfer reaction, we again consider the Butler-Volmer equation with the assumption of negligible variation for the pre-exponential concentration terms to describe the reaction rate at the TPB volume:

$$s_{tpb} = s_{0,tpb} \left\{ \exp\left(\frac{\alpha z F \eta_{tpb}}{RT}\right) - \exp\left(\frac{-(1-\alpha) z F \eta_{tpb}}{RT}\right) \right\}, \tag{2.64}$$

where the overpotential is

$$\eta_{tpb} = E_{tpb,rev} - (\phi_{LSM} - \phi_{YSZ}). \tag{2.65}$$

Note that the reaction rate here is volumetric (A/cm^3). The exchange rate, $s_{0,tpb}$, can be derived from a measured lineal exchange current density, $j_{0,tpb}$ (A/cm). Miyoshi et al. [93] proposed an empirical formula for $j_{0,tpb}$ that specifically targets ORR at the TPB. Thus, the volumetric exchange rate is derived by writing

$$s_{0,tpb}[\mathrm{A/cm^3}] = j_{0,tpb}[\mathrm{A/cm}] \frac{L_{tpb}[\mathrm{cm}]}{V_{total}[\mathrm{cm^3}]} \frac{V_{total}[\mathrm{cm^3}]}{V_{tpb}[\mathrm{cm^3}]}, \tag{2.66}$$

where L_{tpb} is the TPB lineal length, V_{total} is the total volume, and V_{tpb} is the volume occupied by TPB voxels (after TPB relabelling algorithm). The corresponding units are include in square brackets. Similar to the previous

discussion on the charge transfer reaction, the reversible potential of the TPB reaction is

$$E_{tpb,rev} = -\frac{RT}{4F} \ln \frac{p_{O_2,CE}}{p_{O_2,pore}}, \tag{2.67}$$

where $p_{O_2,pore}$ is the field variable that describes p_{O_2} in pores.

2.4.6 Summary of System of Differential Equations

In summary, we first present the formalism for the bulk transport fluxes, whose expressions are

$$J_{O_2} = -\frac{D_{O_2}}{RT} \nabla p_{O_2}, \tag{2.68}$$

$$J_O = \frac{D_O}{a^3 N_A} \nabla [\mathrm{V}_\mathrm{O}^{\bullet\bullet}], \tag{2.69}$$

$$j_i = -\sigma_i \nabla \phi_{YSZ}. \tag{2.70}$$

We then introduce the formalism for the local reactions, whose rates are

$$J_{se} = \frac{k}{a^3 N_A} \left([\mathrm{V}_\mathrm{O}^{\bullet\bullet}]_L - [\mathrm{V}_\mathrm{O}^{\bullet\bullet}]_p \right), \tag{2.71}$$

$$j_{ct} = j_{0,ct} \left\{ \exp\left(\frac{\alpha z F \eta_{ct}}{RT} \right) - \exp\left(\frac{-(1-\alpha) z F \eta_{ct}}{RT} \right) \right\}, \tag{2.72}$$

$$s_{tpb} = s_{0,tpb} \left\{ \exp\left(\frac{\alpha z F \eta_{tpb}}{RT} \right) - \exp\left(\frac{-(1-\alpha) z F \eta_{tpb}}{RT} \right) \right\}. \tag{2.73}$$

The expressions above are combined in the form of the continuity equations for mass (and charge) conservation. The local conservation for pore, LSM, and YSZ are written as

$$\nabla \cdot J_{O_2} = -\frac{s_{tpb}}{4F}, \tag{2.74}$$

$$\nabla \cdot J_O = 0, \tag{2.75}$$

$$\nabla \cdot J_i = -s_{tpb}, \tag{2.76}$$

respectively. J_{se} and j_{ct} are not explicitly shown above. Since they are defined over 2D interfaces, they act as interface conditions (boundary conditions that couple separate mesh domains) for the numerical problem. It

is also important to point out that each transport/reaction rate is region-specific (phase-specific). For example, oxygen ionic flux in YSZ is not defined in pores and LSM. The term s_{tpb} is not defined (and hence zero) anywhere outside the TPB mesh elements.

2.4.7 Model Parameters

A detailed list of the model parameters are tabulated here. Note that in each simulation run, the electrochemical steady state under a range of model overpotential (η_{model}) is simulated.

Table 2.4.1: List of the model parameters and corresponding references.

Notation	Description	Value	Unit	Reference
T	Temperature	1073	K	-
η_{model}	Model (global) overpotential	varies (input)	V	-
$p_{O_2,c}$	Oxygen partial pressure at top of cathode	0.21	atm	-
$p_{O_2,CE}$	Oxygen partial pressure at counter electrode	1e-20	atm	-
E_{model}	Reversible cell potential (or OCV)	1.028	V	-
ϕ_{CE}	Potential at counter electrode	0	V	-
D_{O_2}	Oxygen gas diffusivity (at 1073 K)	0.64	cm^2/s	-
D_O	Oxygen diffusivity in LSM	7.5e-7	cm^2/s	[3]
σ_i	YSZ ionic conductivity	4e-2	S/cm	[52]
k_{se}	Chemical surface exchange coefficient	6.14e-6	cm/s	[127]
$j_{0,ct}$	Charge transfer exchange current density	0.193	A/cm^2	[36]
$j_{0,tpb}$	Lineal TPB reaction exchange current density	1e-7	A/cm^3	[93]
z	Number of electrons for TPB and charge transfer reaction	4	-	-
α	Symmetry factor TPB and charge transfer reaction	0.5	-	-

2.5 HPC Simulation

2.5.1 MOOSE and ERMINE

The model is numerically solved by the FE method based on microstructural meshes. The integration of the model formulation, boundary conditions, finite element discretization, and mesh information yields a nonlinear system of equations to be solved. One expects the numerical model to be relatively stiff for two main reasons:

- Large differences in the relative magnitude of transport/reaction coefficients exist between the phases. For example, the oxygen gas diffusivity is much larger than the YSZ ionic conductivity.

- A mesh built upon a highly interconnected network of pore, LSM, YSZ, and TPB phases requires a large number of elements that vary greatly in size. For example, the TPB volume mesh requires a large number of small elements, while the other volumes have similar numbers of generally larger elements.

A useful simulation tool should utilize massively parallel programming (MPP) techniques and be implemented on a high-performance computing (HPC) environment, to overcome the inherent challenge in the targeted simulations, and it should allow for high-throughput computations over many domains or many operational conditions, or both. Further, since many models of electrode performance include parallel and multi-step reaction-and-transport models, a useful simulation tool should allow for rapid inclusion of new physics.

We use an open-source FE framework (MOOSE, Idaho National Laboratory, Idaho Falls, ID) to instantiate and solve the numerical model. MOOSE is a C++ FE framework capable of MPP on HPC platforms, and it has been used to solve very complex models [34, 102] in neutronics and geophysics. It readily accepts user defined physics discussed earlier in a modular nature (user can toggle a certain physics, e.g, the surface exchange reaction, on and off), as well as the mesh types discussed in Sec. 2.3. The MOOSE framework is built upon the libMesh and PETSc libraries that enable automatic parallel computation through the Message Passing Interface (MPI) and multithreading. In other words, MOOSE provides MPP with minimal programming effort. The modular nature of the framework allows users to specify options such as solver type, preconditioning, the number of parallel cores used to solve the model, etc. Details for MOOSE can be found in [33] and `http://mooseframework.org`, and there is a substantial user network in the field of phase field modeling, neutronics and nuclear materials, and geophysics.

We developed an application (i.e., an extension of MOOSE for specific pur-

poses) from the MOOSE framework specifically for simulating SOFC electrochemistry in microstructural meshes. The application is named *ERMINE*, which loosely stands for **E**lectrochemical **R**eactions in **Mi**crostructural **Ne**tworks. Therefore, the meshed microstructure model developed for this work may simply be referred to as ERMINE in later sections. The ERMINE source codes are available at https://github.com/tim-hsu/ermine and in Appendix A.

2.5.2 Mesh Splitting

To our knowledge, in general, a normal FE simulation run in MOOSE may be carried out by multiple cores in parallel. However, each core would still hold an amount of memory roughly equal to the memory usage of the mesh (plus the amount for model computation). In this scenario, a 200-core simulation applied to a 1GB mesh may require beyond 200 GB of memory usage. Mesh splitting refers to dividing the microstructural mesh into multiple parts and is a way to distribute the memory usage of a mesh to multiple cores such that each core only holds a fraction of the memory of the mesh. This process can be simply implemented by a built-in executable binary file within the MOOSE framework and has been observed to be essential for memory-limited cluster nodes (under 64 GB). We have carried out simulations that theoretically access up to 1.5 TB of node memory, though a more robust benchmark of the actual memory usage has not been done.

2.5.3 Quasi-static Stepping Scheme

It should be noted that since ERMINE aims to solve a system of highly nonlinear equations at steady state, a good initial condition is critical to computation convergence. The easiest initial condition is the global equilibrium, where the net current output is zero and the values of the field variables are known everywhere in the domain. However, due to the nonlinearities, an incremental change in the model overpotential (especially beyond 0.1 - 0.2 V) can lead to drastic changes in the solution (from global equilibrium). Therefore, with an initial condition that is global equilibrium, solving for a steady state solution at an overpotential of 0.1 V or higher can be challeng-

ing. To this end, we have implemented a quasi-static stepping scheme to address the challenge.

With the quasi-static stepping scheme, ERMINE computes a series of steady state solutions along a range of overpotential. First, ERMINE computes a steady state solution at a low overpotential, and saves the solution as the initial condition. This initial condition is then used for another computation at a slightly higher overpotential. The process repeats as the overpotential increments to a high enough value. Using the quasi-static scheme, we are able to obtain a solution at $\eta_{model} = 0.4V$, which is relatively large compared to typical operating conditions (about 0.2 V). An added benefit for using this scheme is that for each simulation run, ERMINE can efficiently generate a current-voltage curve (from 0 to 0.4 V of overpotential), which is one of the most common types of data regarding SOFC performance.

2.5.4 Joule and Bridges

We implemented the ERMINE application on laptops and workstations for the testing and debugging stages. Two supercomputers were used for the production stage: Joule (National Energy Technology Laboratory, Morgantown, WV) and Bridges (Pittsburgh Supercomputing Center, Pittsburgh, PA). Typically, for domains of 10 x 10 x 10 μm^3 (exactly the size of the subvolume in Fig. 2.3.5 with a mean particle size of 0.46 µm), a suitable number of cores is about 256. So far, increasing the domain size has not led to a substantial increase in simulation runtime (due to the increase in the number of cores used). The typical runtime for a such subvolume may range from ten minutes to 1–-2 hours, making the high-throughput workflow (simulating tens or hundreds of subvolumes from a queue) a reality.

2.5.5 Simulation output and visualization

Fig. 2.5.1 shows several different aspects of the simulation output based on the microstructure subvolume shown in Fig. 2.3.5. The simulation was run on Joule using 256 cores, with the model parameters and the boundary conditions listed in Table 2.4.1. The runtime was about 30 minutes. The output consists of fields of local variables (p_{O_2}, $[\mathrm{V}_\mathrm{O}^{\bullet\bullet}]_L$, and ϕ_{YSZ}) that are

discretized and evaluated at the nodes of the microstructure mesh elements. Fig. 2.5.1a,b,c,d show j_i in YSZ, η_{tpb} at TPBs, p_{O_2} in pores, and ϕ_{YSZ} in YSZ, respectively. Quantities such as p_{O_2} and ϕ_{YSZ} were directly solved during the simulation, while j_i and η_{tpb} were computed during post-processing using Paraview (Kitware Inc., Clifton Park, NY and Sandia National Laboratories, Albuquerque, NM).

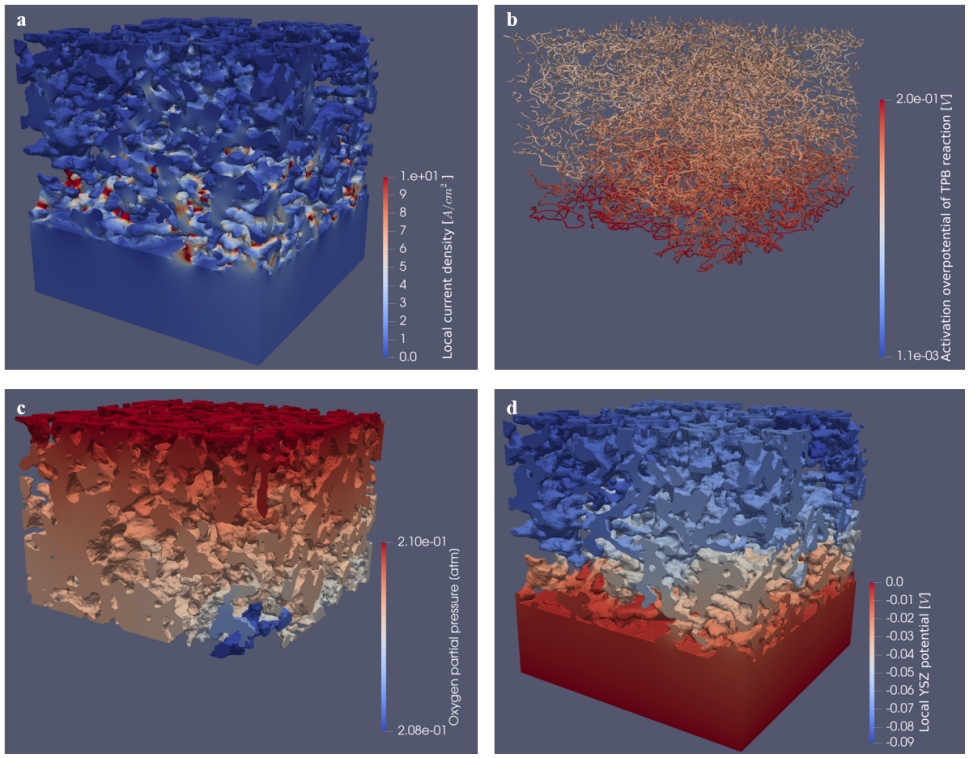

Figure 2.5.1: Simulation output as evaluated at the mesh element nodes when $\eta_{model} = 0.2$, rendered in Paraview. The individual mesh elements are not visible here due to the rendering mode. (a) local current density in YSZ. (b) local activation overpotential at the TPB phase. (c) oxygen partial pressure in pores. (d) Local potential in YSZ. Color indicates magnitude of the shown quantities.

For effective medium models, since the computational domain (in whatever dimensions) is not coupled to local microstructural phase distributions/morphologies and is instead assumed to be a homogenized continuum, smooth gradients of performance metrics are expected in the simulation

output. However, for ERMINE, due to the discrete nature of the computational domain, significant local variations (fluctuations) of performance metrics are expected. For instance, in the case of observing local activation overpotentials at TPBs (η_{TPB}), an effective medium model outputs a smooth-transitioned distribution of η_{TPB} along the electrode thickness (regardless of 1D, 2D, or 3D simulations). In contrary, ERMINE's simulation output of η_{TPB} is spatially coupled to only the TPBs. This example is illustrated in Fig. 2.5.2, where the expected simulation output on η_{TPB} (its value is represented by the color) are shown for an effective medium theory (EMT) model (the EMT model output is schematic; it is not based on real simulation data) and for ERMINE (based on actual simulation data). The EMT model output would contain a smooth-transitioned η_{TPB} distribution, but the ERMINE simulation output retains as much spatial/locality information as possible by computing η_{TPB} only at the relevant microstructural features (i.e., the TPBs). The ERMINE simulation output contains significant vertical and lateral variations in η_{TPB}, which will be discussed in Sec. 4.4.3. These local variations are expected to impact local variations in performance and degradation, such as chromium poisoning.

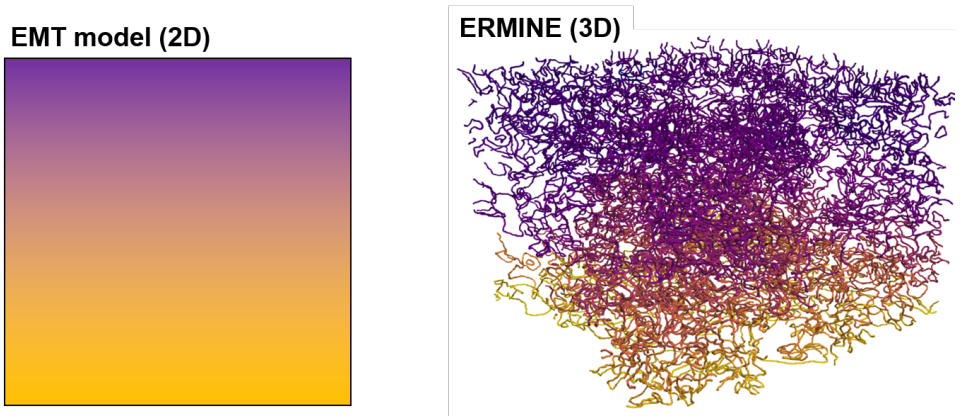

Figure 2.5.2: Example difference in simulations outputs of EMT model vs. ERMINE for the case of η_{TPB}. The color denotes value of η_{TPB}.

Although ERMINE computes fields of local electrochemical quantities, effective performance metrics can be quantified. For instance, we can cal-

culate the current density flux through the bottom plane of the electrolyte (i.e., overall current exiting the computational domain) by integrating the local fluxes of j_i over the plane area. This quantity, j_{model}, varies with the model overpotential, η_{model}. Therefore we can plot the effective performance (current output vs. applied overpotential, or j-V) of the cathode microstructure. The j-V curve is one of the most common descriptor for a cell's performance. The j-V curves, along with other more in-depth analysis, of various microtructures will be shown in later chapters.

2.5.6 Convergence and Heterogeneity

Large-scale heterogeneities in the commercial cell cathode microstructures (can be seen in Fig. 2.2.1b) have been found to cause numerical convergence issues. Such heterogeneities, in a small-to-medium subvolume, become extreme cases of over-abundance of only one phase (e.g., very large LSM or YSZ boulder). Since during simulations, the convergence criterion pertains to the residual error for species transport equations corresponding to all three phases (plus the TPB phase), the large-scale heterogeneities is likely to misrepresent the balance of proportions of the three phases and contribute to unbalanced residual error for the convergence criterion. Subsequently, only the regions of the cathode microstructure without the large-scale heterogeneities typically result in converged simulations. This presents some level of bias in the simulation data for the cathode microstructure, because the large-scale heterogeneities are excluded in later analyses. While future investigations should tackle this issue, the converged simulations present unique insight into local performance and highlights differences between commercial cell heterogeneities and synthetic microstructure heterogenetities.

3

Preliminary Results and Model Validation

3.1 Simulations using Toy Models

Initial testing of the simulations was carried out using toy model meshes, one of which is described in Sec. 2.3.1. These simulations were used to ensure that the different physics were properly encoded and were successfully converging, producing expected results. We describe two types of toy models below. The first is based on a cylindrical mesh containing an axial TPB that intersects the upper and lower bounds of the domain in a perpendicular fashion (see Fig. 2.3.1). The axial TPB toy model is exercised using TPB, MIEC, and combined TPB and MIEC pathways. Simulations were carried out in each case to qualitatively demonstrate the simulations worked as expected. For the second toy model type, simulations only involve an isolated phase (pore, LSM, or YSZ can be isolated from percolation). The isolated phases and their effects on the simulations were investigated.

3.1.1 Axial TPB Model

The mesh used here was discussed in Sec. 2.3.1. The values used in the model were designed to test the simulations, not to compare directly to SOFCs. The model parameters correspond to Table 2.4.1. The simulations were run on a laptop using four cores, and converged very quickly (approximately five minutes) due to the simplicity of the toy mesh.

Four scenarios were simulated based on the axial TPB mesh. In the first scenario, only the TPB pathway is enabled. In the second, only the MIEC pathway is enabled. In the third, both pathways are enabled. Finally, in the fourth, only the MIEC pathway is enabled, *but* three model parameters, which are D_O (oxygen diffusivity in LSM), $j_{0,ct}$ (charge transfer exchange current density), and k_{se} (chemical surface exchange coefficient), are increased by three orders of magnitude (1000 times the values shown in Table 2.4.1). These three parameters are all involved in the MIEC pathway. Thus increasing the three parameters would lead to faster transport and reaction rates through the MIEC pathway.

The model outputs are visualized in Fig. 3.1.1, which shows the YSZ potential distribution at $\eta_{model} = 0.4V$. It can be seen that for simulations involving the TPB pathway, most of the potential gradient radiates from the central TPB. This potential gradient is less obvious for simulations involving only the MIEC pathway, in which case the potential gradient has both lateral and vertical components. As it turns out, the current density output from the MIEC pathway is negligible relative to the TPB pathway. This would make sense because LSM is not known to be an excellent MIEC. In addition, the surface areas in the TPB axial model are fairly minimal and certainly not conducive to MIEC pathway. Table 3.1.1 shows the average current density (through the YSZ phase at the bottom plane) in each scenario at $\eta_{model} = 0.4V$.

Table 3.1.1: Average current density over YSZ bottom plane at $\eta_{model} = 0.4V$ in each scenario of the axial TPB model.

	TPB	TPB + MIEC	MIEC	fast MIEC (1000 X)
Current Density (A/cm^2)	0.63	0.63	9.2e-6	8.8e-3

Increasing MIEC pathway-related rate coefficients leads to a faster overall performance. This demonstrates the flexibility of ERMINE. We may investigate cases when the MIEC pathway (or both TPB and MIEC) is dominant by simply adjusting the model parameters. The same can be done when investigating different materials that relate to different rate coefficients (e.g., LSCF, which has a much faster oxygen diffusivity than that of LSM).

To further demonstrate that the axial TPB model produces results within our expectation, the potential gradient vectors are visualized based on the TPB and the MIEC scenarios, as shown in Fig. 3.1.2. The potential gradient vectors, or effectively, the oxygen ion flux vectors, are represented by the arrows in the figure. It can be seen that for the TPB pathway, the flux originates from the TPB and converges down towards the electrolyte/bottom of the domain. For the MIEC pathway, the flux originates from the left side of the YSZ phase (the LSM/YSZ interface), and converges towards the electrolyte. The figure demonstrates the physical correctness of ERMINE manifest in the axial TPB mesh with a simple geometry.

3.1.2 Isolated Phases

Isolated phases, those that are not connected to the boundary conditions, pose a challenge to the convergence of the simulations. To demonstrate this, we used another toy model where a spherical isolated phase existed within the volume of a connected phase. The mesh used in this simulation is shown in Fig. 3.1.3. The rate coefficients used in the simulations correspond to Table 2.4.1. Note that both the TPB and the MIEC pathways are enabled. The simulations were run with different initial conditions and boundary conditions to explore the impact of isolated phases on numerical convergence. The general conclusions that will be made are: for many initial/boundary conditions, isolated phases have an effect of stalling the simulation convergence to an appropriate steady state, and their exclusion does not pose a major issue to the final expected solution.

A few details are mentioned here regarding the aforementioned conclu-

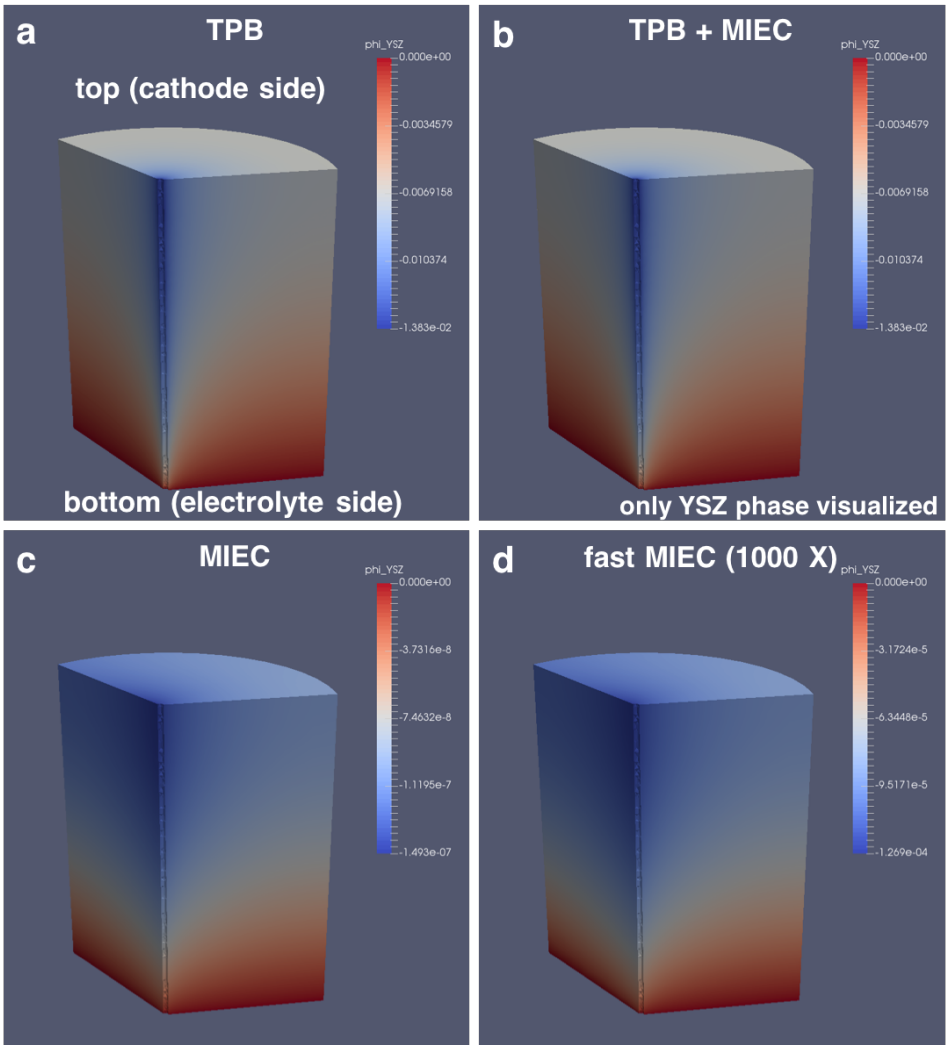

Figure 3.1.1: Visualization of axial TPB model output. Color indicates the YSZ potential (V) distribution at $\eta_{model} = 0.4V$. Only the YSZ phase is shown. The simulations are run with parameters shown in Table 2.4.1, except for (d), where MIEC pathway-related rate coefficients are increased (see section above). Four scenarios are simulated depending on what pathways are enabled. These scenarios are (a) TPB, (b) TPB and MIEC, (c) MIEC, and (d) fast MIEC pathways enabled.

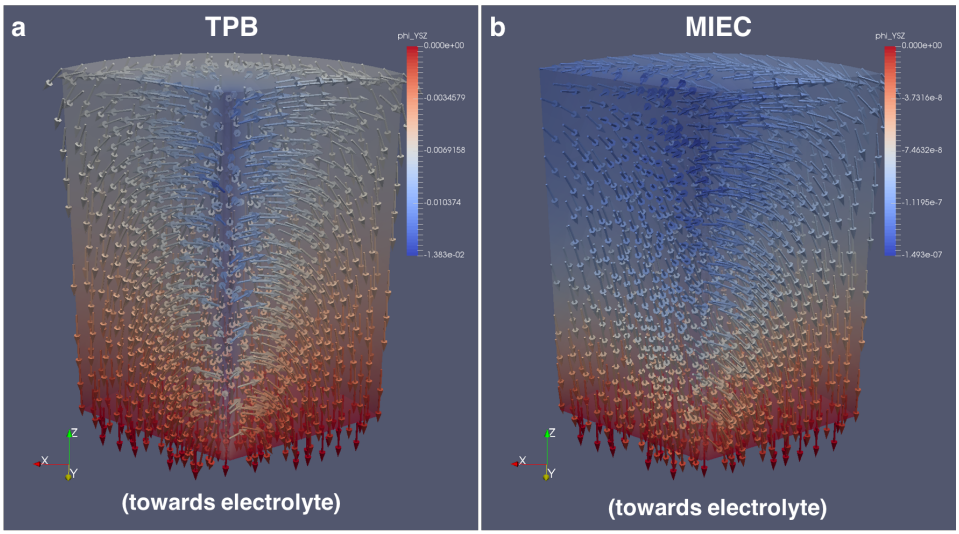

Figure 3.1.2: Visualization of oxygen ion flux from the TPB and the MIEC scenarios of the axial TPB model output. Color indicates the YSZ potential (V) distribution at $\eta_{model} = 0.4V$. Only the YSZ phase is shown with a degree of transparency. The potential gradient vectors, or effectively, the oxygen ion flux vectors, are represented by the arrows. Two scenarios from the axial TPB model are presented, which are (a) the TPB and (b) the MIEC pathways. The arrows only represent flux directions, not magnitudes (they are not to scale).

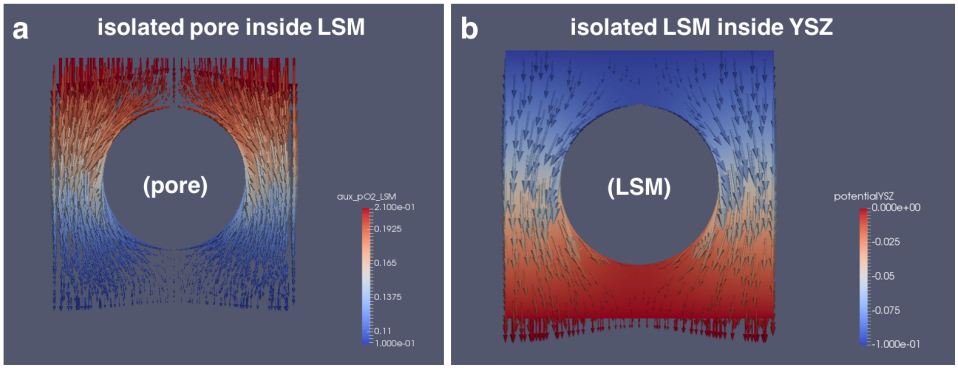

Figure 3.1.3: Visualization of species flux in a matrix phase surrounding an isolated phase. Two cases are shown here, which are (a) an isolated pore surrounded by LSM and (b) an isolated LSM surrounded by YSZ. The color indicates (a) the effective oxygen partial pressure (atm) in LSM and (b) the YSZ potential. The arrows represent directions of (a) oxygen flux in LSM and (b) oxygen flux in YSZ. The lengths of the arrows are scaled to the local flux magnitudes.

sions. Fig. 3.1.3 show two cases when the appropriate steady state is achieved with proper initial/boundary conditions. The two cases are (a) an isolated pore surrounded by LSM and (b) an isolated LSM surrounded by YSZ. The color indicates (a) the effective oxygen partial pressure (atm) in LSM and (b) the YSZ potential. The arrows represent directions of (a) oxygen flux in LSM and (b) oxygen flux in YSZ. Note that the lengths of the arrows are scaled to the local flux magnitudes. It can be seen that at steady state, no observable flux flows through the isolated phase for either case. Thus, the isolated phases are not a favorable pathway. Similar observations were made for several other cases (e.g., isolated pore in YSZ). For many initial/boundary conditions tested during the simulations, an appropriate steady state could not be achieved. This is best explained by a specific example, such as an isolated pore inside LSM, which is also shown in Fig. 3.1.3(a). It was observed that the surface exchange across pore/LSM is an extremely slow process compared to the bulk transports. When the initial/boundary conditions produce a state far from equilibrium such that the isolated pore needs to be equilibrated to the surrounding LSM, the surface exchange is not fast enough to allow this equilibration within any reasonable runtime. However, we already know the outcome at steady state, where the flux across the pore/LSM interface is negligible. Therefore, we may simply discard the isolated pore for future simulations. The same decision was made regarding the isolated LSM and YSZ phases.

3.2 Initial Simulations using 3D Reconstructions of Physical Microstructures

In the first series of experiments to demonstrate the applicability of our computational method to simulate electrochemistry using 3D reconstructions of physical microstructures, we investigated three small sub-volumes of the MSRI cathode from the PFIB data (Fig. 2.2.1(b)). After demonstrating convergence, we made an initial comparison between a continuum model and our meshed model for the three different subvolumes. We found a discrepancy between the two model outputs with respect to the order of relative performances, indicating the subvolumes do no conform to assump-

tions of effective medium theory, even though they should according to their particle sizes. Put another way, the order of performances from the three microstructures based on the continuum model is different from that based on the ERMINE model. A qualitative observation is made to explain this discrepancy, supporting the breakdown of assumptions built into the continuum model.

3.2.1 Methods

Three 5 x 5 x 5 μm^3 subvolumes with different TPB densities were extracted from the MSRI cathode microstructure shown in Fig. 2.2.1b. The TPB densities are significantly different based on the TPB density histogram shown in Fig. 3.2.1, which comes from 700 5 x 5 x 5 μm^3 subvolumes of the cathode microstructure data. The TPB densities, measured in volumetric densities ($\mu m/\mu m^3$), were computed using an in-house algorithm described elsewhere [26]. The TPB density is one of the most important parameters as a measure of electrochemical activity. Similarly, for the continuum model that we chose, the TPB density is one of the most influential parameters in determining the electrode performance. The continuum model used here is called the modified Tanner-Fung-Virkar (m-TFV) model, which yields area specific polarization resistance based on effective properties such as TPB density, YSZ tortuosity, and YSZ volume fraction. Details of the original TFV model and the m-TFV model can be found elsewhere [13, 18, 48, 115, 118, 126]. The result of the m-TFV model based on the selected subvolumes was provided by Rubayyat Mahbub, a doctoral researcher within the same department at Carnegie Mellon University (CMU).

The segmented microstructures were conditioned and meshed, as described in Sec. 2.3.2. These steps took about 15 minutes per subvolume. Simulations were run for each meshed microstructure, using parameters described in Table 2.4.1. As mentioned in Sec. 2.5.3, the simulations began from a small overpotential. Steady state solutions were obtained as the overpotential increments to 0.4 V. The average current density across the bottom-plane of the electrolyte was calculated at every simulation step, using a postprocesser readily available from MOOSE. Based on these simulations, j-V (current

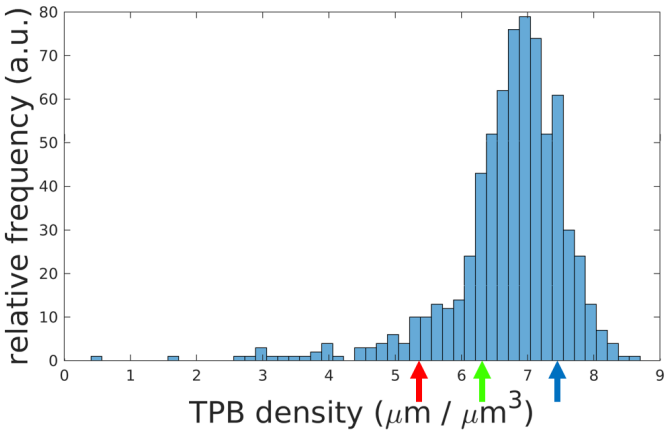

Figure 3.2.1: TPB density histogram based on 5 x 5 x 5 μm^3 subvolumes cropped from MSRI cathode shown in Fig. 2.2.1b. Three subvolumes were selected for an initial study. The arrows correspond to the TPB densities of the three subvolumes.

density vs. cell voltage) curves were generated. This process resulted in carrying out 10-15 simulations per subvolume, or overall 30-45 simulations. Simulations were run on a workstation at CMU, using 32 cores in parallel mode. Individual simulations generally converged in approximately 10 - 15 minutes and the entire set of simulations was run in an hour. These numbers are promising for running high-throughput automated simulations on large volumes of experimental microstructures.

3.2.2 Result and Discussion

The j-V results of this initial study are shown in Fig. 3.2.2, where the lines denote the interpolated result of the actual data, given in open symbols (as denoted in the caption). The results of the m-TFV model are given in closed symbols at 1 A/cm^2, and are linear (from the OCV value). Note that there is a significant difference between the voltages from the two models at the same current density, but this is not unexpected. This can be attributed to the two models not having exactly the same operating conditions or assumptions. For example, the electrolyte layer is involved in ERMINE, but not in the m-TFV model. Rather than focusing on this absolute difference, the attention here should be placed on the order of performances from each

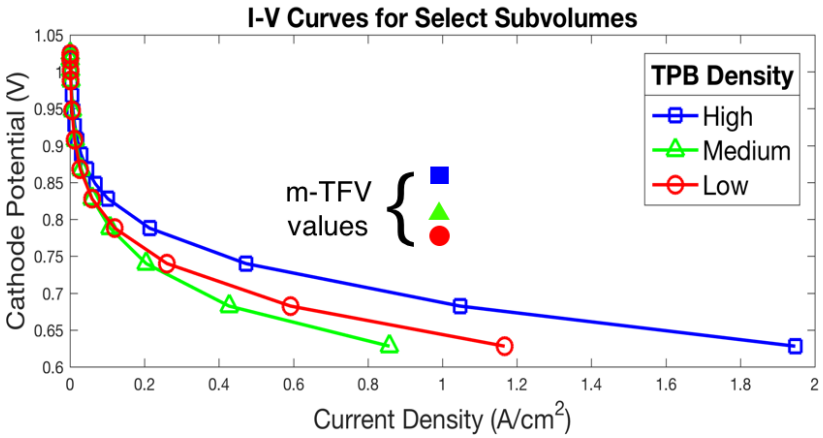

Figure 3.2.2: Current-voltage (I-V) curves from the m-TFV model and the meshed model based on the three subvolumes with sigficantly varied TPB densities. The meshed model result is shown in open markers (unfilled), and the m-TFV model in closed markers (filled). The m-TFV model result was evaluated only at a current density of 1 $\mathrm{A/cm^2}$, whereas in ERMINE the local electrochemistry was evaluated from 0 to 0.4 V of overpotential. Legend indicates relative TPB density magnitude, which can also be indicated by colors. Blue, green, and red are high, medium, and low TPB densities, respectively.

model. One generally expects higher performance from subvolumes with higher TPB densities, as is the case for the m-TFV model. For the ERMINE model, the subvolume with the highest TPB density does have the highest performance. However, the subvolume with the medium TPB density has the lowest performance, while the subvolume with the lowest TPB density has an intermediate performance. This discrepancy indicates that the subvolume microstructures do not conform to the assumptions of the effective medium theory (m-TFV model) and can be explained by examining the subvolume microstructures.

The microstructures of the three subvolumes are shown in Fig. 3.2.3, where only the YSZ phase is shown and the color indicates the YSZ potential, locally. Darker blue regions are operating at higher overpotentials, generally indicating a poor local performance. It can be seen that the subvolume with the high TPB density has the most uniform phase distribution of YSZ, of the three volumes. It also has the smallest volume of dark blue YSZ, located

at the back top corner. On the other hand, the subvolume with the lowest TPB density has the most heterogeneous YSZ phase distribution, with a large absence of YSZ at the cathode (top back) and some at the electrolyte (bottom front). There is a large volume of blue YSZ in the front corner, running from the top of the cathode to at least half the thickness. This explains the lower performance of this subvolume from the prior one. However, the lowest performance comes from the subvolume with the medium TPB density. While this subvolume has a higher degree of microstructural uniformity in the YSZ phase distribution than does the previous subvolume, there is a substantial gap of YSZ in the active cathode at the interface of the electrode and electrolyte. This results in the poorest YSZ connectivity to the electrolyte (least amount of interfacial area between cathode YSZ and electrolyte YSZ). As such, there is a large volume of blue YSZ that dominates the volume of this region (all oxide ions have to go through a small interfacial area that is not readily accessed in this volume). This supports the result that it has the lowest performance of all three subvolumes. This also supports that the experimental microstructures do not conform to assumptions of effective medium theory models, at least not within a volume of 5.0 x 5.0 x 10.0 μm^3 (the cathode size is 5.0 x 5.0 x 5.0 μm^3).

By examining the microstructures, we have shown that ERMINE takes into account the effect of morphologies (in this case the YSZ connectivity) on electrochemistry, whereas the m-TFV model, an instance of continuum models based on effective medium theory, neglects to account for the specifics of YSZ connectivity. The meshed model takes a more comprehensive approach in computing electrochemistry than the continuum modeling (where only a finite number of effective properties are extracted from the microstructure) does. In conclusion, the qualitative observation in this initial study supports the hypothesis that the meshed model may be more suitable to describe local electrochemistry in SOFCs, especially when the microstructural heterogenity can significantly impact the local electrochemistry. And, importantly, there are significant levels of microstructural heterogeneities in the MSRI cells that impact electrochemistry over the 5 µm length scale.

As will be shown in a later chapter, ERMINE is also compared to another

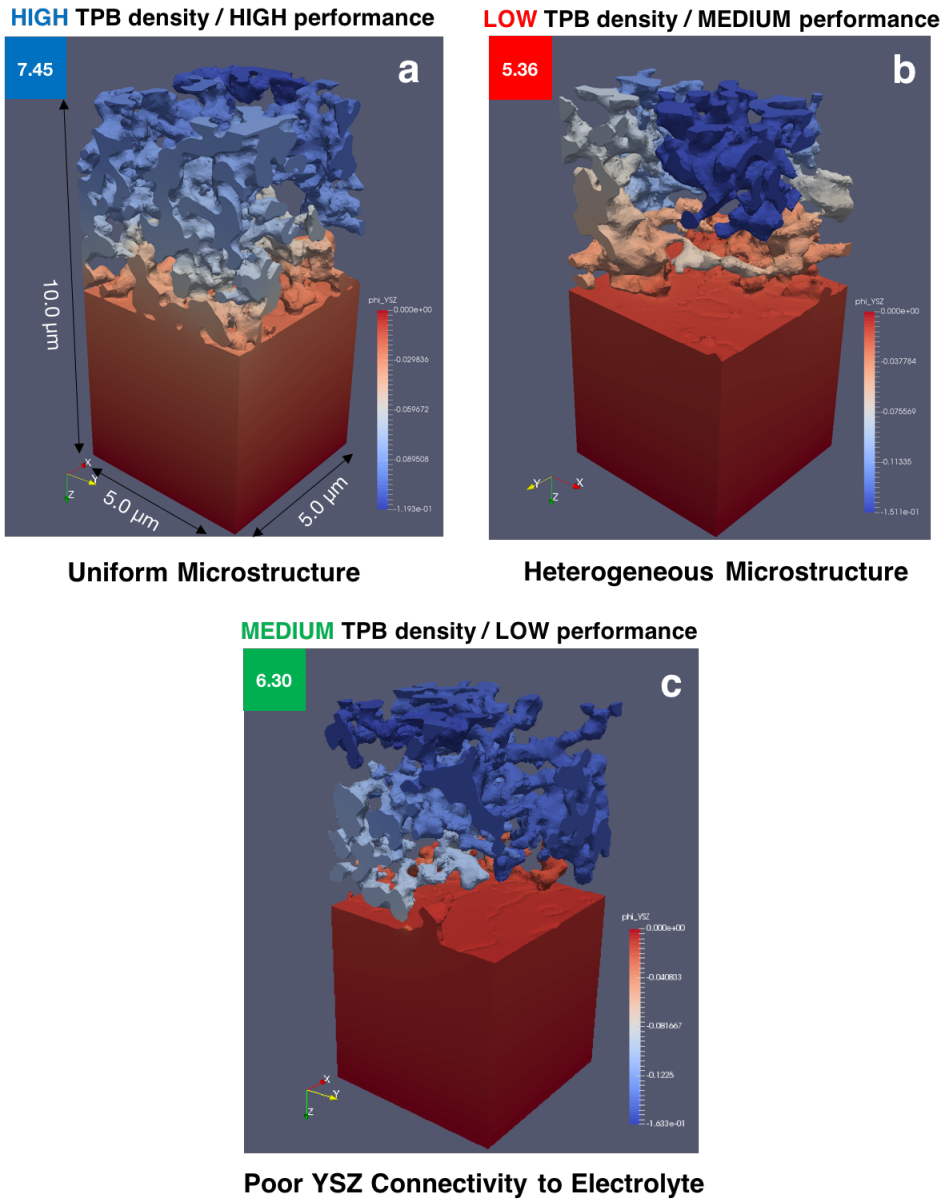

Figure 3.2.3: Meshed microstructural domains based on the selected subvolumes for the first study. The TPB densities, given in $\mu m/\mu m^3$ and shown at the top left corner of each microstructural domain, are (a) high, (b) low, and (c) medium in the figure. Only the YSZ phase is visualized. Colorbar indicates electric potential in YSZ. All three domains have the same dimensions, which are 5.0 x 5.0 x 10.0 μm^3.

effective medium model that has been validated and published [85, 86]. This comparison further supports the validation of ERMINE to produce reasonably accurate electrochemical fields accounting for morphological complexities. See further details in Chapter 4.

3.3 Russian Doll (Nested Subvolumes) Simulations

While the initial simulations presented in the last section clearly show promise for high-throughput simulations of large volumes of SOFC electrodes, it also showed that 5.0 x 5.0 x 10.0 μm^3 volumes do not conform to effective medium theory models. Furthermore, it is not clear that 5.0 x 5.0 x 10.0 μm^3 volumes are appropriate as representative volume elements to describe local electrochemistry. Therefore, the effect of the length scale of the computational domain on the simulated electrochemistry is further investigated in this second study. While the last study considered three microstructures and 40 simulations in total, the current study looks into 150 meshed microstructures, with a goal to run for 10 - 15 simulations on each, individually. To carry out this study, we implemented a high-throughput workflow using scripted ScanIP+FE meshing on a workstation at CMU and automatically queued simulations on the Joule supercomputer at NETL, demonstrating the feasibility of such large scale computational experiments in reasonable time frames. We call this study the Russian Doll study because we consider three nested subvolumes within a larger subvolume, like the famous Russian dolls. We consider nested sub-volumes of different length scales, which are about 5, 7.5, and 10 µm on an edge length. The result suggests indicate clearly that 5 µm is not appropriate for describing the local electrochemistry and suggest 10 µm or above is necessary in the physical microstructures.

3.3.1 Method

The simulations are based on the same cathode microstructure as the first study (the PFIB cathode data from Figure 2.2.1(b)). 50 non-overlapping subvolumes, which are about 12.5 x 12.5 x 12.5 μm^3 in size, were extracted from the microstructure. Each of the subvolumes is further broken down into a set of cubic subvolumes of varying sizes in a similar fashion to a

Russian doll set. This process is illustrated in Fig. 3.3.1, where smaller subvolumes of three different sizes are extracted from the larger subvolume, and only the 10, 7.5, and 5 µm boxes from the larger 12.5 µm cube are shown (because that is all that will be discussed here).[1] In other words, each Russian doll set consists of three cubic subvolumes, whose edge lengths are 10, 7.5, and 5 µm, respectively. Note that for each Russian doll set, the center of the bottom plane (or the cathode/electrolyte interface) stays at the same location (which is the central 5 x 5 μm^2 area of the original 12.5 μm^3 volume). One can describe the Russian doll set as shrinking the largest subvolume from the top and the sides, but not the bottom.[2]

There are a total of 150 subvolumes for these simulations. Each subvolume was conditioned (sequential dilation, append electrolyte layer, label and discard isolated phases, label TPB voxels) as described in Sec. 2.3.2. Again, as described in Sec. 2.3.2, these processes took fairly minimal time relative to meshing and simulations. The conditioning can be done within five minutes per subvolume.

Each of the 150 subvolumes was then meshed using high-throughput scripting with ScanIP+FE meshing on a workstation at CMU. Meshing for the 5, 7.5, and 10 µm subvolumes took approximately 10, 20, and 40 minutes, respectively, per subvolume. Thus the complete meshing time for the 150 subvolumes took about 58 hours (or 2.4 days), and was fully automated. Typical meshing durations and the numbers of mesh elements for these meshes are given in Table 3.3.1.[3] Note that these numbers may vary greatly depending on the microstructural heterogeneity.

The meshes were used as domain inputs to ERMINE, which runs in MOOSE and is implemented on Joule. The number of parallel cores requested for the 5, 7.5, and 10 µm subvolumes were 16, 32, and 64, respectively. Simulations were run using parameters described in Table 2.4.1.

[1] The exact edge lengths for the cubic subvolumes are 9.9, 7.4, and 4.8 µm.

[2] The bottom side refers to the side closet to the electrolyte, and the top side refers to the side furthest from the electrolyte.

[3] In fact, 12.5 µm volumes were meshed and submitted for simulations, as well. However, the mesh files from 12.5 µm volumes are so large such that the memory requirement for the simulations exceeded 64 GB, which is the limit for Joule.

Table 3.3.1: Meshing durations and numbers of elements for the meshes in the Russian doll study.

Domain Size (µm)	Number of Elements (millions)				Duration (minutes)
	pore	LSM	YSZ	TPB	
5	0.4	0.3	0.4	0.2	10
7.5	1.3	1.1	1.1	0.6	20
10	2.8	2.3	2.3	1.2	40
12.5	5.8	4.6	4.2	2.4	80

As mentioned in Sec. 2.5.3, each simulation run results in a j-V (current density vs. cell voltage) curve from 0 to 0.4 V of overpotential. This process would carry out 10-15 steady state simulations per subvolume, and there are a total of 150 subvolumes. Therefore, if all simulation runs converged, there would be over 1500 steady state computations. When simulations converged, the runtimes of individual simulation runs (computing from 0 to 0.4 V of overpotential) for 5, 7.5, and 10 µm subvolumes were approximately 5-15, 20-30 , and 45-60 minutes, respectively. The simulations were submitted to a queue and were automatically instantiated in Joule.

3.3.2 Results and Discussions

Simulations were attempted for all 150 meshed subvolumes, but only 130 converged successfully. The success ratios (number of successful convergences to number of attempted simulations) for the 5, 7.5, and 10 µm subvolumes were 44/50, 45/50, and 41/50, respectively. Overall, 33 Russian doll subvolume sets yielded converged simulations at all three domain sizes. Note that the entire study, with the 130 sub-volumes each having 10 - 15 individual simulations, and including the conditioning and meshing of the microstructures, took only about two weeks to perform. Here we consider only the 33 russian doll sets that converged for all three subvolume sizes. The j-V curves for these are plotted, for each subvolume size, in Fig. 3.3.2.

It can be seen that for each subvolume size, there is a range of j-V curves among the 33 subvolumes. Also, as the size increases, the range narrows. This result is consistent with expectations based on the concept of a rep-

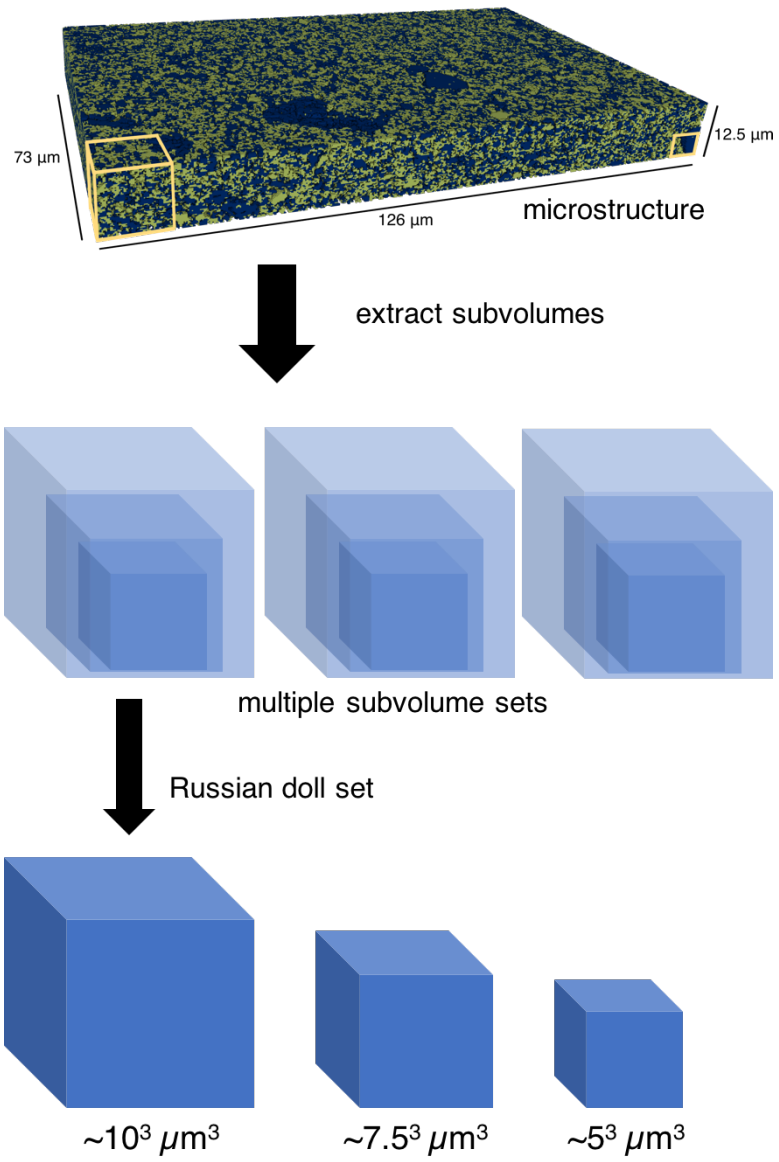

Figure 3.3.1: Schematic of Russian doll subvolumes extraction process. Multiple non-overlapping subvolumes are first extracted from a microstructure data. Analogous to a Russian doll set, smaller subvolumes are extracted from each larger subvolume. The subvolumes are cubic and their edge lengths are about 10, 7.5, and 5 μm.

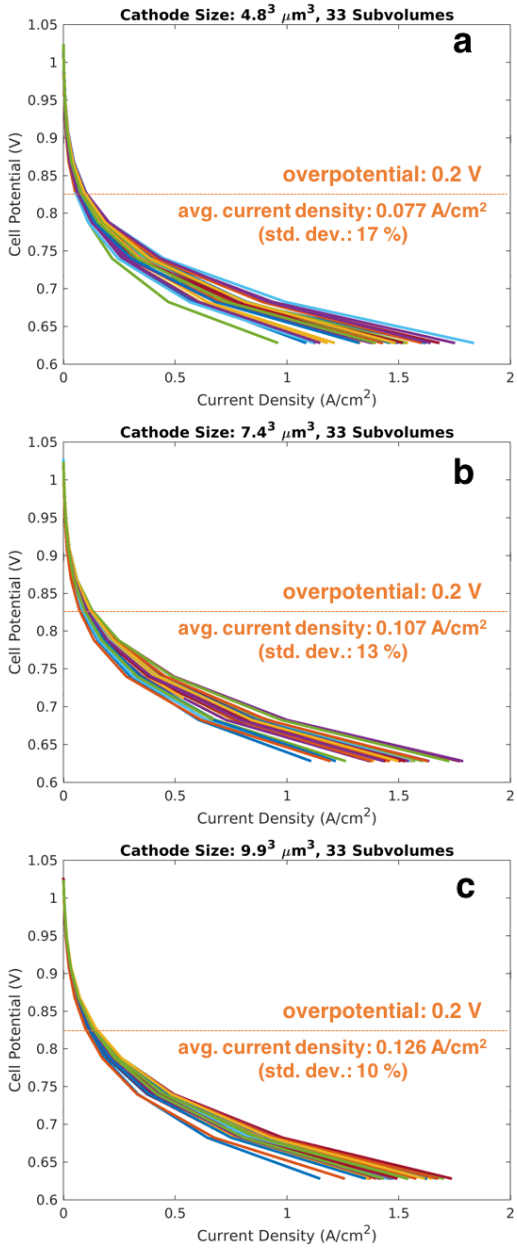

Figure 3.3.2: Current density-voltage curves for the second study. For each subvolume size, the I-V curves of the 33 simulations are plotted together. The cathode sizes are about (a) 5, (b) 7.5, and (c) 10 μm.

resentative volume element; larger subvolumes should lead to statistically more similar properties. The average current density, as well as the standard deviation among the current densities were evaluated at the overpotential of 0.2 V, which is a typical SOFC operating voltage. The standard deviations, calculated as percentages of the average current densities, decrease with increasing size but still remain substantial (10 %) at 10 µm. The average current density increases substantially with increasing subvolume size. This raises the question of whether 5 or even 10 µm is enough to describe local electrochemistry. To address this question, a number of qualitative observations regarding the microstructures were made.

One Russian doll set was chosen to illustrate the effect of subvolume size on the computed performance. This set of subvolumes, with the added electrolyte layers for the simulations, are visualized in Fig. 3.3.3. Again, only the YSZ phase is shown and the color represents the local potential (similar to Figure 3.2.3). Starting with the largest subvolume size (10 µm), the distribution of YSZ in the microstructure appears to be uniform, and the YSZ potential has a smooth gradient from top to bottom. As the size decreases, the YSZ phase distribution becomes less uniform and the YSZ potential drop becomes more discontinuous, or less smooth. At 5 µm, the YSZ potential drop is clearly abrupt over certain regions of the micrstructure. In fact, a closer examination of the 5 µm subvolume, as shown in (d), reveals that there is only a single thin YSZ channel (circled in red) connecting all the YSZ phase from top (the YSZ phase roughly in blue) to bottom (the YSZ phase roughly in red). In other words, all of the oxide ions generated from the ORR at the top region of the electrode have to transport through the thin channel to reach the electrolyte. However, this is not the case when viewing the microstructures in the larger subvolumes; there appear to be more alternative connections for ionic transport between top and bottom, resulting in smoother potential drop and improved performance.

This observation suggests that 5 µm is not an appropriate subvolume size for computing the local electrochemsitry. Based on the figure, 7.5 and 10 µm subvolumes appear to be more appropriate. However, there is still a wider distribution for the YSZ potential on the top surface of the 7.5 µm subvolume

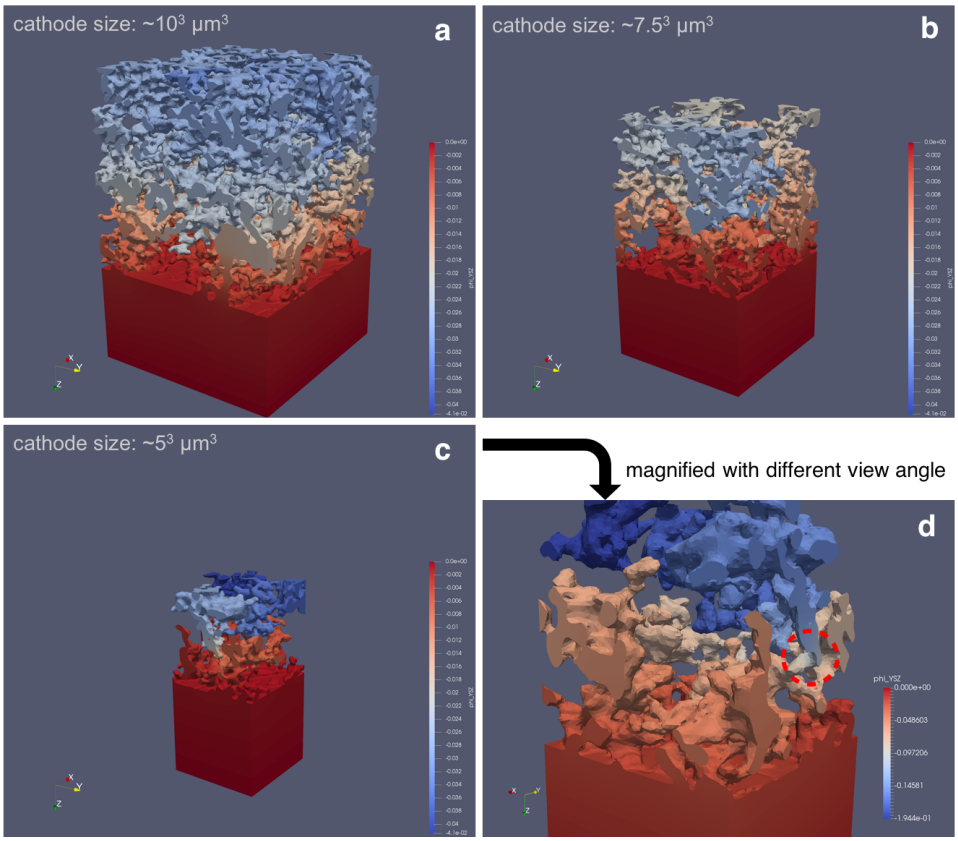

Figure 3.3.3: Visualization of the microstructures and the simulated YSZ potential from a set of Russian doll subvolumes. The subvolume sizes, excluding the 5 μm electrolyte layer, are (a) 10, (b) 7.5, and (c) 5 μm, respectively. Only the YSZ phase is visualized. The colorbar indicates YSZ potential. (d) is the same as (c) but viewed with a different angle, focusing on the thin channel of YSZ circled in red. This single YSZ channel connects all YSZ from top (the YSZ phase roughly in blue) to bottom (the YSZ phase roughly in red).

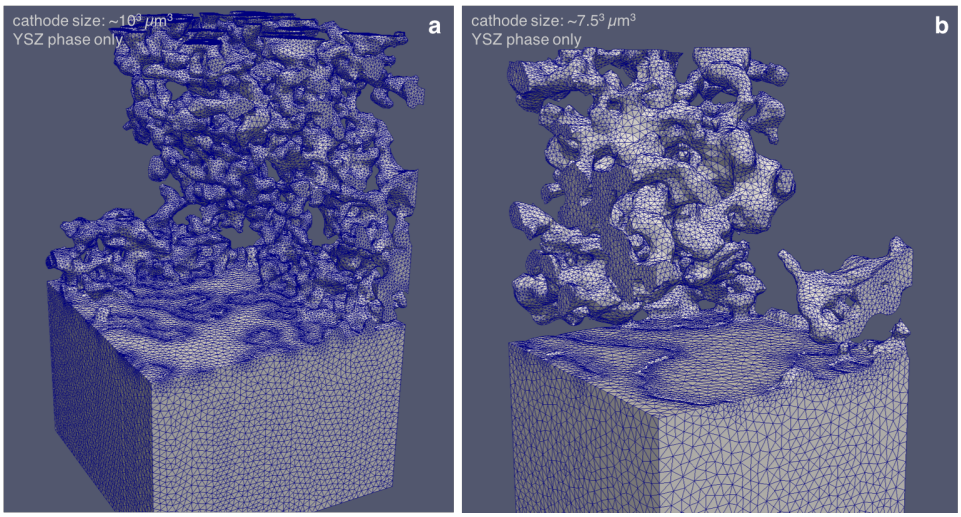

Figure 3.3.4: Visualization of two heterogeneous subvolumes from the Russian doll simulations. The two subvolumes did not result in converged simulations. The subvolume sizes are about (a) 10 and (b) 7.5 µm. Only the TPB phase is shown. The microstructures are rendered with mesh elements in the YSZ phase.

than for the 10 µm subvolume, indicating that the 10 µm subvolume is best. This explains the substantial increase in the average current density from 5 to 10 µm subvolumes. Further analysis and more quantitative results are necessary to determine the appropriate subvolume size to statistically describe local electrochemistry.

Finally, keep in mind that only 33 out of the 50 subvolumes result in converged simulations at all sizes. A significant portion of the unconverged simulations come from highly heterogeneous subvolumes. These subvolumes are likely to contribute to outlier performances and add to the standard deviations. Fig. 3.3.4 shows two examples of such subvolumes. There is a large absence of YSZ in both subvolumes. In such a case, the performance is likely to be extremely poor. Further work is necessary to investigate whether simulations on these subvolumes can reach a reasonably converged state.

3.4 Large-scale Subvolume Simulation

To further determine the appropriate size for a microstructure subvolume, a very basic Russian doll set of MSRI cathode subvolumes was simulated. Only two sizes were used: $10 \times 10 \times 7$ µm^3 and $30 \times 30 \times 7$ µm^3. Table 3.4.1 lists the computational difficulty (hardware resource and time) for the two simulations. It can be seen that a 9-fold increase in subvolume size can lead to a much more increase in overall time required for meshing and simulation. Nonetheless, such a large-scale subvolume can be meshed, split, and simulated within about a week.

Table 3.4.1: Relative computational difficulty for a large-scale subvolume

Size (µm^3)	# mesh elements	Mesh time	Mesh split time	# cores used	Run time
$10 \times 10 \times 7$	30 M	1 day	1 hr 36 mins	252	45 mins
$30 \times 30 \times 7$	130 M	5 days	19 hrs 28 mins	560	5 hrs 40 mins

With model parameters being the same, the two simulation results (j-V curves) are shown in Fig. 3.4.1. In terms of effective performance output, there is very little difference between the two. This suggests that the scale of the domain beyond 10 µm may have diminishing impact on the effective performance output, and that 10 µm may be large enough to describe the overall performance. However, a more robust investigation is necessary in order to better understand the impact of the domain scale on *local* electrochemical quantities.

3.5 Basic Scaling Test

In this section, a basic scaling test was performed to validate the necessity of HPC resources and the scaling capacity of ERMINE. A sample MSRI microstructure cathode subvolume mesh was used for the scaling test. Its physical size is $10 \times 10 \times 10$ µm^3 (including 3 µm electrolyte thickness), and its number of mesh elements is roughly 25–30 millions. The simulations were run on Bridges' regular compute nodes.

In parallel computing, the runtime of a (parallel) algorithm is the time

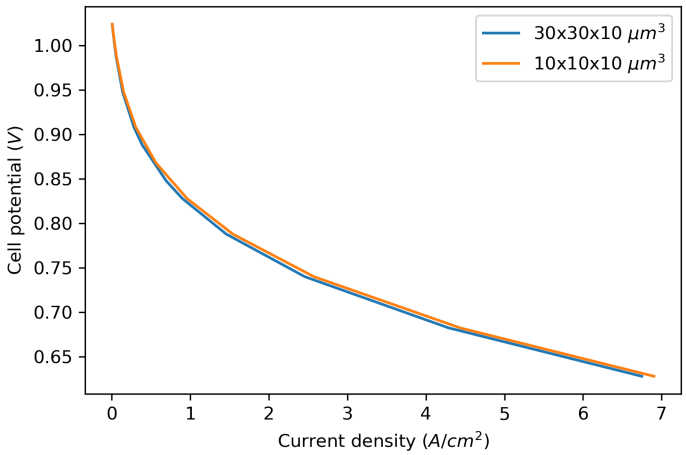

Figure 3.4.1: Comparison of the effective performance outputs (overpotential vs. current density) between the large-scale subvolume and the "regular " $10 \times 10 \times 7$ μm^3 subvolume. Note that the legend accounts for an appended electrolyte thickness of 3 μm, making the overall thickness 10 μm.

elapsed between the start of the (parallel) process and its termination. Fig. 3.5.1a shows the runtime as a function of the number of cores used (p). It is clear that the use of parallel cores can drastically reduce the runtime. In fact, the simulation could not be run serially (using only one core) or with small p; at $p = 4$, the simulation appeared to hang (convergence computation at extremely slow rate), the runtime exceeded the maximum allowed duration on Bridges' regular nodes (48 hours), and the simulation was subsequently forced to terminate. At high p, the runtime appears to converge to almost 0 hours, suggesting that this basic scaling test has not fully explored ERMINE's scaling capacity; a larger simulation domain size, with more complex geometries/physics may be simulated without much further difficulty.

A common measure of how parallelism may help faster execution is the Speedup, which can be defined as the ratio of the serial run time to the parallel run time

$$\text{Speedup} = T_s/T_p, \tag{3.1}$$

where T_s is the serial runtime, and T_p is the parallel runtime using p cores.

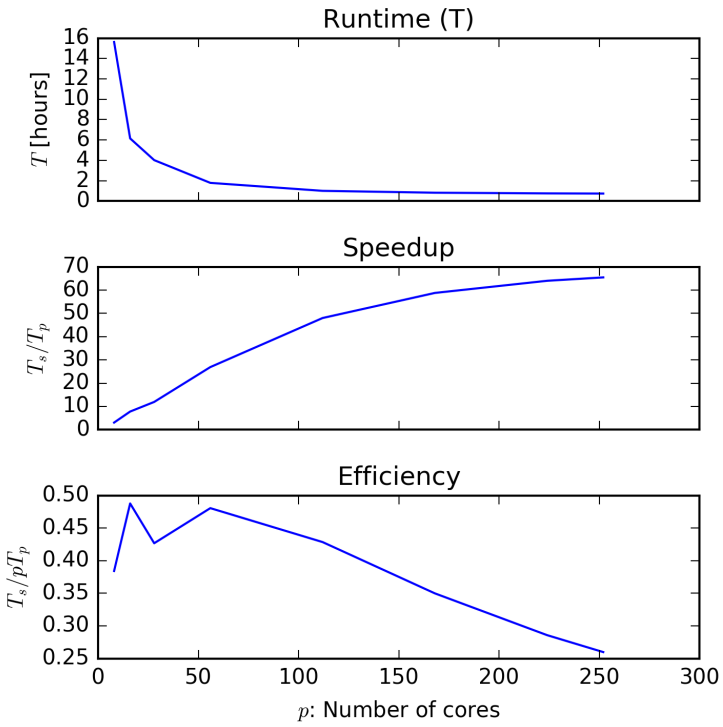

Figure 3.5.1: Runtime, speedup, and efficiency of a sample parallel simulation as functions of number of processes (p).

Since a truly serial runtime could not be acquired, a naive assumption was made such that the serial runtime is $T_s = 48$ hours (the maximum allowed duration per compute session). Even with such an assumption, the speedup can reach up to 70 times the assumed serial speed. Further, the speed does not seem to quite plateau yet at $p = 252$, suggesting again that ERMINE's scaling capacity has not been fully strained.

Finally, the Efficiency is a measure of how each core is efficiently utilized during the parallel computation. Its definition may be

$$\text{Efficiency} = T_s/(pT_p) \tag{3.2}$$

and ranges from 0 (no useful core utilization) to 1 (perfect per-core efficiency). The maximum efficiency is roughly located at $p = 10 - 50$, with a

sharp dip inside the range. Without further monitoring more factors such as real-time memory usage, core load for shared nodes, etc., it is difficult to explain the dip. At $p = 252$, the efficiency reaches 0.25 but has not dropped to 0. This suggests that a higher p can be used before depleting the efficiency.

Overall, Fig. 3.5.1 demonstrates that HPC resources are essential for conducting non-linear electrochemistry simulations in complex microstructure domains. However, it appears this basic scaling test has not fully strained ERMINE's compute performance on Bridges; the test reveals some promise for ERMINE to incorporate a larger domain size or higher model complexity before depleting core efficiency.

3.6 Conclusions

In conclusion, to address microstructural heterogeneties in commercial SOFCs and the associated large variations of local electrochemistry throughout the microstructure, we have developed ERMINE that would fulfill the goal discussed in the first chapter. This goal is, briefly, to construct a numerical model capable of computing morphology-coupled electrochemistry and its distribution throughout the microstructure.

A major highlight of this work is that we have adopted the MOOSE framework, a numerical FE framework designed and tested for high performance computing platforms. We have successfully developed an SOFC-specific application from MOOSE—ERMINE. Using the advantages of MOOSE, ERMINE is capable of simulating ORR within cathode microstructures in a high-throughput, highly parallel fashion. As a result, an individual simulation can converge within a short amount of time.

In addition to ERMINE modeling, every step in the workflow is automated, i.e., without significant user supervision. Thus far, we have shown that our ERMINE model can output results comparable to effective medium theory in a high-throughput fashion. The preliminary results show that a study of substantial size (close to 1500 steady state simulations, each using 16, 32, 64 or more cores) can be done within two weeks. Thus the high-throughput workflow, backed by the hardware and software resources at CMU and NETL, has been proven to contain no elements of infeasibility.

The main scientific contribution of this work, built off of the foundations built up in this chapter, will be detailed in the following chapters—each of those corresponds to a self-contained publishable work.

4

High Performance Computation of Local Electrochemistry in Heterogeneous Microstructures of Solid Oxide Fuel Cells

This chapter is the first self-contained part of the thesis planned for academic journal publication. The following sections correspond to a standard journal structure (e.g., abstract, introduction, methods, results and discussion, conclusions), with an additional section for the supplementary material. Therefore, the chapter can be treated as a stand-alone paper.

4.1 Abstract

A high-throughput, high-performance computational approach is presented to simulate local electrochemistry in three-dimensions over large volumes of solid oxide fuel cell electrodes. Simulations are carried out on 47 three-phase cathodes, whose lateral {vertical} dimensions are 22 {15} times their average

particle size (0.46 µm). The 47 microstructures are spread across four distinct groups having different standard deviations in their particle size and/or local volume fraction distributions. While the average performance simulated compares favorably to two accepted effective medium theory (EMT) models, the largest discrepancy between the locally-resolved simulations and the EMT models arises from the Ohmic transport terms. This is borne out further by considering local electrochemical values, specifically quantifying regions of extremely high current densities or distributions of local activation overpotentials at specific distances from the electrolyte: values often connected with degradation. The impact of particle size and volume fraction distributions on the distribution of performance values (within and between microstructural groups) is highlighted throughout. Results from this study indicate that high-performance simulations in a high-throughput, large-data workflow can elucidate performance characteristics which are not captured by continuum level models utilizing EMT. Understanding of these detailed performance characteristics can be used to develop more durable and reliable electrochemical cells.

4.2 Introduction

Fuel cells are electrochemical devices capable of converting fuel energy directly into electrical energy, with advantages over conventional fossil fuel-based power generation methods (high efficiency, low byproduct emission, etc.) [91, 99]. Solid oxide fuel cells (SOFCs) are excellent candidates for stationary power generation; they have fuel flexibility, high power densities, and the ability to recycle waste heat for combined heat and power applications [99]. Widespread commercialization of SOFCs is limited by performance factors—including durability and reliability—that are related to the microstructure of electrodes and that fundamentally impact the cost of power [2, 17, 23, 31, 54, 88, 91, 96, 101, 109, 126]. Durability refers to a cell's performance over time and reliability refers to the cell-to-cell performance variation. Both are related to degradation. The most challenging degradation mechanisms to overcome in SOFCs (e.g., chromium poisoning, nickel coarsening, interphase reactions, phase decomposition) are correlated to lo-

calized reactions and transport phenomena linked directly to the electrode microstructures [2, 23, 54, 68, 88, 96, 121, 126, 132]. Therefore, quantifying the local microstructure and its influence on local electrochemistry is key to understanding SOFC durability and reliability.

Over the past decade, methods to quantify the electrode microstructure in three-dimensional (3D) space have matured greatly; Ga focused ion beam (Ga-FIB) coupled with scanning electron microscopy (SEM) [16, 22, 23, 37, 51, 54, 57, 58, 61, 63, 87–89, 95, 96, 106, 110, 118, 123, 124] or nanoscale X-ray computed tomography (nano-CT) [13, 18, 25, 26, 38, 40, 60, 69, 81, 95, 109, 110, 117] have become the standard for incorporating 3D microstructural parameters into models of electrochemical performance. They have appropriate resolution to differentiate phases having characteristic lengths scales of $\overline{a}$ = 0.5–1.0 µm over volumes whose edge lengths are L = 10–30 µm. It is believed that volumes with $L^* = L/\ \overline{a}$ = 10–30 accurately capture the local electrochemical performance and—if the microstructure is uniform beyond this length scale—the overall properties of the electrode [43]. Herein, we aim to quantify variations in otherwise identical volumes over the length scale of $L^* \approx 22$. Recently, a Xe-plasma FIB (PFIB) coupled with SEM enabled reconstructions of electrodes over much larger volumes, with in-plane edge lengths over L = 100–200 µm [48, 83]. In the commercial cells investigated [48, 83], variations existed in microstructural parameters well beyond the length scale of $L \approx 15$ µm or $L^* \approx 30$ [26, 48, 83]. These local structural variations contribute to local electrochemical variations [26, 48, 83], which in turn must affect durability and reliability, but in ways that are not well understood. Herein, we compare the variability of simulated performance parameters for a number (14) of large volumes ($L^* \approx 22$) of the commercial cell and compare them to volumes from synthetic homogeneous electrodes [48].

The most widely used methods to quantify electrochemical properties from 3D microstructural data are effective medium theory (EMT) models. EMT models approximate the electrode microstructure as a homogeneous body (often reduced to 1D or 2D) [1] and incorporate effective microstructural properties quantified from 2D or 3D data. Several EMT models have been shown to capture the average performance (such as current-voltage behav-

ior) of complex electrodes with reasonable accuracy [13, 18, 63, 85, 97, 118, 124, 130]. The strengths of EMT models are computational simplicity and relative accuracy for computing average values. For degradation events that may be related to local transport or electrochemical (e.g., current density and overpotential) values away from the mean, EMT is not well suited.

Numerical models that retain spatially resolved 3D microstructural information have also been explored, including finite element (FE) [4, 8, 9, 81, 105], finite volume (FV) [6, 7, 64, 65, 93, 104, 108, 134], and Lattice-Boltzmann [38, 55, 61, 89, 111] methods. Such simulations capture both the average performance values and the local distributions of electrochemical quantities, and are better suited to inform local degradation models. However, spatially resolved numerical models require a significant increase in computational resources; this often limits the scope of the included electrochemical reactions and transport pathways, the volume of individual microstructures, and the overall number of microstructures. Only a few studies have analyzed simulated local performance metrics (e.g., current density and overpotential) from a statistical perspective or across different microstructural types [4, 47, 104]. Bertei et al. [4] recently reported distributions of local current densities within four distinct 3D microstructural subvolumes, providing insight into non-uniformities of local current flow in SOFC electrodes as related to microstructural parameters. The volume of those 4 simulations (one for each type of anode microstructure) had edge lengths on the order of $L^* = 10$–16, which are on the larger end of any volumes reported previously using such 3D simulations. We have developed a high-performance FE code [47] that enables a significant increase in the volume of individual microstructures simulated, allows a large number of volumes to be simulated simultaneously in a reasonable time-frame, and includes several different types of electrochemical reaction/transport paths. This is particularly important relative to commercial cathodes that have significant standard deviations in both particle sizes and local volume fractions [26, 48, 83], and have both two phase boundary (2PB) and three phase boundary (TPB, or 3PB) electrochemical reaction-and-transport paths [30].

Here, we present a high-performance computational (HPC) workflow capable of processing PFIB-scale datasets of 3D cathode microstructures and

simulating morphology-resolved, local electrochemical values at considerable length scales ($L^* \approx 22$) in a high-throughput fashion (47 such volumes). Further, the computations consider both 2PB and TPB electrochemical pathways. Parallel simulations were implemented using the open-source MOOSE framework [33] and carried out—each using 256 cores—on two supercomputers: Joule (National Energy Technology Laboratory, Morgantown, WV) and Bridges [98] (Pittsburgh Supercomputing Center, Pittsburgh, PA). The 47 microstructures are spread across four distinct groups having different standard deviations in their particle size and/or local volume fraction distributions. Both commercial SOFC and synthetic datasets (described elsewhere [48]) are included. We investigated both intra-group and inter-group distributions of electrochemical quantities, especially focusing on local electrochemical property values. These HPC simulations produced significant amounts of data, allowing a data-driven statistical approach to understanding SOFC durability and reliability.

4.3 Methods

A computational workflow was developed to mesh and simulate reconstructed SOFC cathode microstructures in a high-throughput fashion. An experimentally captured commercial SOFC cathode microstructure (named COM-0.48) and three synthetically generated microstructures (named SYN-0.34, SYN-0.40, and SYN-0.50, respectively) were used for this work. The acquisition and the properties of these microstructures were detailed elsewhere [48, 83]. The properties relevant to this work are tabulated in Table 4.3.1.

Table 4.3.1: Summary of the microstructures used for electrochemical modeling

Name	Origin	$\sigma_a / \ \overline{a}$	$\overline{\rho}_{\mathrm{TPB}}$ [$\mu\mathrm{m}^{-2}$]	$\overline{\tau}_{\mathrm{YSZ}}$	Subvolume size [µm]	# of subvolumes
SYN-0.34	Synthetic	0.34	7.8	1.27	$10 \times 10 \times 7$	13 (15)
SYN-0.40	Synthetic	0.40	6.3	1.30	$10 \times 10 \times 7$	12 (15)
COM-0.48	PFIB	0.48	4.8	1.38	$10 \times 10 \times 7$	14 (15)
SYN-0.50	Synthetic	0.50	4.2	1.31	$10 \times 10 \times 7$	8 (9)

The microstructure names include letters and numbers. The letters indicate the type of microstructure; SYN for synthetically generated microstruc-

tures [48] and COM for a commercial cathode (supplied by Materials and Systems Research, Inc., Salt Lake City, UT) characterized using PFIB [48]. The numbers in the names indicate the mean-normalized standard deviation of the particle size ($\sigma_a/\ \overline{a}$).

The mean particle size ($\overline{a}$) of the three synthetic microstructures were scaled (by scaling voxel size) to match that of the commercial cathode (0.46 µm). These mean values are based on number-weighted distributions and their measurement details were reported in [48]. $\sigma_a/\ \overline{a}$ is the primary microstructural variable that differs across the synthetic microstructures [48], which affects other microstructural parameters, including the mean triple phase boundary (TPB) density ($\overline{\rho}_{\mathrm{TPB}}$) and the mean yttria-stabilized zirconia (YSZ) tortuosity factor ($\overline{\tau}_{\mathrm{YSZ}}$). The TPB density was measured by summing the mesh element perimeters at the intersection of three phases in a meshed three-phase microstructure. The tortuosity factor is the square of the geometric tortuosity [48], which is based on geometric distances. The local volume fraction for each synthetic microstructure is consistent and quickly converges with increasing length scale, but the local volume fraction of COM-0.48 was reported to vary more significantly [26, 48]. Table 4.6.1 (in Supplementary Material, Sec. 4.6) includes microstructural parameters quantified for each subvolume that resulted in a converged simulation. The importance of $\sigma_a/\ \overline{a}$, $\overline{\rho}_{\mathrm{TPB}}$, and $\overline{\tau}_{\mathrm{YSZ}}$ to the electrochemical performance is discussed in the results section.

After scaling, each reconstructed microstructure was divided into multiple subvolumes of the same size—$10\times10\times7$ µm^3—resulting in each volume having the dimensions of $L^* = 21.7\times21.7\times15.2$. A 3 µm thick electrolyte layer was appended to each subvolume, making all simulation domains $10\times10\times10$ µm^3. These domains were subjected to the workflow that converts the TPB lines into volumes (described as a fourth phase) and then meshes the volumetric phases. Figure 4.3.1 visualizes one of the COM-0.48 subvolumes, where (a) represents the component layers, (b) shows the meshed morphology of the overall microstructure in the whole computational domain, and (c) shows a higher resolution rendering of a small region of the cathode to emphasize the meshed TPB elements (the red phase). In Figure 4.3.1b and 4.3.1c, the pores (gas permeable phase) are transparent, the ion-conducting

phase (YSZ) is green, and the electron conducting phase (LSM) is blue. A total of 54 subvolumes, as indicated by the numbers in the parentheses in Table 4.3.1, were subjected to the workflow, with 47 yielding numerical convergence at the simulation stage (87 % yield rate).

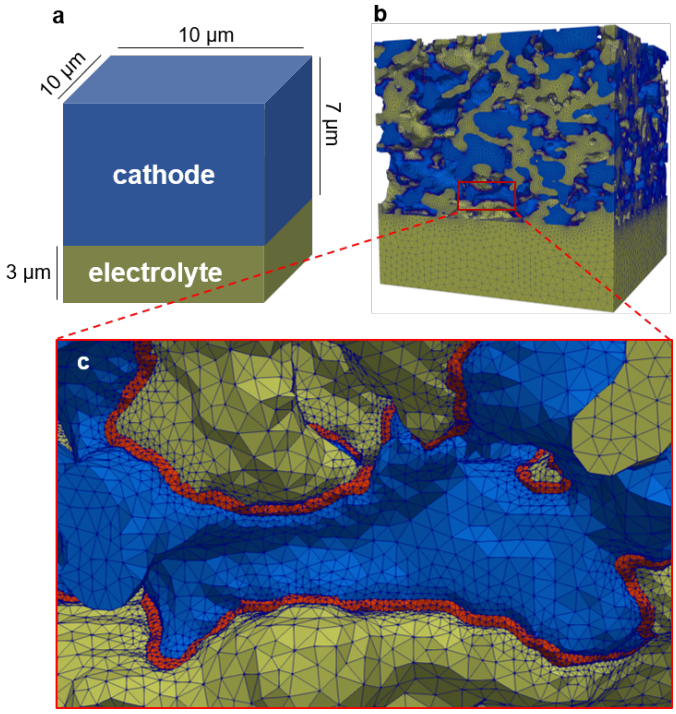

Figure 4.3.1: Visualization of a meshed microstructure subvolume. This subvolume belongs to COM-0.48. (a) Simplified representation of the component layers with length scales. (b) Rendering of the meshed suvolume with unstructured, tetrahedral elements. The number of total mesh elements is 29.4 millions. (c) Magnified region of (b) showing TPB mesh elements. The pores are transparent. The blue phase is lanthanum strontium manganite (LSM). The green phase is yttria-stabilized zirconia (YSZ). The red phase is TPB.

The electrochemical model (herein named ERMINE, for Electrochemical Reactions in MIcrostructural NEtworks) is a reaction-and-transport model that simulates two oxygen reduction reaction (ORR) pathways in a three-phase cathode microstructure. Implementation-wise, the simulation operates on four-phase microstructural meshes, with the fourth phase being the volumetric TPB mesh elements, which act as volumetric source/sink terms for

the reaction species. Two ORR pathways are included in the current version of ERMINE, as listed below.

- TPB pathway: oxygen gas and electrons transport from the top of the cathode through the pores and LSM, respectively, react to produce oxygen ions within the TPB elements, and oxygen ions transport through YSZ to the bottom of the electrolyte.

- MIEC (mixed ionic-electronic conductivity) pathway: oxygen gas and electrons transport from the top of the cathode through the pores and LSM, respectively, oxygen in the pores react with electrons at pore/LSM interfaces to produce oxygen ions in LSM (i.e., surface exchange), oxygen ions transport through LSM and transfer to YSZ at an LSM/YSZ interface, and the oxygen ions transport through YSZ to the bottom of the electrode.

In the pore/LSM/YSZ cathode, the ORR has fast kinetics for the TPB pathway and much slower kinetics for the MIEC pathway. Though all simulations carried out incorporated both pathways, using the material parameters given in Table 4.6.2, the TPB pathway typically accounts for more than 99 % of the overall ionic current.

ERMINE is an application developed within the MOOSE framework, an open-source finite element environment designed for massively parallel multiphysics simulations [33]. Two supercomputers were used for simulations: Joule (National Energy Technology Laboratory, Morgantown, WV) and Bridges [98] (Pittsburgh Supercomputing Center, Pittsburgh, PA). Their hardware specifications can be found at `https://hpc.netl.doe.gov` and `https://www.psc.edu/bridges`. Each simulation (subvolume) took typically 30 minutes to 2 hours of runtime using 256 state-of-the-art cores. ERMINE outputs scalar fields of simulated electrochemical properties (e.g., the potential in YSZ, the oxygen gas partial pressure in pores) evaluated at the mesh element nodes. Vector quantities such as the local current densities are calculated in post-simulation processing using the open-source scientific visualization software Paraview (Kitware Inc., Clifton Park, NY and Sandia National Laboratories, Albuquerque, NM). Effective performance metrics

can also be calculated from the electrochemical fields. Specifically, the effective current density is calculated by averaging the local current densities exiting the bottom of the electrolyte.

The ERMINE outputs were compared with two different EMT models: the TFV model [18, 115] and the DREAM SOFC model [85, 100]. Volume fractions, mean particle sizes, TPB densities, and tortuosity factors were taken as input into TFV and DREAM SOFC to produce effective performance metrics. The model parameters used for TFV, along with the model implementation details, were described in [48]. The DREAM SOFC model was used as described in [85], but with the same parameters as those used by ERMINE (Table 4.6.2). For DREAM SOFC, the Butler-Volmer expression was derived considering $\frac{1}{2}\,O_2 + 2\,e^- \longrightarrow O^{2-}$ [85]: only 2 electrons were considered in the reaction. However, the formulation of the Butler-Volmer expression for ERMINE considers a reaction similar to $O_2 + 4\,e^- \longrightarrow 2\,O^{2-}$: 4 electrons were considered in the reaction. The current DREAM SOFC simulations involved only the cathode half-cell, as described in [86], to correspond to the cathode half-cell setting of ERMINE. Both TFV and DREAM SOFC only consider the TPB pathway as the mechanism of ORR. While ERMINE simulates both TPB and MIEC pathways, the MIEC pathway is negligible. Thus, all three models are mechanistically similar to each other.

4.4 Results and Discussion

4.4.1 ERMINE simulations and microstructural heterogeneities

Table 4.3.1 shows that $\overline{\rho}_{\mathrm{TPB}}$ decreases as $\sigma_a/\ \overline{a}$ increases for a fixed average particle size (0.46 µm); this is supported by observations in [62]. The relationship is essentially linear, as illustrated in Figure 4.4.1a. The values of $\overline{\rho}_{\mathrm{TPB}}$ and $\sigma_a/\ \overline{a}$ from the COM-0.48 cathode agree well with the linear relationship determined from the synthetic cathodes. The effective current densities (j) computed using ERMINE for all 47 subvolumes are plotted across a range of overpotentials (η) in Figure 4.4.1b. For the synthetic cathodes, the current density at any specific overpotential increases with increasing $\overline{\rho}_{\mathrm{TPB}}$ (decreasing $\sigma_a/\ \overline{a}$). However, the η-j curves of COM-

0.48 do not lie between the curves of SYN-0.40 and SYN-0.50, even though the average TPB density of COM-0.48 is between that of SYN-0.40 and SYN-0.50. The COM-0.48 subvolumes generally exhibit lower j values than SYN-0.50, even though they have higher TPB densities (clearly evident in the inset of Figure 4.4.1b). Note that based on Figure 4.4.1b, the computed performance indicates primarily activation behavior/losses with some Ohmic contribution.

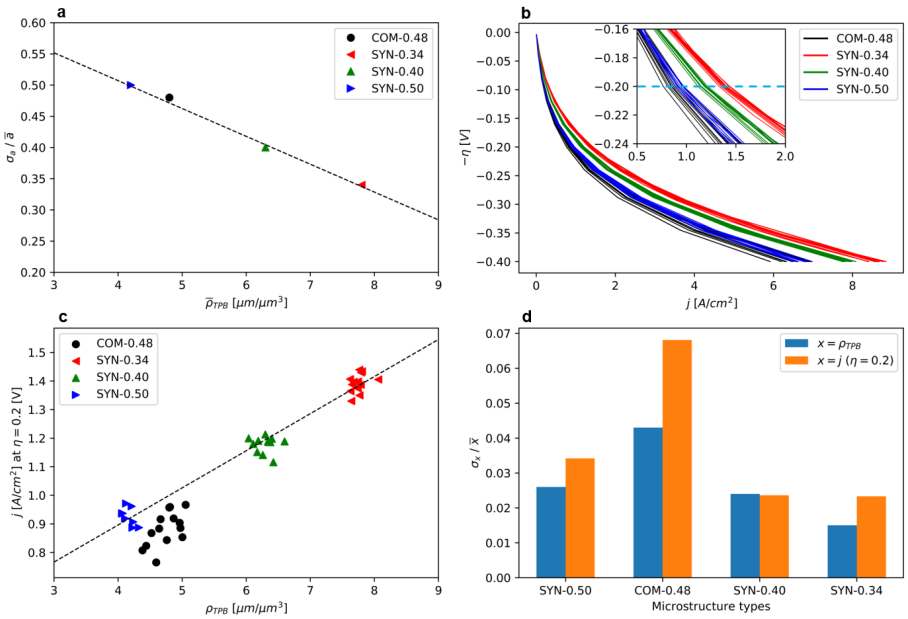

Figure 4.4.1: Comparison of the microstructure types based on effective performance output by ERMINE. (a) shows a near-linear relationship between $\sigma_a / \bar{a}$ and $\bar{\rho}_{\mathrm{TPB}}$ for all of the microstructures. The dashed line is the linear fit of the data points. (b) Effective current densities (j) of the 47 subvolumes across a range of overpotentials (η). Note that η is applied across the cathode and the electrolyte layers. The inset is a magnified region focusing on 0.2 V of overpotential, which the dashed blue line indicates. (c) Values of j at $\eta = 0.2$ V from (b) plotted against subvolume-specific TPB densities (ρ_{TPB}). The dashed line is a linear fit of the synthetic microstructures, excluding COM-0.48. (d) Barplot of mean-normalized standard deviations of x, where x represents either ρ_{TPB} or j (at $\eta = 0.2$).

The values of j at $\eta = 0.2$ V are plotted against subvolume-specific TPB densities (ρ_{TPB}) in Figure 4.4.1c. The dashed line represents the linear fit

to the synthetic cathodes data, indicating that j (of the synthetic cathodes) scales almost linearly with ρ_{TPB} (and therefore $\sigma_a/\ \overline{a}$ for a fixed particle size). However, these values do vary around the average, and the mean-normalized standard deviations of ρ_{TPB} and j (at $\eta = 0.2$) are plotted in Figure 4.4.1d. For the synthetic microstructures, the distribution width (or the standard deviation) of j generally corresponds to that of ρ_{TPB}, and the mean-normalized standard deviation of both increases with increasing $\sigma_a/\ \overline{a}$. The values of j (at $\eta = 0.2$) for the COM-0.48 subvolumes in Figure 4.4.1c are considerably below the linear fit from the synthetic data, indicating that the COM-0.48 subvolumes are underperforming relative to their ρ_{TPB} values. The COM-0.48 subvolumes also exhibit a wider distribution of ρ_{TPB} and j relative to their mean values (Figure 4.4.1d), and the distribution width of j is a bit wider, relative to the distribution width of ρ_{TPB}, than is observed in the synthetic cathodes.

The results presented in Table 4.3.1 and Figure 4.4.1 indicate that the primary microstructural effect of a broader particle size distribution ($\sigma_a/\ \overline{a}$), at a given particle size, is a linear variation in ρ_{TPB} and a linear variation in j (at $\eta = 0.2$). The mean-normalized standard deviations of these values also increase with $\sigma_a/\ \overline{a}$, from 1.5 to 2.5 % for ρ_{TPB} and from 2 to 3.5 % for j, even though each group is built from statistically similar microstructural targets and have $L^* \approx 22$. Further, the properties of the commercial cathode indicate that they contain another level of microstructural heterogeneity not present in the synthetics electrodes. While this heterogeneity did not impact the average value of ρ_{TPB} versus $\sigma_a/\ \overline{a}$, it leads to an underperformance of j (at $\eta = 0.2$), and a wider distribution in mean-normalized standard deviation for its $\sigma_a/\ \overline{a}$: 4% for ρ_{TPB} and 6.5 % for j. This agrees with the original report [48], which demonstrated that the commercial cathode had significant local variations of volume fraction and TPB density over the mesoscale. The electrochemical simulations run in ERMINE quantify the impact of these microstructural variations; the simulations indicate that the impact is not exclusively tied to the local ρ_{TPB} values, but also to other local microstructural features internal to subvolumes of $L^* \approx 22$.

4.4.2 Comparison of ERMINE and EMT models

In Table 4.3.1, there is a small but quantifiable difference in the mean tortuoisty factor of the YSZ phase ($\overline{\tau}_{\mathrm{YSZ}}$), a value that increases in a similar fashion to the variability in mean-normalized standard deviation of ρ_{TPB} and j (at $\eta = 0.2$) discussed in Section 4.4.1. The YSZ tortuosity factor represents an effective transport path distance for ionic transport in YSZ and is typically incorporated into EMT models. Thus, comparison to EMT models will be informative in estimating the impact of ionic transport versus TPB reactivity.

As shown in Figure 4.4.2, the η_c-j performance curves from ERMINE are compared to the two EMT models. Note that η_c is the overpotential across only the cathode layer. The η_c-j performance curves of TFV are linear, while the curves of ERMINE and DREAM SOFC are combinations of logarithmic (activation or Tafel) and linear (Ohmic) parts. Relative to the other two models, the TFV model overpredicts the performance at low overpotentials and underpredicts at high overpotentials, with a crossover near $\eta_c \approx 0.15$ V. ERMINE and DREAM SOFC are in reasonable qualitative agreement across the entire overpotential range, which verifies that ERMINE and DREAM SOFC are modeling the reaction/transport of the TPB pathway in a comparable way. Quantitatively, however, the ERMINE curves have consistently lower j values at any given η_c than the DREAM SOFC curves, which we explore more deeply below.

In general, the three models are quite similar in values near $\eta_c \approx 0.15$ V, which supports the utility of EMT models to capturing average performance at typical cathodic overpotentials [13, 18, 63, 85, 97, 118, 124, 130]. Visually, the spread among the performance curves for the synthetic microstructutres is narrow compared to the commercial cathode. Based on the assumption that the η_c-j curves of ERMINE and DREAM SOFC consist of activation and Ohmic contributions, more fundamental performance descriptors—the effective exchange current density (j_0), which is sensitive to TPB density [11], and the effective Ohmic resistance (R_{ohm}), which is sensitive to YSZ tortuosity [125]—were extracted by fitting them with a nonlinear function

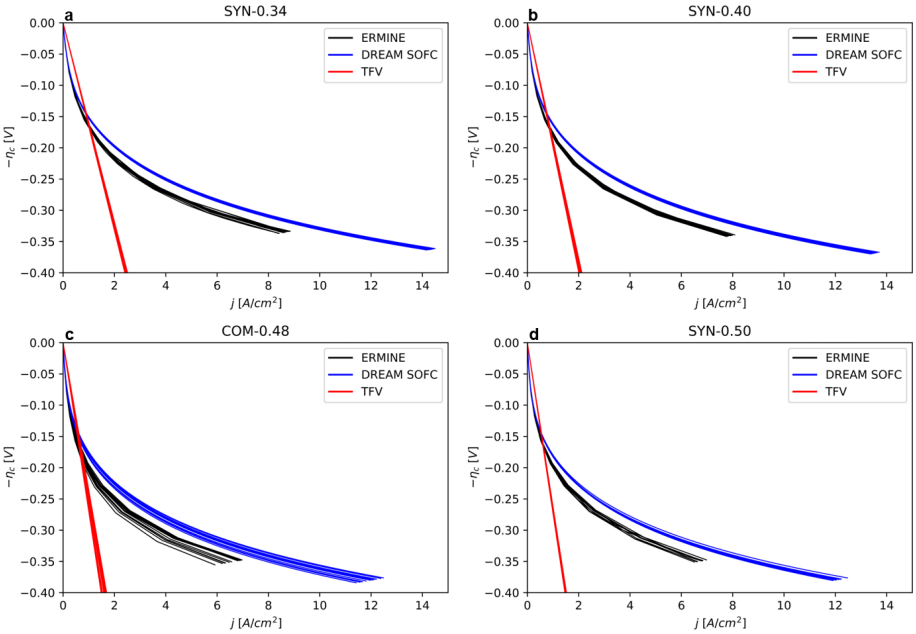

Figure 4.4.2: Effective performance outputs from ERMINE, DREAM SOFC, and TFV for all subvolumes grouped by the microstructure type. η_c is the model overpotential across the cathode layer, and j is the effective current density. Subfigure title indicates the microstructure type.

consisting of a Tafel term and an Ohmic term. The Tafel term describes the activation overpotential as:

$$\eta_{act} = \frac{RT}{\alpha z F}[\ln(j) - \ln(j_0)], \tag{4.1}$$

where R is the gas constant, T is the temperature, α is the symmetry factor (α=0.5), and F is the Faraday constant. The Ohmic term describes the Ohmic overpotential as:

$$\eta_{ohm} = jR_{ohm}. \tag{4.2}$$

The nonlinear function, which expresses the total overpotential (over cathode), is therefore:

$$\eta_c = \eta_{act} + \eta_{ohm} = \frac{RT}{\alpha z F}[\ln(j) - \ln(j_0)] + jR_{ohm}. \tag{4.3}$$

Equation 4.3 was used to fit the η_c-j curves from the ERMINE and DREAM SOFC models. Figure 4.6.1 illustrates the η_c-j data and the fitted curves for one subvolume of each microstructure type. Very good fits were obtained for all subvolumes for both models.

The effective j_0 values extracted from the DREAM SOFC and ERMINE η_c-j curves are plotted versus ρ_{TPB} in Figures 4.4.3a and 4.4.3b, respectively. The EMT model directly links activation current with ρ_{TPB}, and a nearly linear trend is observed in Figure 4.4.3a between j_0 and ρ_{TPB}. The COM-0.48 data agrees well with the values for the synthetics, with the j_0 values being slightly lower than expected for their ρ_{TPB}. The values of j_0 from ERMINE (Figure 4.4.3b) are uniformly lower than those from DREAM SOFC (Figure 4.4.3a), though the local TPB reaction rates were identical in both models. This indicates that the details of transport from local TPBs, as modeled by ERMINE, effectively reduces the exchange current compared to DREAM SOFC. Also, because the slope of the line fitted to the synthetic data in Figure 4.4.3b (0.0033) is lower than that of Figure 4.4.3a (0.0045), this effect is more significant at higher ρ_{TPB}. Nevertheless, the data in Figure 4.4.3b approximate a linear trend, but with significantly higher scatter of j_0 values at a given ρ_{TPB} (vertical scatter) than the data from DREAM SOFC (Figure 4.4.3a). This also indicates that details of the local transport from TPBs effectively increase the spread in the values of j_0. Again, the COM-0.48 values are in similar agreement with the synthetic values, but they are a little more depressed from the line for ERMINE than for DREAM SOFC: some values for COM-0.48 are lower than the lowest value for SYN-0.50 in the ERMINE data, but not in the DREAM SOFC data.

The values of R_{ohm} extracted from the DREAM SOFC and ERMINE η_c-j curves are plotted versus $\tau_{\mathrm{YSZ}}/\theta_{\mathrm{YSZ}}$ (YSZ tortuosity factor divided by YSZ volume fraction) in Figures 4.4.3c and 4.4.3d, respectively. In DREAM SOFC, the effective YSZ ionic conductivity ($\gamma_{\mathrm{YSZ,e}}$) is estimated using a Bruggeman type model:

$$\gamma_{\mathrm{YSZ,e}} = \gamma_{\mathrm{YSZ}} \frac{\theta_{\mathrm{YSZ}}}{\tau_{\mathrm{YSZ}}}, \tag{4.4}$$

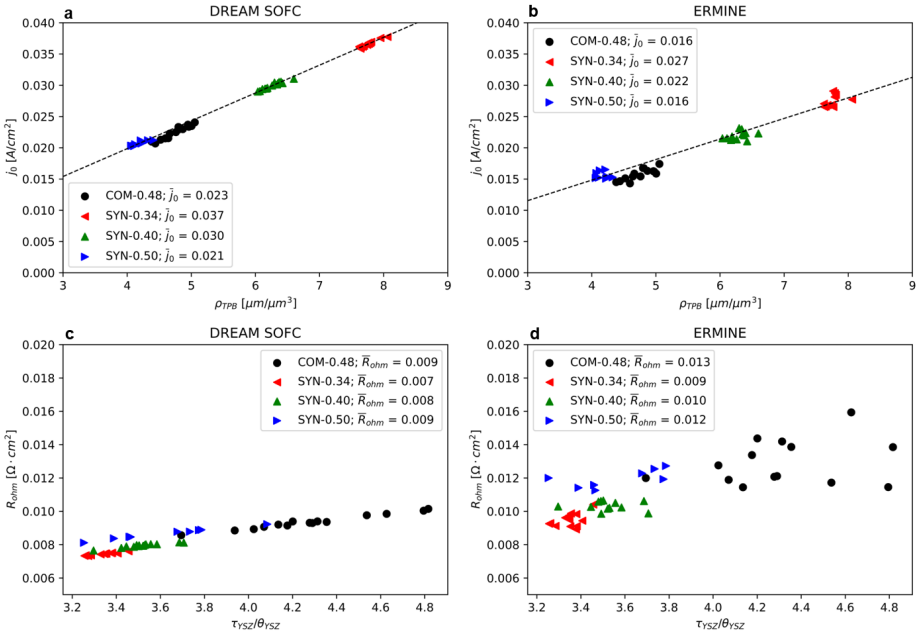

Figure 4.4.3: Exchange current densities (j_0) and Ohmic resistances (R_{ohm}) plotted against ρ_{TPB} and $\theta_{\mathrm{YSZ}}/\tau_{\mathrm{YSZ}}$ (YSZ volume fraction divided by YSZ tortuosity factor) respectively for all subvolumes. The legend in each subfigure indicates the microstructure type and the mean value of j_0 or R_{ohm}. Subfigure titles indicate the model name. The dashed lines are linear fits applied to the synthetic microstructures, excluding COM-0.48.

where γ_{YSZ} is the YSZ conductivity value. Since resistance is inversely proportional to conductivity ($R \propto 1/\gamma$), the linear relationship of $\gamma_{\mathrm{YSZ,e}}$ with respect to $\theta_{\mathrm{YSZ}}/\tau_{\mathrm{YSZ}}$ corresponds to an inverse relationship of R_{ohm} with respect to $\theta_{\mathrm{YSZ}}/\tau_{\mathrm{YSZ}}$; equivalently, R_{ohm} is linear with respect to $\tau_{\mathrm{YSZ}}/\theta_{\mathrm{YSZ}}$. A nearly linear relationship is observed in Figure 4.4.3c, as expected from DREAM SOFC, with a relatively shallow slope. Considering the synthetic data only, each type of microstructure exhibits a linear relationship between R_{ohm} and $\tau_{\mathrm{YSZ}}/\theta_{\mathrm{YSZ}}$ with a shallow slope. As the $\sigma_a/\ \bar{a}$ increases, the R_{ohm} values (lines) increase very slightly, the average $\tau_{\mathrm{YSZ}}/\theta_{\mathrm{YSZ}}$ values increase, and the spread of $\tau_{\mathrm{YSZ}}/\theta_{\mathrm{YSZ}}$ values increases significantly. The COM-0.48 data is significant in that the average value of $\tau_{\mathrm{YSZ}}/\theta_{\mathrm{YSZ}}$ is considerably higher than for all of the synthetics, and the spread is similar to the SYN-0.50 data. This indicates that the increased heterogeneity in the COM-0.48

microstructure impacts the tortuosity significantly (as opposed to ρ_{TPB}), which also increases R_{ohm} significantly.

Figure 4.4.3d shows that the values of R_{ohm} from ERMINE are uniformly higher than those from DREAM SOFC (Figure 4.4.3c). The linear correlation is less obvious, if applicable, because there is considerably more variation in the data around an expected shallow slope. As $\sigma_a / \ \overline{a}$ increases for the synthetic data sets, (the average of) R_{ohm} also increases more significantly in the ERMINE data than in the DREAM SOFC data, though the scatter around the average is similar for all (again highlighting a near zero slope for each). The values of R_{ohm} from ERMINE for the COM-0.48 data are even more scattered and distributed towards higher values than expected from the synthetics. This indicates that the local volume fraction heterogeneity manifests itself strongly in the local ionic transport and impacts the effective local Ohmic resistance.

Overall, Figure 4.4.3 demonstrates a distinctive difference between ERMINE and DREAM SOFC outputs. While the EMT approximations of DREAM SOFC are reasonable and generate qualitative agreements between the two models, the full-scale locally resolved ERMINE simulations deviate from the EMT model in a manner that suggests the differences arise in the treatment of local ionic transport. ERMINE indicates that the local ionic transport paths suppress the effective exchange current from the ensemble of TPBs more than accounted for in DREAM SOFC, while the linear relationship between j_0 and ρ_{TPB} is preserved. ERMINE also indicates that the local ionic transport paths increase the effective Ohmic resistance of the cathode more than accounted for in DREAM SOFC. Because the correlation of R_{ohm} with $\tau_{\mathrm{YSZ}}/\theta_{\mathrm{YSZ}}$ is shallow in the DREAM SOFC data, the significantly increased scatter in R_{ohm} found in the ERMINE data suggests that the difference between ERMINE and DREAM SOFC is primarily related to the treatment of the local ionic transport.

4.4.3 Activation overpotential distribution and binning analysis

Thus far, *effective* electrochemical quantities based on subvolume ensembles have been analyzed. Here, the local overpotential at active TPBs (η_{TPB}) is examined, which is expected to influence degradation mechanisms (such as chromium poisoning [68, 93, 121]). The 3D distribution of local activation overpotential at active TPBs (η_{TPB}) of a COM-0.48 subvolume is shown in Figure 4.4.4a, for which the global overpotential (η) was 0.2 V across the domain. In Figure 4.4.4a, the TPB elements are rendered and the value of η_{TPB} is denoted by the color. It can be seen that the activation overpotential varies along the vertical (Z) axis, with high values (approaching the global overpotential) towards the bottom (Z = 0 µm) and low values (0.10 V) near the top (Z = 7 µm). At any given TPB location, the activation overpotential and the Ohmic overpotential, as defined in this study, must sum up to the global overpotential (0.2 V). Thus, as the Ohmic overpotential increases, the activation overpotential decreases. In other words, TPB elements with activation overpotentials near 0.2 V {0.1 V} require little {significant} Ohmic overpotential to drive the generated current from TPBs, through the YSZ, to the electrolyte. The overpotentials are therefore a function of the specific local current pathways in YSZ and the local current densities in those pathways. Similar distributions of η_{TPB} are observed in all subvolumes, though lateral and vertical variations differ within and between microstructural types.

To better visualize and quantify the variations, the data shown in Figure 4.4.4a were binned into $1 \times 1 \times 1$ µm^3 volumes, and the median value in each bin was determined. Figure 4.4.4b-d visualizes the lateral (X-Y plane) variation of the binned η_{TPB} values extracted from Figure 4.4.4a, with (b), (c), and (d) corresponding to a Z-range of 0–1, 1–2, and 2–3 µm, respectively. Significant variations of η_{TPB} are observed, with regions of relatively low values being adjacent to regions of relatively high values, both laterally in an image and across images in the same X-Y location. Such variations can occur because of significant differences in the local transport path (the

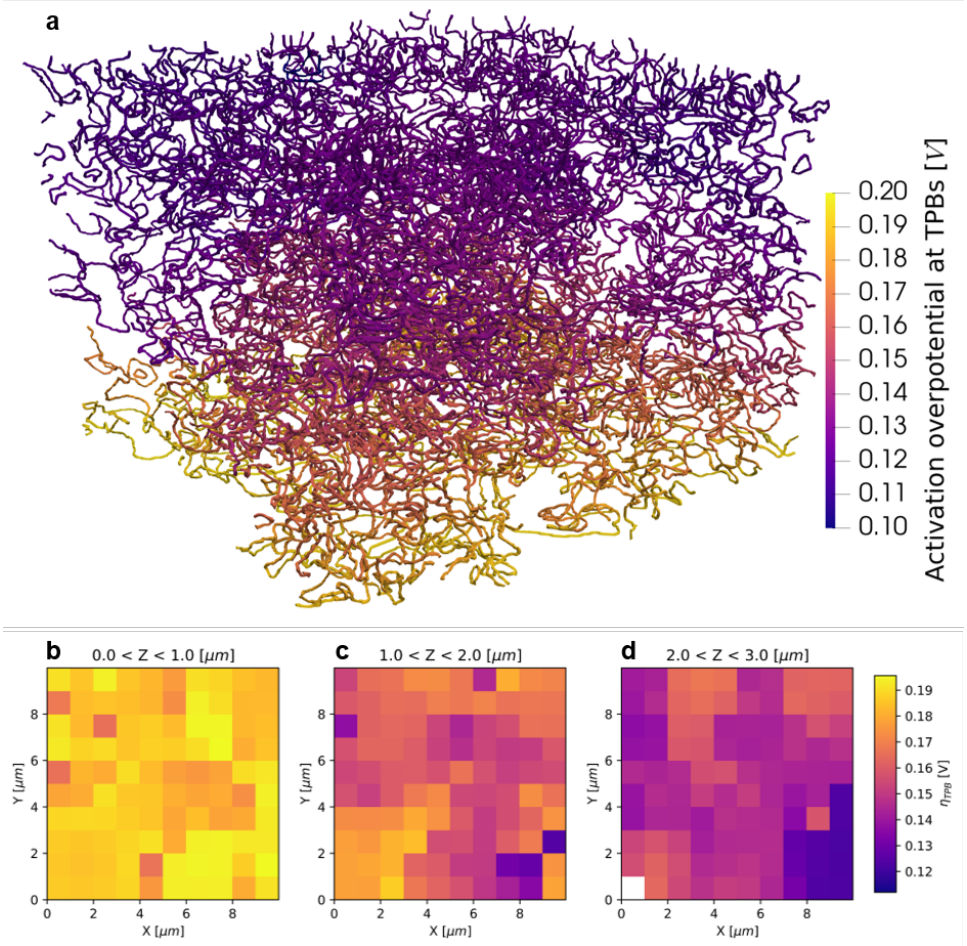

Figure 4.4.4: 3D distribution of local activation overpotential at TPBs (η_{TPB}) of a COM-0.48 subvolume at $\eta = 0.2$ V. (a) Original data representing η_{TPB} at the TPB elements. Only the TPB elements are rendered. (b-d) Binned medians of η_{TPB} according to $1 \times 1 \times 1$ $\mu\mathrm{m}^3$ bins. Subfigure title indicates bin location along the vertical (Z) axis. Z = 0 corresponds to the cathode/electrolyte interface. Only up to three bin widths along Z are shown. Lack of color (white) indicates absence of TPBs.

local tortuosity from the TPB to the electrolyte), the local value of the ionic current to which an element contributes (the local ρ_{TPB} and/or local constrictions in ionic current paths), or combinations of those. The variations observed within a specific Z-layer (≈ 10 % at a given Z value) and between adjacent Z-layers (regions of TPBs in the second layer are more active than regions of TPBs in the first layer, etc.) are both significant.

The binning process described above was applied to all 47 subvolumes, resulting in 32900 ($47 \times 10 \times 10 \times 7$) binned median values of η_{TPB} from all subvolumes. These values were further grouped by microstructural type and Z location, and new median values were computed (e.g., the median values from COM-0.48 at Z=0–1 µm are condensed to a single median value). The new median values are plotted against the distance to the electrolyte (Z), as shown in Figure 4.4.5a. A similar analysis was performed based on the DREAM SOFC data, as shown in Figure 4.4.5b. For plotting purposes, the midpoints of the bin widths are used to represent Z-ranges. The decrease of η_{TPB} with increasing Z resembles an exponential curve. As Z approaches 0, η_{TPB} reaches the maximum value, indicating the TPBs at the electrolyte interface contribute the most to the overall performance. As Z approaches 7, η_{TPB} does not drop below 0.10 V, indicating that the TPB reaction (activation) 7 µm away from the electrolyte still has a higher contribution to the global overpotential than the Ohmic overpotential does. This is likely due to the relatively thin cathode and electrolyte thicknesses (7 and 3 µm, respectively).

Two major differences between the model outputs can be observed in Figure 4.4.5. First, ERMINE simulations result in overall lower values of η_{TPB}, particularly at $Z > 0$, as compared to DREAM SOFC. Second, the COM-0.48 curve has a functionally different form relative to the synthetics in the ERMINE simulations, while it is similar to the synthetics in DREAM SOFC.

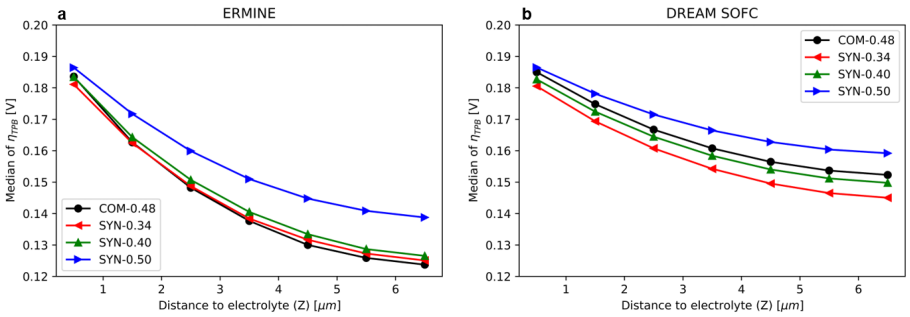

Figure 4.4.5: Local activation overpotentials at TPBs (η_{TPB}) versus distance to the electrolyte (Z) for all subvolumes at global overpotential of 0.2 V. η_{TPB} was computed from (a) ERMINE and (b) DREAM SOFC, as indicated by the subfigure title. The markers' X coordinates are at the midpoints of the bin widths along Z.

Although ERMINE simulations result in overall lower η_{TPB}, there is little difference in η_{TPB} between the two models at $Z \approx 0$, likely because the local ionic current generated at TPBs near $Z = 0$ does not travel any significant distance through the cathode. The value of η_{TPB} near the electrolyte is primarily determined by the current density through the uniform electrolyte, which is dominated by the average ρ_{TPB}. As the current density through the electrolyte increases with ρ_{TPB}, the Ohmic {activation} overpotential increases {decreases}. For the DREAM SOFC data, this trend is observed at all Z values: the value of η_{TPB} from lowest to highest corresponds to SYN-0.34, SYN-0.40, COM-048, and SYN-0.50, which corresponds to the order of ρ_{TPB}. At $Z > 0$ for ERMINE, geometric details of the ionic transport pathways through the microstructure from TPBs and the associated current density magnitudes in the pathways combine to effectively suppress {raise} the local activation {Ohmic} overpotentials as compared to DREAM SOFC.

In Figure 4.4.5a, the local ionic transport (Ohmic overpotential) for COM-0.48 begins in the mid-range of the four groups at $Z \approx 0$, but gradually becomes worse than the others (steeper descent), and is the worst beyond $Z = 2$. The behavior of the COM-0.48 data in DREAM SOFC shown in Figure 4.4.5b does not indicate such a steep decrease, though the values seem suppressed from the similar SYN-0.50 data. The unique steep decrease of the COM-0.48 curve in ERMINE suggests that the COM-0.48 microstructure and performances are fundamentally different from the synthetic electrodes;

its distinctive level of heterogeneity results in worse local ionic transport, a likely cause for COM-0.48's significantly depressed effective current densities than expected for its TPB density values (Figure 4.4.1c).

The activation (and Ohmic) overpotential is a function of the specific local current pathways in YSZ and the local current densities in those pathways. Factors related to local current pathways include the tortuosity factor, and factors related to local current density include TPB density and pathway constrictions (discussed in Section 4.4.4). The impact of changing tortuosity factors (by a factor of 3) and TPB densities (by a factor of 1.6) in DREAM SOFC on η_{TPB} and j are quantified in Figure 4.6.2. It can be seen that both τ_{YSZ} and ρ_{TPB} significantly impact the performance metrics (η_{TPB} and j). Figure 4.6.2a and c indicate that an increase in τ_{YSZ} effectively suppresses the values of η_{TPB} and j. Therefore, significantly increasing the tortuosity factor (or τ/θ) in DREAM SOFC brings its output closer to that of ERMINE (in terms of η_{TPB} and j). However, the output does not match perfectly: attempting to match the η_{TPB}-Z curves (Figure 4.6.2a) requires $\tau/\theta = 10$–12, which overly suppresses j in the η_c-j curves. Similarly, attempting to match the η_c-j curves requires $\tau/\theta = 8$, which results in overly high values of η_{TPB} in the η_{TPB}-Z curves. It should be noted that, $\tau/\theta = 8$–12 corresponds to an increase in the YSZ tortuosity factor by 2 to 3, which is much too large to be an error in the measurement or method to describe the effective tortuosity, and indicates that *local* tortuosity from TPBs is important.

Figure 4.6.2b and d indicate that an increase in ρ_{TPB} effectively suppresses η_{TPB}, similar to above, but it also raises j. This indicates that an increased current density (from increased TPB density) indeed suppresses η_{TPB}, but not at the expense of overall current density that occurs on increasing τ_{YSZ}. Since the average current density is strongly connected to the average ρ_{TPB}, an increased average current density is not likely the difference between ERMINE and DREAM SOFC. However, increased local current densities, e.g., high current densities at constrictions (see Section 4.4.4), may cause a suppression in η_{TPB} without an increase in the average j.

This analysis suggests that the difference between ERMINE and DREAM SOFC may be accounted for by a combination of (1) high local tortuosity from TPB sites relative to the average/effective tortuosity, and (2) in-

creased local current density, such as in constrictions. It is interesting to note that modifying the effective tortuosity value in DREAM SOFC can better capture the output generated by ERMINE without needing a priori geometrical arguments. This manual match indicates that improved EMT models can be generated using microstructurally resolved 3D simulations, such as ERMINE, that directly simulate the microstructural effects without assumptions. More work is needed to assess the utility and accuracy of such combined models.

The variation of local TPB overpotential/activity quantities as affected by local pathway-dependent factors in heterogeneous electrodes was also reported by [59, 94]. Further, other factors associated with local current pathways, such as constrictivity [46, 59, 77], are known to contribute to local activation/Ohmic overpotentials. Thus, it appears that ERMINE captures these features effectively, but more work is needed to fully model or quantify them. Finally, because the overall difference between the synthetic data sets in ERMINE and DREAM SOFC have been correlated to local differences in ionic transport, it can be further concluded that the unique shape of the COM-0.48 data arises from significantly different ionic transport paths, as compared to the synthetics. This difference is likely correlated to the unique volume fraction variation/heterogeneity within the subvolumes of the COM-0.48 data.

4.4.4 Local current density distributions and hotspot analysis

In prior sections, it was concluded that local ionic transport in YSZ significantly influenced the overall performance and the local TPB performance; furthermore, its impact on either was a function of standard deviations in the particle sizes and local volume fractions within subvolumes of $L^* \approx 20$. In Section 4.4.3, it was shown that a combination of increased local tortuosity and increased local current densities are likely origins of the difference in ERMINE and DREAM SOFC. Thus, the local current density within the YSZ phase (j_{YSZ}) is investigated here for all microstructural types.

A rendering of j_{YSZ} for a single COM-0.48 subvolume is given in Figure 4.4.6a. Only the YSZ phase is rendered, and the color indicates the

magnitude of j_{YSZ} at $\eta = 0.2$ V. It can be seen readily that high current density regions (red), herein called *hotspots*, exist non-uniformly throughout the YSZ phase. While the average current density is 1.2 $\mathrm{A\,cm^{-2}}$, the current densities in hotspots can be greater than than 10 $\mathrm{A\,cm^{-2}}$ (more than an eight-fold increase). (Note, the colorbar range was manually set for ease of visualization but does not contain the full value range.) An example of increased local current density at a constricted YSZ channel is shown in Figure 4.4.6b. In the narrowest region of the channel, the current density is more than 10 $\mathrm{A\,cm^{-2}}$. Such hotspots represent the upper tail of the j_{YSZ} distribution and are related to local constrictions or bottlenecks in the transport paths, resulting in a high local flux (Figure 4.4.6b). Constrictions (or the constrictivity of the transport network) are known to impact electrode performance [46, 59], though they are less widely included in EMT models than tortuosity. It is reasonable to consider that these constrictions contribute to the differences found above for transport from local TPBs (Section 4.4.3), and to potential degradation mechanisms related to high or nonuniform local current densities, as discussed by Bertei et al. [4].

To isolate the hotspots for further analysis, they were extracted from the microstructures as follows. First, the element node-sampled distribution (plotted in Figure 4.4.6a) of j_{YSZ} was converted to an element volume-sampled distribution, and the volume of each element was used to create a volume-weighted distribution, for which the mean ($\overline{j}_{\mathrm{YSZ}}$) and standard deviation ($\sigma_{j_{\mathrm{YSZ}}}$) were determined. The scalar field of j_{YSZ} magnitude was then thresholded when the local value was greater than $\overline{j}_{\mathrm{YSZ}} + \beta\sigma_{j_{\mathrm{YSZ}}}$, where β is a multiplier and was set as $\beta = 5$. For all subvolumes, $\overline{j}_{\mathrm{TPB}} + 5\sigma_{j_{\mathrm{YSZ}}}$ corresponds to roughly the same total volume of the volume-sampled j_{YSZ} (see Table 4.6.4).

After thresholding, the DBSCAN algorithm [27] (in the `sklearn` Python library) was applied to spatially cluster the mesh element volume-sampled field of j_{YSZ} into individual hotspots, defined as a clustered group of mesh elements (holding extremely high values of j_{YSZ}) that are adjacent or very close to each other in space. A 3D spatial plot of the hotspots extracted from the data shown in Figure 4.4.6a is given in Figure 4.4.6c (and Fig-

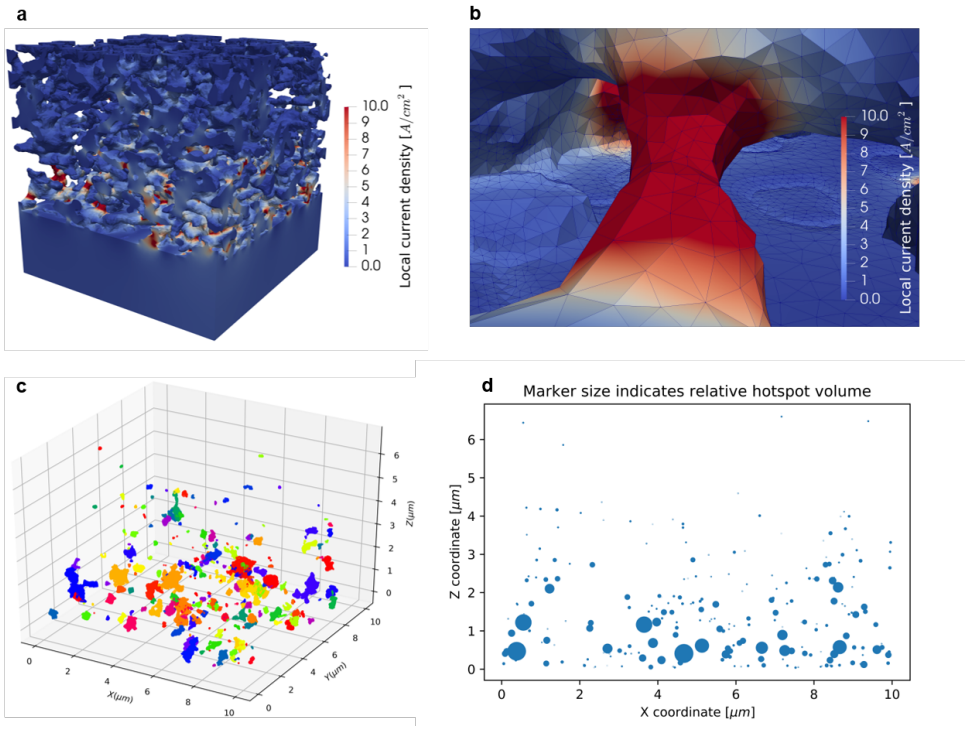

Figure 4.4.6: Visualization of local current density in YSZ (j_{YSZ}) and regions of high j_{YSZ} (hotspots) for a COM-0.48 subvolume. (a) Rendering of j_{YSZ} in the YSZ phase. (b) A hotspot located at a bottleneck, or constriction zone, in the YSZ phase. Color indicates magnitude of j_{YSZ}. The colorbar range was manually set for ease of visualization and does not contain the full value range. (c) Extracted hotspots after thresholding and clustering the field of j_{YSZ} shown in (a). Color indicates separateness of the hotspots. (d) 2D projection of the local hotspots shown in (c). Marker size indicates relative hotspot volume.

ure 4.6.3 shows the same for one of each of the synthetic microstructures). The hotspots/clusters are colored to distinguish distinct clusters. An X-Z plane projection of the spatial distribution of the hotspots is shown in Figure 4.4.6d, where each hotspot's X and Z coordinates were calculated (by averaging the coordinates of the hotspot's constituent elements) and plotted into a scatter plot. The marker size indicates relative hotspot volume, which was calculated by summing the hotspot's constituent element volumes. It is immediately evident in Figure 4.4.6d that there is a variation in the hotspot sizes and locations. In general, there is a high concentration of hotspots—as

well as large hotspots—near the cathode/electrolyte interface (Z = 0). Also, the spatial distribution in the X direction appears somewhat heterogeneous. Similar observations were made for all subvolumes when analyzed in this fashion (as illustrated in Figure 4.6.4).

The above hotspot analysis was applied to all subvolumes. The number of hotspots for each subvolume is plotted in Figure 4.4.7a as a function of ρ_{TPB}. Interestingly, this plot is reminiscent of the $j_{\eta=0.2V}$-ρ_{TPB} data plotted in Figure 4.4.1c. For the synthetic microstructures, the number of hotspots is roughly linear with ρ_{TPB}, with a significant variation in the number of hotspots per microstructural type (vertical distribution). The COM-0.48 subvolumes have significantly lower numbers of hotspots than the synthetics would at that value of ρ_{TPB}, and essentially lower numbers than the SYN-0.50, which has lower ρ_{TPB}values.

The distribution of hotspot volumes from all subvolumes were grouped by microstructural type ($\sigma_a/\ \overline{a}$) and plotted as standard boxplots in Figure 4.4.7b, with the mean (μ) and standard deviation (σ) of the volumes listed. For the synthetic electrodes, the mean value increases slowly from 0.003 to 0.005, while the standard deviation increases from 0.006 to 0.014. The COM-0.48 data has a larger mean (0.008) and standard deviation (0.020) than any of the synthetics. Further, the outliers (black circles) for all distributions skew to larger volumes and their maximum values follow the same trend: the volume of outliers increases with $\sigma_a/\ \overline{a}$ for the synthetics, and the COM-0.48 data contains a longer tail of outliers, indicating more larger hotspots. Here the outliers are values greater than $Q_3 + 1.5\mathrm{IQR}$, where Q_3 is the upper quartile and IQR is the interquartile range.

If one only considers hotspots above a certain volume such as $0.5V_s$, where V_s is the volume of a spherical particle of the mean particle size (0.46 µm), observations similar to Figure 4.4.7b can be made. The number of large volume hotspots ($> 0.5V_s$) for each microstructure is plotted versus ρ_{TPB} in Figure 4.4.7c. The trends observed in Figure 4.4.7a are reversed in Figure 4.4.7c: the number of large volume hotspots decreases with ρ_{TPB} for the synthetics, and there are more large hotspots for the COM-0.48 cathodes than expected for their ρ_{TPB} values. The outliers in Figure 4.4.7b were

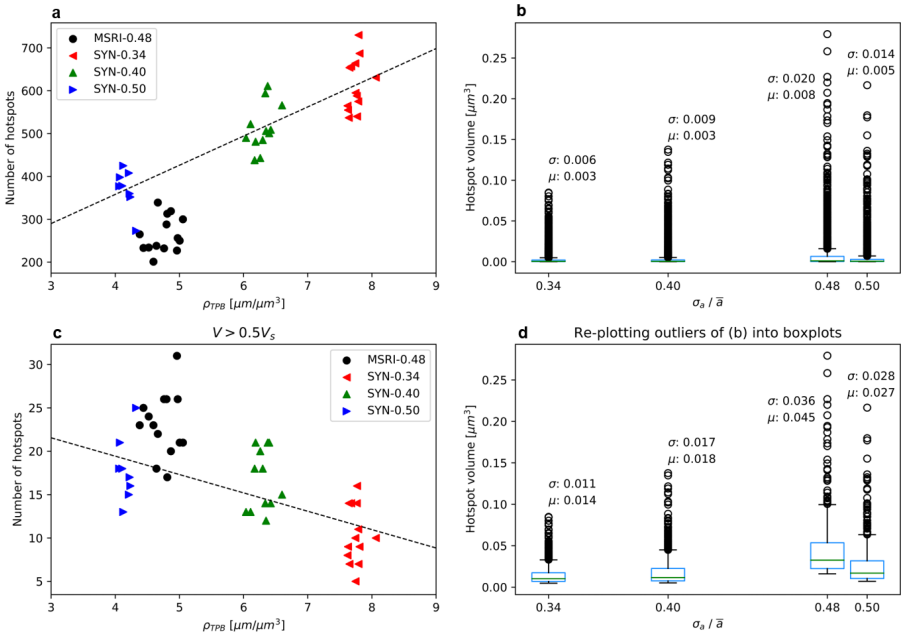

Figure 4.4.7: Comparison of hotspot distributions based on all 47 subvolumes. (a,c) Number of hotspots plotted against ρ_{TPB} for all subvolumes. The dotted-lines are linear fits applied to the synthetic microstructures, excluding COM-0.48. (c) only shows hotspots larger than 0.5 V_s, where V_s is the volume of a spherical particle with the mean particle size (0.46 μm). (b,d) Boxplot of hotspot volumes from all subvolumes grouped by the microstructure type, with the average (μ) and the standard deviation (σ) annotated for each microstructure. Outliers are shown as black circles. (d) is a boxplot for the outliers shown in (b).

extracted and re-plotted as boxplots in Figure 4.4.7d, again grouped by microstructural type ($\sigma_a/\ \overline{a}$), with the mean (μ) and standard deviation (σ) of the volumes listed. For the synthetics, the mean value increases from 0.014 to 0.027, while the standard deviation increases from 0.011 to 0.028. Again, the COM-0.48 has a larger mean (0.045) and standard deviation (0.036) than any of the synthetics. Further, the outliers (black circles) for all distributions are similar to that reported for Figure 4.4.7b.

This analysis indicates that the number and the volume of hotspots are a function of $\sigma_a/\ \overline{a}$: the number decreases with $\sigma_a/\ \overline{a}$ and the volume increases with $\sigma_a/\ \overline{a}$. Furthermore, the distributions of the hotspot size/volume in COM-0.48 cathodes are functionally different from those of the synthetic

microstructures; the hotspot number {size} distribution of COM-0.48 is distinctively weighted to smaller {larger} values. The distinctive heterogeneity of the commercial cell cathode, being an increased standard deviation in the local volume fraction within the subvolumes themselves [48], results in a functionally different distribution of local YSZ current density throughout the microstructure. The ERMINE output clearly shows widespread constrictions in the microstructures and their impact on local current density distribution is significant. This finding supports the idea that constrictivity is important for local ionic transport and helps explain the differences in ionic transport discussed in Section 4.4.3. More work is needed to quantify the relative importance of constrictions in current flow and differences in local tortuosity values from TPBs.

In Section 4.4.3, the DREAM SOFC model was adjusted manually by increasing the effective tortuosity term to bring its output closer into agreement with that from the ERMINE model. Similar outcomes may arise from including constrictivity terms in EMT models. This work demonstrates that high-throughput 3D simulations locally resolved over the 3D microstructure (such as ERMINE) can be used to develop improved EMT models that include local tortuosity and constrictivity relationships. Beyond improving models of average/effective properties, local hotspots can also be correlated to degradation events linked to local current density, such as Ohmic heating where the local heat generation rate is $j^2 r$, where r is the resistivity of YSZ. In other words, variation in local current density leads to even more variation (squared) in local heat generation, and high thermal gradients may likely cause degradation related to thermal stresses. Overall, the analyses in Section 4.4.3 and 4.4.4 show the potential for using ERMINE to inform models of different degradation modes, including local overpotenial and current density hotspots.

4.4.5 Summary

47 subvolumes of complex, three-phase electrode microstructures, each having dimensions of $10 \times 10 \times 7$ µm^3, or $L^* = 21.7$ {15.2} in the horizontal {vertical} directions, were subjected to a high-throughput workflow to simulate

electrochemistry and transport in SOFC cathodes using HPC platforms. All but the mesh generation software are open-source packages, including the MOOSE framework that runs ERMINE; the codes, microstructures, and data are available as indicated in the Supplementary Material (Sec. 4.6). The size of each subvolume and the total number of subvolumes simulated are large relative to those investigated in prior computational works [4, 6–9, 38, 55, 61, 64, 65, 81, 89, 93, 105, 108, 111, 134]. The size is larger than needed to fully represent local electrochemistry, and the number of subvolumes, spread across 4 distinct microstrutural types, yields initial understanding of statistical variations on local values within a microstructural class. The overall time required for meshing and simulating all 47 sub-volumes was $\approx$ 10 days. The inclusion of both two and three phase reaction pathways in ERMINE did not significantly increase the clock time for simulations (from an earlier instantiation [47]), and only the TPB pathway contributes significantly for the specific materials properties investigated. These observations indicate that there is a significant room for growth in HPC simulations for SOFCs, including overall volumes, increased complexity in physics, full cell simulations, etc. The yield on convergence of simulations was 87 %, which is high but can also be improved in the future.

ERMINE was used to compare four different types of microstructures reported previously [48]: three synthetics having controlled variations in the standard deviation of their particle size distribution and a commercial cell that had both a specific standard deviation in the particle size and a variation in the local volume fractions over the length scales considered herein. The ρ_{TPB} values are linearly correlated to the mean normalized standard deviation in particle size $\sigma_a / \overline{a}$ (for a constant mean particle size), for both the synthetics and commercial cells. However, the commercial cells have a significant simulated underperformance, or depressed effective current density output, and a substantially higher variability in effective performance. Throughout the work, the effect of the internal volume fraction variations that exist within the COM-0.48 cathode differentiates it from the synthetic cathodes.

Comparison of the average ERMINE output with two EMT models indicates that the heterogeneity is strongly tied to specifics of the local ionic

transport in YSZ. The two EMT models do not capture this variation precisely, though average values near typical operating conditions are all similar. Extracting effective exchange current densities and Ohmic resistances indicate that the primary difference between the results from the EMT models and ERMINE, as well as between the commercial and synthetic microstructure results, came from the ionic transport path through the electrode. Because ERMINE is a high-throughput method on HPC platforms, it can be used to develop improved EMT models that capture local microstructural impacts more precisely.

The importance of the ionic transport path is borne out further when considering local properties extracted from the locally resolved ERMINE simulations, such as local overpotential at the TPBs and local current density in YSZ. The commercial cathode suffers from poor local ionic transport as compared to the synthetic electrodes, resulting in increased Ohmic (decreased activation) overpotentials at TPBs, and an increase in the number of large volume hotspots (constrictions) in the YSZ transport network, and significantly wider variations on those values. ERMINE captures the local pathway-dependent parameters, including tortuosity, constrictivity, and local current density, which are all seen to affect the cathode performance. Access to local values of overpotential and current density will inform more accurate local degradation models, including chromium poisoning and local heating related issues.

4.5 Conclusions

A high-throughput, high-performance computational approach was presented to simulate local electrochemistry in three dimensions resolved over microstructural features of solid oxide fuel cell electrodes. The model retains full details of the microstructure as complex finite element meshes and it models local reaction-transport of relevant electrochemical species. Simulations were carried out on 47 meshed three-phase cathode volumes, whose lateral {vertical} dimensions are each approximately 22 {15} times the average particle size (0.46 µm for all). The 47 microstructures are spread across four distinct groups—one commercial cell cathode and three synthetic cathodes—

having different standard deviations of the particle size and/or the local volume fraction distributions. The simulation output from the locally-resolved model was compared to those of two accepted EMT models. Analysis of the data generated from these models results in the following findings and conclusions.

- The average performance simulated from the locally-resolved model compares favorably to the EMT models, indicating the local physics are accurately captured.

- The largest discrepancy between the locally-resolved simulations and the EMT models arises from the local ionic (Ohmic) transport in the YSZ phase of the active cathode. Analysis of local activation overpotential at TPB sites and local current density in YSZ reinforce this.

- Constriction of local current density was shown by the locally-resolved simulations to be widespread in all microstructures, but this is not accounted for by either EMT model. Thus, high-throughput locally-resolved simulations offer a path to informing/improving the accuracy of EMT models.

- The ability of the locally-resolved model to compute fields of activation overpotentials and current density hotspots demonstrates the potential for using locally-resolved simulations to better inform models of local degradation mechanisms.

- The distinctive heterogeneity of the commercial cathode, previously captured as variations in local volume fractions, clearly impacts the electrochemical properties simulated by the locally-resolved models; the commercial microstructure results in distinctive distributions of (1) effective voltage-current performance output, (2) local activation overpotentials at TPB sites, and (3) local current densities in YSZ.

- The distinctive distributions of local electrochemical quantities contribute unfavorably to the ionic transport terms, resulting in the commercial microstructure having the worst overall performance relative

to the synthetic microstructures, despite not having the lowest values of TPB density.

- Many of these findings can be attributed to the high-performance, high-throughput nature of the presented computational approach, allowing locally-resolved simulations of many microstructural volumes, with each having large enough size to compute accurate local properties. Such methods offer a large-data, statistical approach to understanding fuel cell performance characteristics, which will underpin the development of high-durability, high-reliability electrochemical cells.

4.6 Supplementary Material

4.6.1 Microstructural properties for all subvolumes

The four microstructure datasets used in this work were scaled and cropped into 54 subvolumes, 47 of which resulted in converged ERMINE simulations. Here the microstructural properties relevant to the TFV and DREAM SOFC models are tabulated for all of the 47 subvolumes, as shown in Table 4.6.1. The first row denotes the parameter, where θ is the volume fraction, τ is the tortuosity factor, $\overline{a}$ is the *volume-weighted* mean particle size [µm], ρ_{TPB} is the TPB density [µm^{-2}], and A_i is the interfacial surface area per unit volume [µm^{-1}]. The second row denotes the phase, where 1, 2, and 3 correspond to pores, LSM, and YSZ, respectively. Details regarding the measurements of these parameters (except for the TPB density) were described in [26, 48]. The TPB density was measured by summing the mesh element perimeters that are at the intersection of three phases after meshing the three-phase microstructures.

It can be seen that the *volume-weighted* particle sizes in Table 4.6.1 do not precisely match the *number-weighted* mean particle size (0.46 µm) mentioned in the main text, especially for SYN-0.34 and SYN-0.40 subvolumes. This is because the scaling of the microstructures (before subvolume cropping) was based on the *number-weighted* mean particle sizes reported in [48], and the subvolume-specific particle sizes (after cropping) were calculated based on *volume-weighted* distributions of particle sizes. Both definitions of the

mean particle size are fundamentally different and thus result in different values [48]. However, the values listed in Table 4.6.1 are not significantly far from 0.46 µm. Furthermore, the difference in the particle size (e.g., from 0.30 to 0.46 µm) have been found to have negligible influence on TFV and DREAM SOFC output. Finally, the measurements of the other parameters were independent of the particle size.

Table 4.6.1: Relevant microstructural properties for all subvolumes

	θ			τ			$\overline{a}$			ρ_{TPB}	A_i		
	1	2	3	1	2	3	1	2	3		1/2	1/3	2/3
SYN-0.34	0.34	0.28	0.38	1.32	1.51	1.27	0.30	0.28	0.34	7.74	1.48	1.82	1.51
	0.34	0.28	0.38	1.33	1.54	1.27	0.31	0.28	0.34	7.65	1.48	1.80	1.47
	0.34	0.28	0.37	1.33	1.46	1.30	0.32	0.28	0.35	7.64	1.46	1.77	1.47
	0.34	0.28	0.38	1.32	1.51	1.28	0.31	0.28	0.34	7.68	1.47	1.81	1.46
	0.34	0.28	0.38	1.33	1.47	1.28	0.31	0.28	0.34	7.63	1.47	1.80	1.47
	0.34	0.28	0.38	1.32	1.49	1.27	0.30	0.28	0.34	7.77	1.49	1.83	1.49
	0.33	0.28	0.39	1.35	1.49	1.26	0.31	0.28	0.35	7.62	1.43	1.80	1.51
	0.34	0.28	0.38	1.32	1.49	1.28	0.31	0.27	0.33	8.06	1.52	1.81	1.52
	0.34	0.28	0.38	1.34	1.52	1.26	0.30	0.28	0.34	7.81	1.47	1.84	1.48
	0.34	0.28	0.38	1.33	1.52	1.27	0.31	0.28	0.34	7.74	1.46	1.80	1.50
	0.34	0.28	0.38	1.32	1.49	1.27	0.30	0.27	0.34	7.79	1.48	1.83	1.50
	0.34	0.28	0.38	1.32	1.50	1.27	0.31	0.28	0.34	7.79	1.47	1.80	1.49
	0.34	0.28	0.39	1.34	1.56	1.27	0.30	0.27	0.34	7.76	1.46	1.81	1.55
SYN-0.40	0.35	0.28	0.37	1.34	1.51	1.29	0.37	0.33	0.39	6.11	1.29	1.60	1.31
	0.35	0.28	0.37	1.31	1.52	1.30	0.39	0.34	0.41	6.04	1.27	1.56	1.27
	0.35	0.28	0.37	1.33	1.50	1.31	0.38	0.34	0.40	6.17	1.31	1.57	1.29
	0.34	0.29	0.37	1.33	1.47	1.28	0.37	0.33	0.39	6.40	1.33	1.57	1.34
	0.35	0.28	0.37	1.33	1.44	1.30	0.38	0.34	0.39	6.19	1.29	1.57	1.30
	0.33	0.30	0.37	1.35	1.42	1.31	0.36	0.34	0.39	6.38	1.34	1.54	1.37
	0.35	0.29	0.36	1.33	1.47	1.32	0.39	0.33	0.39	6.60	1.37	1.55	1.32
	0.34	0.30	0.36	1.34	1.44	1.32	0.37	0.33	0.39	6.42	1.38	1.53	1.33
	0.34	0.30	0.36	1.33	1.45	1.31	0.37	0.33	0.39	6.34	1.35	1.56	1.32
	0.34	0.29	0.37	1.34	1.48	1.29	0.37	0.34	0.39	6.35	1.32	1.55	1.34
	0.34	0.29	0.37	1.34	1.45	1.30	0.38	0.33	0.40	6.26	1.32	1.55	1.31
	0.32	0.29	0.38	1.37	1.44	1.27	0.36	0.33	0.40	6.30	1.32	1.54	1.38
COM-0.48	0.35	0.29	0.35	1.27	1.64	1.31	0.42	0.52	0.46	4.80	1.38	1.90	1.39
	0.36	0.31	0.33	1.27	1.53	1.35	0.44	0.52	0.40	5.05	1.43	1.81	1.46
	0.37	0.32	0.31	1.28	1.45	1.41	0.51	0.56	0.49	4.52	1.50	1.56	1.32
	0.37	0.33	0.30	1.27	1.43	1.40	0.49	0.56	0.41	4.59	1.47	1.62	1.36
	0.36	0.32	0.32	1.29	1.49	1.36	0.46	0.59	0.39	4.96	1.45	1.78	1.36
	0.39	0.32	0.29	1.25	1.44	1.40	0.54	0.56	0.38	4.64	1.45	1.61	1.37
	0.37	0.31	0.32	1.27	1.48	1.36	0.45	0.54	0.39	4.87	1.49	1.80	1.39
	0.36	0.31	0.33	1.27	1.56	1.36	0.45	0.54	0.42	4.66	1.45	1.79	1.35
	0.37	0.31	0.32	1.25	1.54	1.38	0.46	0.53	0.41	4.76	1.45	1.81	1.33
	0.38	0.30	0.32	1.24	1.64	1.34	0.47	0.56	0.40	4.38	1.40	1.85	1.27
	0.37	0.34	0.29	1.25	1.48	1.39	0.48	0.62	0.39	4.44	1.50	1.61	1.31
	0.37	0.32	0.31	1.26	1.44	1.37	0.45	0.53	0.40	5.00	1.51	1.75	1.41
	0.36	0.32	0.32	1.26	1.56	1.35	0.42	0.54	0.39	4.97	1.46	1.89	1.40
	0.37	0.30	0.34	1.26	1.62	1.37	0.46	0.52	0.41	4.81	1.40	1.84	1.38
SYN-0.50	0.33	0.31	0.36	1.37	1.43	1.31	0.47	0.45	0.49	4.11	1.10	1.27	1.11
	0.35	0.31	0.34	1.33	1.45	1.31	0.52	0.46	0.50	4.22	1.09	1.24	1.07
	0.34	0.29	0.37	1.35	1.51	1.29	0.51	0.42	0.52	4.07	1.07	1.29	1.07
	0.34	0.31	0.35	1.37	1.52	1.32	0.49	0.46	0.48	4.23	1.10	1.25	1.12
	0.31	0.30	0.38	1.39	1.49	1.30	0.49	0.45	0.54	4.06	1.01	1.23	1.14
	0.34	0.31	0.35	1.38	1.49	1.33	0.50	0.43	0.50	4.32	1.10	1.26	1.11
	0.32	0.31	0.37	1.46	1.50	1.28	0.49	0.46	0.51	4.12	1.06	1.23	1.16
	0.33	0.28	0.39	1.39	1.56	1.26	0.49	0.42	0.52	4.21	1.03	1.31	1.14

4.6.2 ERMINE model parameters

The model parameters for ERMINE are listed in Table 4.6.2. Note that for each subvolume, ERMINE operates in the potentialstatic mode and computes the local electrochemistry, including local current density, across a range of the global overpotential (η_{model}) from 0 to 0.4 V. Boundary condition values are denoted as BC.

Table 4.6.2: List of model parameters

Notation	Description	Value	Unit	Reference
T	Temperature	1073	K	-
$p_{O_2,C}$	[BC] Oxygen partial pressure at top of cathode	0.21	atm	-
$p_{O_2,CE}$	Oxygen partial pressure at counter electrode	1×10^{-20}	atm	-
E_{model}	Reversible half-cell potential	1.028	V	-
$\phi_{YSZ,CE}$	[BC] YSZ potential at counter electrode	0	V	-
η_{model}	Model (global) overpotential	0 - 0.4	V	-
D_{O_2}	Oxygen gas diffusivity	0.64	cm^2/s	-
$D_{O,LSM}$	Oxygen diffusivity in LSM	7.5×10^{-7}	cm^2/s	[3]
γ_{YSZ}	YSZ ionic conductivity	4×10^{-2}	S/cm	[52]
k_{SE}	Chemical surface exchange coefficent	6.14×10^{-6}	cm/s	[127]
$j_{0,CT}$	Charge transfer exchange current density	0.193	A/cm^2	[36]
$j_{0,TPB}$	Lineal TPB reaction exchange current density	1×10^{-7}	A/cm	[93]
z	Number of electrons for TPB and charge transfer reaction	4	-	-
α	Symmetry factor for TPB and charge transfer reaction	0.5	-	-

4.6.3 Supercomputer usage

It is important to emphasize that each supercomputer/cluster is highly unique in its software environment, hardware specification, resource allocation, etc. As a result, there are many factors that can influence simulation convergence behavior and runtime. Nevertheless, for this work, ERMINE was implemented successfully in two different supercomputers (Joule and Bridges) and the simulations converged in similar time frames with essentially identical outputs. More specifically, all subvolumes were simulated in Joule, and some of the subvolumes were simulated in Bridges for verification. Table 4.6.3 shows the effective current density (j) output by Joule and Bridges across a range of model overpotential (η_{model}) input based on a COM-0.48 subvolume. The simulation in Joule was run using 256 cores distributed across 16 nodes, where each node consists of 16 cores. The simulation in Bridges was run using 252 cores distributed across 9 nodes, where each node consists of 28 cores. Apart from the difference in the core distributions, as well as the fundamental difference between the two systems, both simulations were run with exactly the same parameters. It can be seen that the effective current density outputs are essentially identical, with negligible differences in the high decimal places. Both simulations converged roughly within an hour.

Based on Table 4.6.3, we are confident that ERMINE can be implemented across multiple different HPC platforms with relative ease; given enough hardware resources, the choice of the supercomputer should not pose difficulty or impact to numerical convergence behavior, simulation runtime, and output precision.

At the time of this work, the CPUs used are 8-core 2.6 GHz Intel Sandy Bridge CPUs from Joule and 14-core 2.3-3.3GHz Intel Haswell CPUs from Bridges. Further public details of Joule and Bridges can be found at https://hpc.netl.doe.gov and https://www.psc.edu/bridges.

Table 4.6.3: Effective current density output by Joule and Bridges based on a COM-0.48 subvolume

η_{model} [V]	j (Joule) [A/cm^{-2}]	j (Bridges) [A/cm^{-2}]
0.004	0.005931836	0.005931685
0.0116	0.016171945	0.016171486
0.0260	0.036753762	0.036754306
0.04	0.059180984	0.059180739
0.08	0.149686208	0.149685157
0.12	0.30578202	0.305778968
0.16	0.562107554	0.562106973
0.2	0.957201468	0.957194729
0.24	1.540196415	1.540198332
0.288	2.574214565	2.574215171
0.3456	4.436694497	4.436694228
0.4	6.904549637	6.904553065

4.6.4 Statistics of thresholding local current density for all subvolumes

In each subvolume, the volume-weighted distribution of local current density in YSZ (j_{YSZ}) was determined. The mean ($\overline{j}_{\mathrm{YSZ}}$) and the standard deviation ($\sigma_{j_{\mathrm{YSZ}}}$) were then calculated for the threshold value of $\overline{j}_{\mathrm{YSZ}} + 5\sigma_{j_{\mathrm{YSZ}}}$. Values of j_{YSZ} higher than the threshold are kept and defined to be part of the *hotspots*, or regions of high local current density, while values lower than the threshold are discarded. Since j_{YSZ} is volume-sampled, each value of j_{YSZ} has an associated volume (of a mesh element). The sum of the element volumes that are thresholded, or V_t, is also calculated for each subvolume, as shown in Table 4.6.4. The unit for $\overline{j}_{\mathrm{YSZ}}$ and $\sigma_{j_{\mathrm{YSZ}}}$ is A/cm^{-2}. V_t is normalized by dividing by the cathode volume and is shown as a percentage of the cathode volume in Table 4.6.4.

It can be seen that the threshold scheme used in this work effectively results in extracting roughly the same amount of volume of the local j_{YSZ} field from each subvolume; V_t is about 0.4 to 0.5 % for all subvolumes. Although the values of V_t appear small relative to the cathode volume, the thresholded hotspots nevertheless appear quite dense throughout the cathode space, as shown in Section 4.6.7, indicating that the hotspot distribution is still likely to impact local and effective performance. In addition, since the threshold scheme extracts roughly the same total volume of hotspots from each subvolume, a change in the number of hotspots corresponds to a change in the overall hotspot volumes, e.g., more hotspots means each hotspot is smaller on average.

Table 4.6.4: Statistics of thresholding local current density (j_{YSZ}) for all subvolumes

	$\overline{j}_{\mathrm{YSZ}}$	$\sigma_{j_{\mathrm{YSZ}}}$	$\overline{j}_{\mathrm{YSZ}} + 5\sigma_{j_{\mathrm{YSZ}}}$	V_t [%]
SYN-0.34	1.58	1.31	8.15	0.42
	1.60	1.28	7.98	0.41
	1.55	1.30	8.06	0.46
	1.60	1.28	8.02	0.41
	1.57	1.31	8.12	0.43
	1.57	1.32	8.16	0.44
	1.61	1.27	7.94	0.42
	1.62	1.33	8.25	0.41
	1.64	1.27	7.98	0.40
	1.59	1.29	8.04	0.42
	1.59	1.31	8.12	0.43
	1.65	1.26	7.95	0.38
	1.63	1.27	7.96	0.42
SYN-0.40	1.40	1.19	7.35	0.43
	1.42	1.16	7.22	0.40
	1.38	1.22	7.48	0.47
	1.41	1.25	7.66	0.46
	1.42	1.21	7.47	0.41
	1.38	1.24	7.57	0.44
	1.42	1.25	7.70	0.41
	1.34	1.27	7.67	0.46
	1.41	1.22	7.51	0.43
	1.43	1.23	7.55	0.44
	1.35	1.26	7.65	0.47
	1.40	1.22	7.50	0.44
COM-0.48	1.20	1.13	6.87	0.51
	1.25	1.19	7.19	0.45
	1.12	1.18	7.04	0.48
	1.06	1.25	7.29	0.52
	1.18	1.21	7.22	0.53
	1.17	1.19	7.10	0.50
	1.21	1.16	6.99	0.46
	1.17	1.13	6.82	0.46
	1.14	1.21	7.17	0.52
	1.09	1.19	7.01	0.48
	1.11	1.20	7.11	0.47
	1.16	1.24	7.38	0.48
	1.15	1.21	7.22	0.49
	1.22	1.12	6.85	0.46
SYN-0.50	1.16	1.01	6.19	0.42
	1.12	1.07	6.48	0.44
	1.15	0.98	6.06	0.45
	1.14	1.06	6.43	0.44
	1.13	0.98	6.02	0.44
	1.10	1.12	6.72	0.53
	1.19	0.95	5.96	0.36
	1.17	0.99	6.11	0.41

4.6.5 Nonlinear fitting to effective performance curves

For each subvolume, the effective performance curve of cathode overpotential (η_c) versus current density (j) was fitted with the nonlinear function to extract the effective exchange current density (j_0) and the Ohmic resistance (R_{ohm}). Figure 4.6.1 shows the performance curve and the fitted curve from one subvolume of each microstructure type, for ERMINE and DREAM SOFC. It can be seen that the performance curves were well fitted by the nonlinear function, with the r-squared value of the fitting being 0.97 for the ERMINE data and 0.99 for the DREAM SOFC data. The fitted values of j_0 and R_{ohm} are also shown in each subfigure.

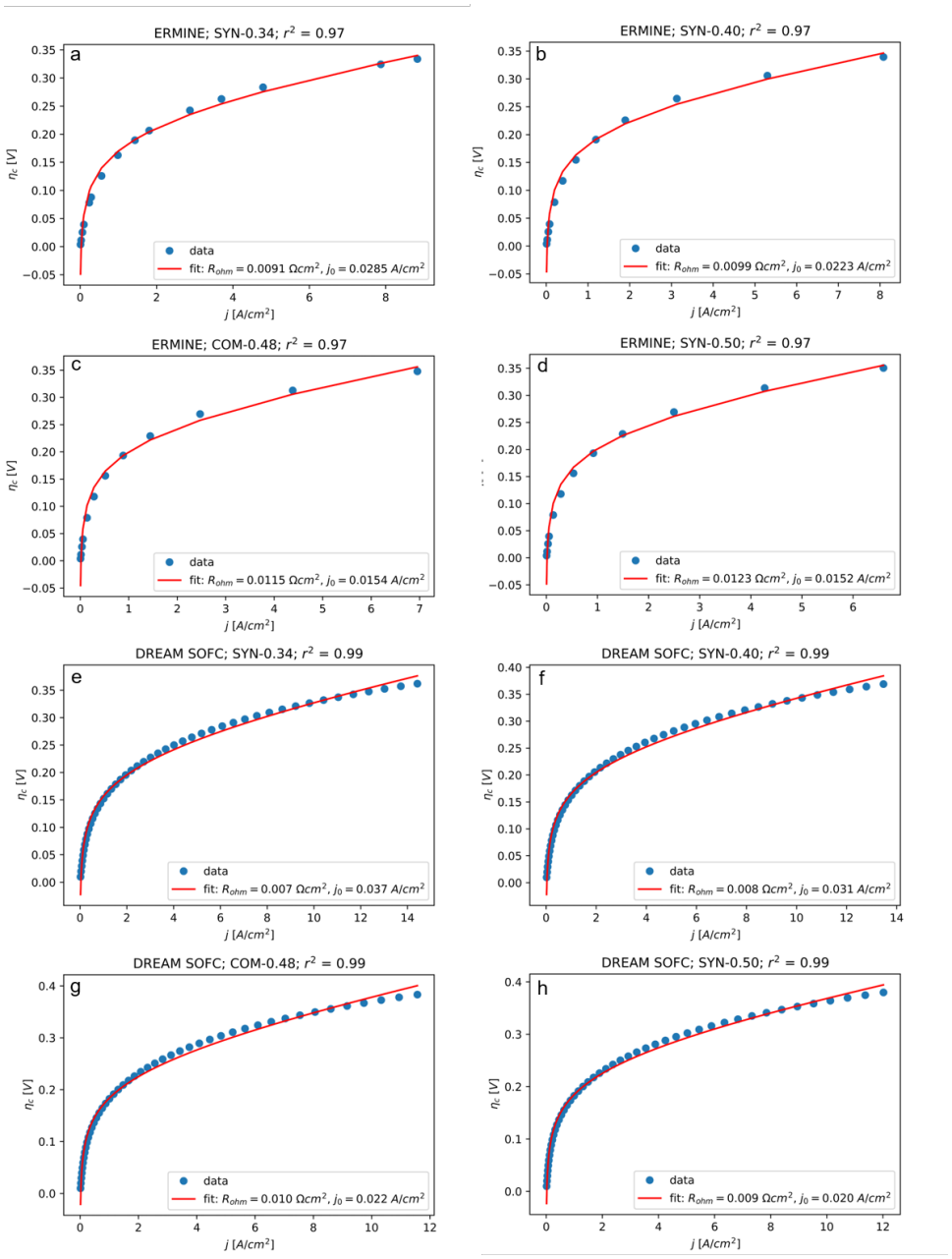

Figure 4.6.1: Effective performance curves and fitted curves for one subvolume of each microstructure type for both ERMINE and DREAM SOFC. Subfigure title indicates the model name, the microstructure type, and the r-squared value for the fitting.

4.6.6 The effect of tortuosity and TPB density on DREAM SOFC output

Figure 4.6.2 shows the impact of changing the YSZ tortuosity factor (τ_{YSZ}) and the TPB density (ρ_{TPB}) in DREAM SOFC simulations on two output performance metrics: the local activation overpotential at the TPBs (η_{TPB}) and the effective current density (j). η_{YSZ} is plotted versus the distance to the electrolyte (Z), while j is plotted across a range of global overpotential over the cathode (η_c). Each subfigure is based on performing DREAM SOFC simulations on the same COM-0.48 subvolume with manual changes in the values of τ_{YSZ} and ρ_{TPB}. Both τ_{YSZ} and ρ_{TPB} have significant impact on the performance metrics. Figure 4.6.2a and c indicate that an increase in τ_{YSZ} effectively suppresses the values of η_{TPB} and j. On the other hand, Figure 4.6.2b and d indicate that an increase in ρ_{TPB} effectively suppresses η_{TPB} but raises j. As described in the main text, simply modifying the tortuosity factors cannot bring both into agreement. Combining increased local tortuosity with increased local current density in constrictions is argued in the main text, using these figures, to explain discrepancies in the output of the two models.

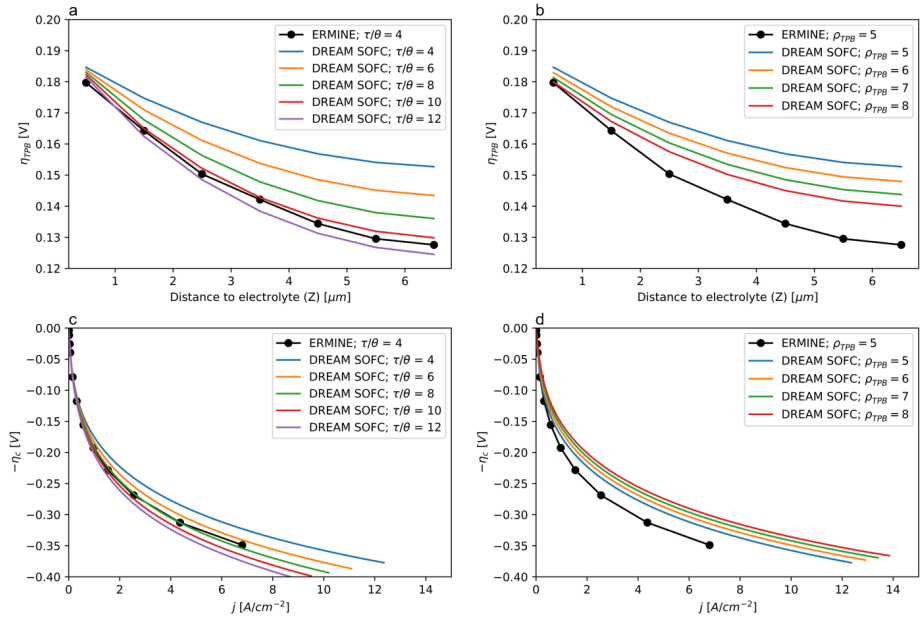

Figure 4.6.2: Impact of the YSZ tortuosity (τ_{YSZ}) and the TPB density (ρ_{TPB}) on the local activation overpotential at TPBs (η_{TPB}) and the effective current density output (j) based on DREAM SOFC simulations applied to one COM-0.48 subvolume. In (a) and (b), η_{TPB} is plotted versus the distance to the electrolyte (Z). In (c) and (d), j is plotted across a range of global overpotential applied across the cathode (η_c). In (a) and (c), τ_{YSZ} is altered such that the ratio of the YSZ tortuosity over the YSZ volume fraction (τ/θ) ranges from 4 to 12. In (b) and (d), ρ_{TPB} is altered such that its value ranges from 5 to 8 $\mu\mathrm{m}^{-2}$. In each figure legend, $\tau/\theta = 4$, or $\rho_{\mathrm{TPB}} = 5$, corresponds to the unaltered (original) data. Simulation output based on ERMINE is also plotted for comparison to DREAM SOFC.

4.6.7 Hotspot distribution visualization

After thresholding and clustering, the extracted hotspots from one subvolume of each synthetic microstructure type are shown in Figure 4.6.3. In each subfigure, the hotspots appear quite dense throughout the cathode volume and mostly concentrated towards the bottom of the cathode (or the cathode/electrolyte interface). The hotspots of the SYN-0.50 subvolume are noticeably fewer and larger than that of the other two subvolumes. This is further illustrated by Figure 4.6.4, which shows X-Z plane projection of the hotspot coordinates. The relative volume of each hotspot is indicated by the marker size. It can be seen that the hotspot distribution of the SYN-0.50 subvolume is less dense and significantly nonuniform along the X axis.

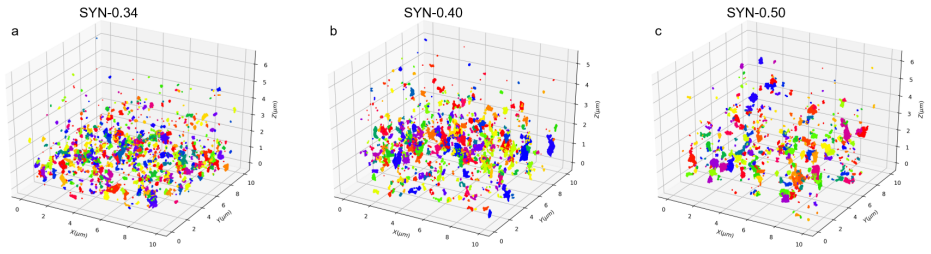

Figure 4.6.3: Extracted hotspots of local current density from one subvolume of each synthetic microstructure type. Subfigure title indicates microstructure type.

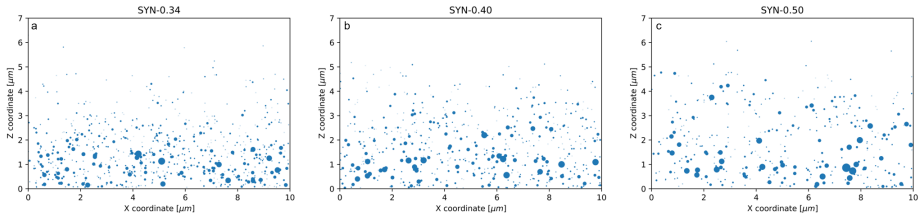

Figure 4.6.4: 2D projection of the local hotspots shown in Figure 4.6.3. Subfigure title indicates microstructure type. Marker size indicates relative hotspot volume.

5

High Performance Finite Element Simulations of Infiltrated SOFC Cathode Microstructures

This chapter is the second self-contained part of the thesis planned for academic journal publication. The following sections correspond to a standard journal structure (e.g., abstract, introduction, methods, results and discussion, conclusions), with an additional section for the supplementary material. Therefore, the chapter can be treated as a stand-alone paper.

5.1 Abstract

High-throughput, high-performance finite element simulations are presented that model electrochemistry and transport within dozens of solid oxide fuel cell cathodes containing synthetically generated nanoscale infiltrates. The computational approach retains the complex microstructural morphologies

of cathodes, including those of the three backbone phases (gas, ion, and electron conductors) and the infiltrates (an electron conductor), in meshed domains and computes distributions of local electrochemical quantities within the domains. Simulations were implemented on a supercomputer (each at 140 cores) and carried out on 48 distinct microstructural subvolumes, with varying backbone heterogeneities and infiltrate loadings, to investigate the impact of the infiltration on the electrochemical performance metrics of different cathodes. Analyzing both the ensemble (averaged over subvolumes) and the local (evaluated within subvolumes) performance metrics indicate that infiltration of an electron conductor significantly improves the electrochemical performance of each backbone, and does not modify the essential ionic transport properties of that backbone. These results shed light into the design and fabrication of optimal electrodes in fuel cells.

5.2 Introduction

Infiltration of solid oxide fuel cell (SOFC) electrodes, which is the process of introducing a nanoscale electrocatalyst phase to a pre-fabricated electrode backbone, has been reported to significantly improve their electrochemical performance [14, 53, 70–74, 78, 79, 107, 112, 119]. Infiltration thus modifies the local electrode morphology/microstructure, which in turn modifies local electrochemical activities and/or transport, resulting in improved overall (cell-level) performance. Additionally, some infiltration has been shown to reduce long-term degradation [28, 29]. The combination of increased electrochemical performance and decreased degradation are important targets for commercialization of SOFCs, and infiltration offers a potential cost-effective path to such electrode engineering. However, the effects infiltration has on microstructure-based local electrochemistry, and their implications for performance stability, are not well understood. To gain insight into such fundamental structure-performance relationships, methods to probe or simulate local electrochemical fields within an infiltrated electrode, in a spatially-resolved manner, are necessary.

Currently, it is intractable to experimentally determine local electrochemical quantities inside an electrode microstructure. It is possible to develop

numerical models that can be used to compute microstructural evolution, species transport, and local electrochemistry within a microstructural domain [13, 18, 63, 85, 97, 118, 124, 128], and the average output of such models compare favorably to average metrics of electrodes. Recently, we developed our own open-source simulation code, ERMINE, capable of high-throughput simulations on high-performance computing environments and used it to highlight statistical variations expected in SOFC electrodes, both between average values of different sub-volumes and between local values within all sub-volumes [49]. Less work has targeted understanding the effect of infiltration on microstructures. Liang et al. [76] used phase field modeling to study morphological evolution of infiltrated electrodes undergoing thermally-driven grain/particle coarsening. Yang et al. [128, 129] used continuum multiphysics modeling to simulate surface/bulk pathways of oxygen reduction reaction (ORR), simulating the effects of infiltration by changing effective rate constants or average microstructural properties to correspond expected values in infiltrated electrodes. There have not been reports that model infiltrated electrodes over spatially-resolved, meshed microstructural domains. In our experience, such a model requires significant computational resources, which have not been widely applied to SOFC electrode engineering research, but are becoming more readily available.

In this work, we use ERMINE, a spatially-resolved, morphology-preserving meshed model [49], to simulate electrochemistry and transport for both experimentally reconstructed and synthetically generated microstructures that were subsequently synthetically infiltrated with nanoscale particles using an in-house algorithm. All of the backbones considered here are composed of three phases—YSZ (yttria-stabilized zirconia, an ion conductor), LSM (lanthanum strontium manganite, an electron conductor), and air in pores (oxygen gas conductor)—and were simulated in our previous paper [49]. The infiltration algorithm introduces electron conducting LSM nanoparticles to the solid-pore surfaces within the cathode backbone, by reassigning a certain fraction of pore voxels at the solid-pore interfaces to be LSM seeds, followed by some dilation and smoothing functions. All simulations were implemented in parallel using high-performance computing (HPC) resources. Over 50 volumes were simulated, whose lineal dimensions were ≈ 20 times their av-

erage particle dimension and were spread across four distinct groups, each having a different standard deviation in particle size and/or local volume fraction distributions. Distributions of electrochemical quantities of infiltrated electrodes—within and across simulated domains—were investigated and compared against the values from the uninfiltrated backbones. This work represents a novel approach to understanding the effect of infiltration on microstructure-based local electrochemistry and provides opportunities for using simulation to engineer optimal SOFC electrode microstructures via infiltration.

5.3 Methods

The microstructures studied in this work, including their acquisition and analysis, were detailed in our previous works [48, 49, 82]. Briefly summarized, these microstructures include an experimentally captured commercial SOFC cathode microstructure (named COM-0.48) and three synthetically generated microstructures (named SYN-0.34, SYN-0.40, and SYN-0.50, respectively). COM indicates commercial microstructure of an SOFC purchased from MSRI (Salt Lake City, UT) and SYN indicates synthetic microstructures [48] generated using Dream.3D (BlueQuartz Software, Springboro, OH). The numbers in the names indicate the mean-normalized standard deviation of the particle size ($\sigma_a / \overline{a}$); it indicates the distribution width of the particle size and was used as a primary input for the generation of the synthetic microstructures. In our previous works [48, 49], it was reported that COM-0.48 exhibits distinctively large variations in the distributions of both microstructural properties and simulated effective performances. Further, COM-0.48 resulted in the lowest overall performance, even though it did not have the lowest TPB density nor did it have the highest $\sigma_a / \overline{a}$. Thus, COM-0.48 is considered a more heterogeneous microstructure relative to the synthetic ones having only particle size distributions incorporated.

All four microstructure types from [48, 49] were studied for this paper. From each microstructure type, five subvolumes of $10 \times 10 \times 7$ μm^3 were chosen from random locations within the large volume. For subvolumes of COM-0.48 and SYN-0.50, which are the most heterogeneous and have

the lowest performance [49], three different levels of infiltrate loading were performed, where infiltrate particles were artificially generated using an in-house algorithm that operates on the backbone microstructures in voxelated form, as shown in Figure 5.3.1. This work considers the backbone synthetic microstructures to be composed of pore-LSM-YSZ phases (i.e., the same as the commercially made COM-0.48 cathode), and the infiltrate phase to be the (perfect) electronic conductor LSM. The lack of any voltage drop within the constricted nanoparticle conducting pathway will serve to describe an upper bound on the performance enhancement from infiltration of electronic conductors. First in the infiltration algorithm, a fraction f of the pore voxels that are in contact with LSM/YSZ surfaces were randomly selected to instantiate seeds; those voxels were converted from pore to LSM, as indicated in Figure 5.3.1a and b. Without a clearer understanding of the true spatial distributions of nanoparticles on the solid phases, which may be controlled using processing methods, a random process was chosen to assess the impact of such an infiltration. Next, the seeds were dilated using a morphological dilation operation with a spherical kernel with a two voxel radius (which translates to a sphere with a five voxel diameter), as shown in Figure 5.3.1c. Finally, regions of original LSM/YSZ surfaces that were affected by the dilation were restored, roughly halving the dilated spherical particles. The result is a backbone microstructure populated with small hemispheres of particles, five-voxels-wide, randomly deposited on the solid surfaces, as shown in Figure 5.3.1d. As the voxel size of the microstructural domains is $\approx$ 20–30 nm [49], the in-plane width (out-of-plane height) of the infiltrate particles is on the order of 100–150 (60–90) nm.

The three different levels of infiltrate loading used were $f = 0.02,\ 0.04,\ 0.06$. 3D renderings of a COM-0.48 microstructure subvolume infiltrated at different values of f are shown in Figure 5.3.2. Although the values of f are small, the infiltrate distributions are dense on the LSM/YSZ surfaces, owing to the dilation step. The infiltration loading was determined from the resulting microstructures as fractional pore volume converted to LSM and fractional solid weight (assuming an LSM density of 6.5 $\mathrm{g\,cm^{-3}}$), which are shown in Figure 5.6.1 (Supplementary Material, Sec. 5.6). It can be seen

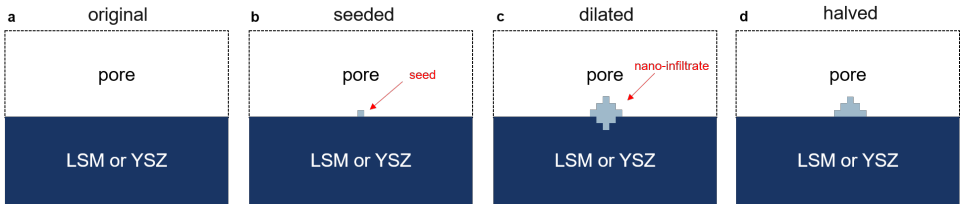

Figure 5.3.1: Diagram of infiltration algorithm. (a) Original LSM/YSZ surface in voxelated form. (b) A seed placed at a random pore voxel on the LSM/YSZ surface. (c) The seed is dilated using a spherical kernel. (d) Original LSM/YSZ surfaces are returned.

that the decrease in pore volume and the increase in solid weight are clearly impacted as f ranges from 0 to 0.06 (approximately in linear fashion). For the maximum loading of $f = 0.06$, the pore volume was reduced by roughly 8 % for COM-0.48 and 10 % for SYN-0.50, and the weight is increased by roughly 4–6 % for both. This level of infiltration is reasonable compared to literature values [32, 72, 74].

Infiltration of the three phase backbone with LSM is expected to modify directly the local electrochemically active sites, increasing the surface area of LSM when the infiltrate is on LSM and increasing the triple-phase boundary (TPB) density when LSM infiltrates on YSZ have connectivity with the LSM backbone. A schematic of this is shown in Figure 5.3.3, where the original TPB is morphologically modified owing to an isolated infiltrate straddling an original TPB. New TPB is formed around the infiltrate in contact with YSZ and the overall TPB segment is lengthened, contributing to an increase in TPB density. For the current set of the materials parameters used for ERMINE, the ORR occurs mostly through the three-phase boundary pathway (or TPB pathway) rather than the two-phase boundary pathway [47, 49] due to slow oxygen ion/vacancy transport in LSM and slow surface exchange at pore/LSM interface. The contribution of the former is many orders of magnitude greater than the latter. Therefore, the increase in TPB density contributes much more significantly to overall performance than the increase in LSM surface area does. In other words, even though a two-fold increase in LSM surface area may result in a two-fold increase in two-phase pathway

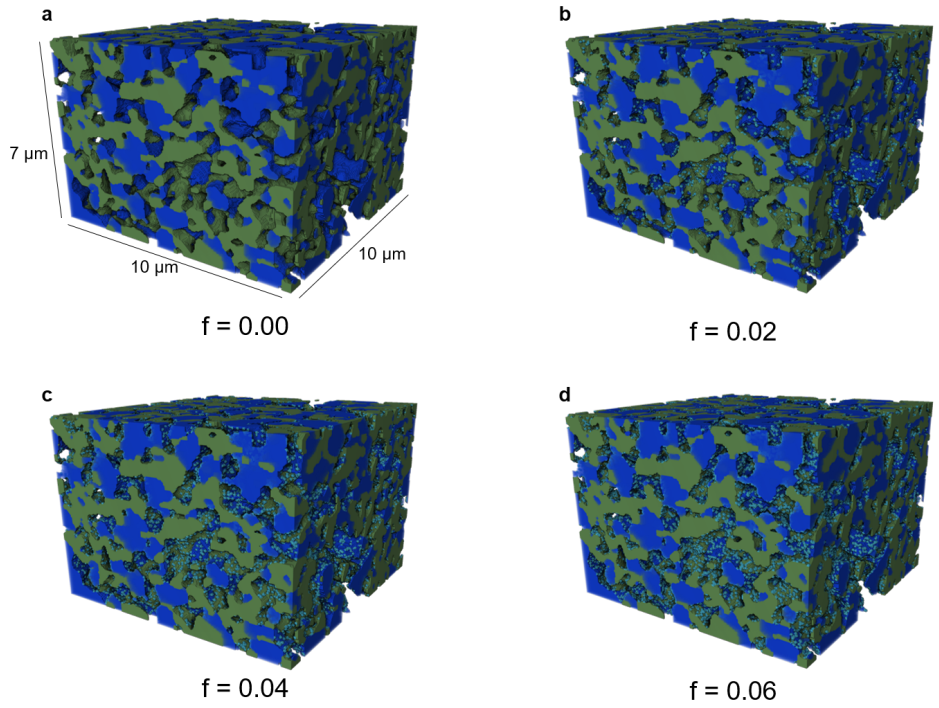

Figure 5.3.2: 3D rendering of a COM-0.48 subvolume infiltrated at different loading levels (or f). The pores are transparent. The LSM phase is blue. The YSZ phase is green. The infiltrate phase is cyan. (a) $f = 0.00$. (b) $f = 0.02$. (c) $f = 0.04$. (d) $f = 0.06$.

current contribution, such improvement in performance is negligible relative to the TPB pathway current output. This work therefore focuses on the increase in TPB density upon infiltration and the corresponding change in electrochemical performance.

Figure 5.3.4 shows the TPB densities (ρ_{TPB}) of the backbone microstructures (5 subvolumes each for COM-0.48 and SYN-0.50) as a function of infiltration seed fraction f. ρ_{TPB} increases substantially with increasing f; at $f = 0.06$, ρ_{TPB} is almost doubled for these microstructures. Note that only active TPBs are considered in this work, which are defined as the intersection of percolated pore, LSM, and YSZ phases. Details regarding the TPB density measurement were described in our previous work [49].

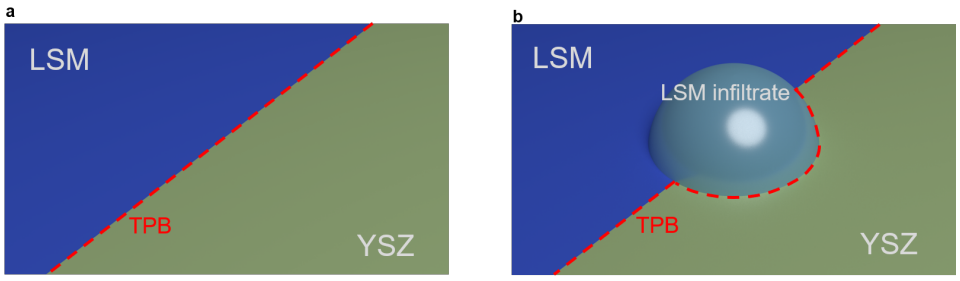

Figure 5.3.3: (a) 3D rendering of a TPB line at the pore-LSM-YSZ junction. Note that the pore phase is transparent. (b) 3D rendering of an infiltrate particle deposited at the TPB. Considering the infiltrate phase is LSM, the original TPB is effectively lengthened due to the formation of the new TPB formed around the infiltrate.

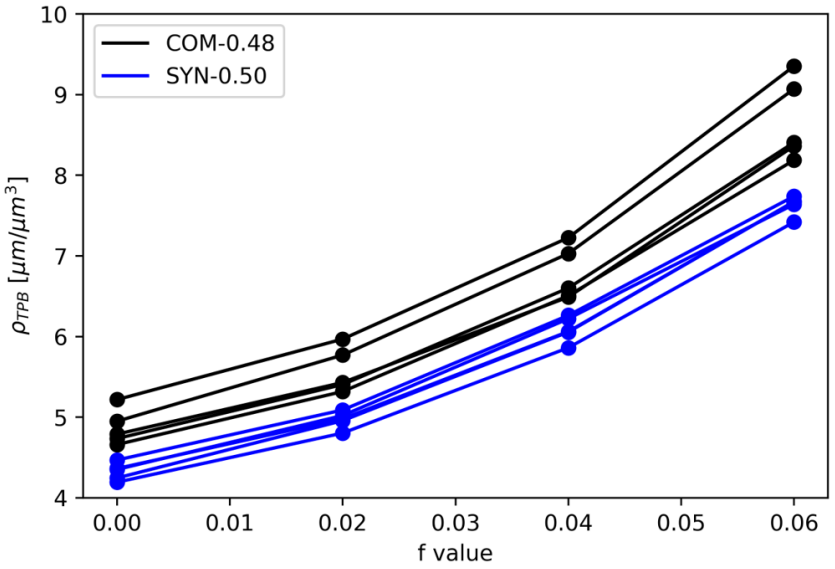

Figure 5.3.4: TPB density (ρ_{TPB}) as a function of f value for COM-0.48 and SYN-0.50 subvolumes.

Once infiltrated (or not), the microstructures were subjected to processing, meshing, and HPC simulations. Table 5.3.1 summarizes the ratio of the number of converged simulations to the number of attempted simulations with respect to the f value and the microstructure type. A total of 50 subvolumes—both backbone and infiltrated microstructures—were sub-

jected to meshing and simulation, and 48 resulted in numerical convergence. Note that the infiltrated microstructures originated from the backbones and thus are almost identical to the backbones (except at the infiltrate locations). Each simulation was run on the Bridges supercomputer [98] (Pittsburgh Supercomputing Center, Pittsburgh, PA) with 140 regular-memory cores over typically 2–5 hours. The hardware specifications can be found at https://www.psc.edu/bridges. The electrochemical simulation, as described in our previous work [49], is a reaction-and-transport model that simulates ORR pathways in a three-phase cathode microstructure. The simulation outputs scalar fields of electrochemical quantities (e.g., YSZ potential, activation overpotential at TPBs, etc.) throughout the microstructure. Ensemble (or effective) performance metrics can be extracted from the local electrochemical fields. Further details of the workflow encompassing meshing process, model implementation, and post processing were described in [49]. This work used the same model parameters as our previous work [49].

Table 5.3.1: Simulation convergence yield

Microstructure type	$f = 0.00$	$f = 0.02$	$f = 0.04$	$f = 0.06$
COM-0.48	5/5	5/5	5/5	4/5
SYN-0.34	5/5	-	-	-
SYN-0.40	5/5	-	-	-
SYN-0.50	5/5	5/5	5/5	4/5

5.4 Results and Discussion

The analyses of the simulation outputs largely follow those in our previous work [49]. Various electrochemical quantities were analyzed to gain insight into the effect of infiltration on cell performance. Some quantities are effective performance metrics, or those averaged over the whole subvolume, and some are direct performance metrics, which are local values of reaction and transport terms spatially distributed within the subvolume. Both quantities are discussed to elucidate the impact of nanoscale infiltration on performance of SOFC cathodes.

5.4.1 TPB density and Effective Performance

Two of the more general effective performance metrics, the global overpotential (η) and the global effective current density (j), were extracted from each of the 48 converged simulations. The η-j curves are shown in Figure 5.6.2, for all sub-volumes. As discussed above, infiltration of LSM into the LSM/YSZ/pore backbone is expected to increased the TPB density. The values of j at a fixed overpotential ($\eta = 0.20$) are plotted against the TPB density (ρ_{TPB}) in Figure 5.4.1. The values for the un-inflitrated backbones are given as closed circles of different colors, and are consistent with values reported previously from these sub-volumes (they were processed, meshed, and simulated again here for consistency of comparison with the infiltrated subvolumes). The dashed line represents the average performance of synthetic microstructures as a function of ρ_{TPB}, and the spread in individual sub-volumes around the average value is consistent with prior reports [49]. In this work, we focused infiltration on the two lower performing microstructures, SYN-0.50 (blue symbols) and COM-0.48 (black symbols). Note the un-infiltrated COM-0.48 data points sit below the average performance line of the synthetics, and perform worse (lower j at $\eta = 0.20$) than the SYN-0.50 that have lower TPB densities.

In Figure 5.6.2, it can be seen that increased infiltration values increase the current density output at a fixed overpotential, for the ten distinct subvolumes subjected to infiltration. It is clear in Figure 5.4.1 that ρ_{TPB} increases directly with infiltration, and this leads to a direct increase in j at $\eta = 0.20$. The average ρ_{TPB} values for SYN-0.50 are 5.0, 6.1, and 7.6 $\mu m/\mu m^3$ (which are increases of 16, 42, and 77 %) when f is 0.02, 0.04, and 0.06, respectively. For SYN-0.50, this improvement in j at $\eta = 0.20$ is approximately linear in ρ_{TPB}, with a slope similar to, but slightly shallower than, the slope of the average value for the synthetic backbones. The relative increase drops a bit between $f = 0.04$ and $f = 0.06$, perhaps indicating a diminishing return on increased TPB density with infiltration loading. Nevertheless, at $f = 0.06$, the ρ_{TPB} values are just slightly below those of the SYN-0.34 backbones, which are the most uniform and best performing of the electrode backbone microstructures. Note that the distribution of values

for the infiltrated microstructures does not narrow significantly on infiltration, instead each backbone increases with TPB density but also reflects the original location of the backbone in the distribution.

These observations are largely reinforced by the COM-0.48 simulations. The average ρ_{TPB} values for COM-0.48 are 5.6, 6.8, and 8.6 µm/µm^3 (which are increases of 14, 39, and 76 %) when f is 0.02, 0.04, and 0.06, respectively. Again, the improvement in j at $\eta = 0.20$ is approximately linear in ρ_{TPB}, with a slope shallower than the slope of the average value for the synthetic backbones, as well as of the SYN-0.50 infiltrated microstructures. Likewise, the relative increase drops a bit between $f = 0.04$ and $f = 0.06$, again indicating a diminishing return on increased TPB density with infiltration loading. Because of these observations, the relative location of an individual sub-volume does not move significantly within the distribution at the different infiltration values. Furthermore, the underperformance of the COM-0.48 microstructures, relative to the synthetic ones, worsens at a given ρ_{TPB} value (owing to the shallower slope), despite the increased TPB densities and increased performance relative to themselves. This is most notable at $f = 0.06$, because the ρ_{TPB} values for the COM-0.48 microstructures exceed all the synthetic microstructures, infiltrated or not. Yet, the j at $\eta = 0.20$ of COM-0.48 remain highly scattered and are significantly below the SYN-0.34 backbone performance values. These collected observations indicate that infiltration of LSM into LSM/YSZ/pore backbones is an effective method to increase ρ_{TPB} and j at $\eta = 0.20$ (or any overpotential value), but a signature of the original backbone remains for both the synthetic microstructures, having only particle size distribution in-built, and for the commercial microstructures, having both particle size and volume fraction distributions present [48].

5.4.2 Activation and ohmic contributions

The electrochemical model was simulated over an overpotential-current range (for these materials and microstructures) which results in two primary contributions to overpotentials: activation (Tafel) and Ohmic. The effective exchange current density (j_0), which quantifies the average activation con-

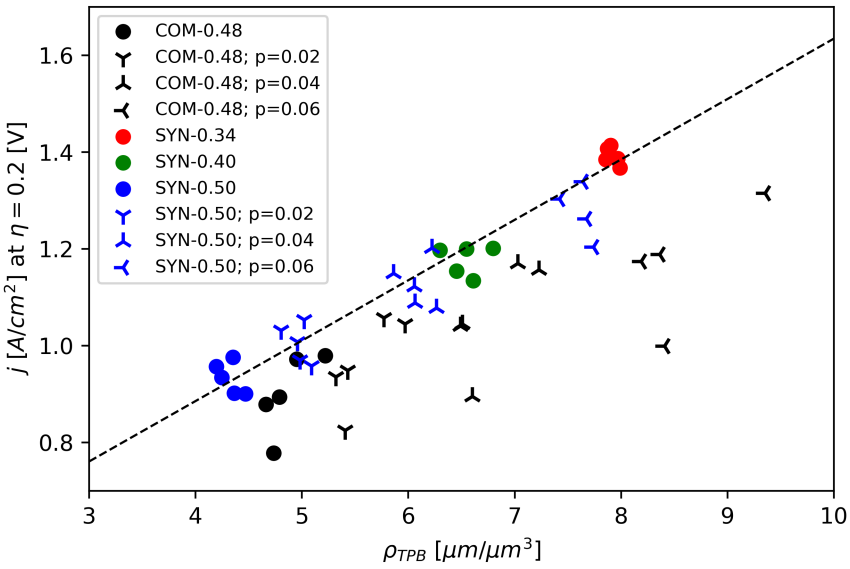

Figure 5.4.1: Values of j at $\eta = 0.2$ plotted against the subvolume-specific TPB densities. Note that each data point is based on one parallel simulation implemented on a supercomputer. The dashed line is a linear fit applied to the synthetic backbone microstructures.

tribution, and the effective Ohmic resistance (R_{ohm}), which captures the average Ohmic contribution, were extracted from individual η-j curves (as described in [49]). The effect of infiltration on these two values is quantified in Figure 5.4.2a,b, which plots the change in the values of j_0 (left axis, red circles) and R_{ohm} (right axis, blue x's), relative to the backbone only values ($f = 0$), as a function of f. Upon infiltration, j_0 increases significantly, on average for COM-0.48 (SYN-0.50) by 11.6, 30.4, and 56.7 % (12.6, 34.2, and 62.5 %), respectively for $f = 0.02$, 0.04, and 0.06. At the same time, R_{ohm} decreases with f, but only slightly: the average values for COM-0.48 (SYN-0.50) changed by 0.7, -0.4, and -3.6 % (0.4, -3.0, and -7.5 %), respectively for $f = 0.02$, 0.04, and 0.06. While both a j_0 increase and an R_{ohm} decrease contribute to improved overall performance, as indicated by Figure 5.4.1, the change in j_0 is more significant. This is consistent with a somewhat linear trend in j at $\eta = 0.20$ with ρ_{TPB}, since the activation term is primarily

associated with the TPB reaction, and the effective value linked to the total TPB density.

As observed for the backbones from a given microstructure type, there is a significant variation in performance metrics (See Figure 5.4.1 and [49]) owing to internal heterogeneities between subvolumes. Because the infiltration algorithm acts stochastically, one might envision variability in the effect of infiltration. One notes that the range of the relative change in either metric in Figure 5.4.2a,b appears to increase (it spreads out) with increasing f. The mean-normalized standard deviation of j_0 and R_{ohm} at each f value are plotted in Figure 5.4.2c,d. For both COM-0.48 (c) and SYN-0.50 (d), the mean-normalized standard deviations steadily increase, though the magnitude of these increases is on the order of 10–30 % (COM-0.48) and 20–60 % (SYN-0.50) of the variation in the original microstructure. Note the exception for the SYN-0.50 microstructures infiltrated at $f = 0.06$, which is attributed to the small number of observations—five subvolumes at each value of f, except four for $f = 0.06$—and the stochastic variability in infiltration.

Overall, the observations in Figure 5.4.1 agree with those of Figure 5.4.2a-b from the last section. Infiltration of LSM into LSM/YSZ/pore backbones generally improves the performance of the existing backbone, primarily by decreasing activation overpotentials or by increasing the effective exchange current densities through increased TPB densities (an increased number of electrochemically active sites). While the effective Ohmic transport improves slightly, i.e., R_{ohm} decreases slightly, a significant signature of the original backbone remains in the infiltrated microstructures. It was shown that the Ohmic contribution is largely dependent on local ionic transport in the YSZ phase [49], and this was a significant source of variability in the backbones themselves. It is likely that local ionic transport was not significantly altered by the infiltration, which is to be expected for infiltration by an electronic conductor if the additional TPB increase adds ionic current uniformly to pre-existing transport paths instead of opening up previously dead or under-utilized paths. For the most part, it appears that additional TPB density is spread out somewhat uniformly, but with some variability around the

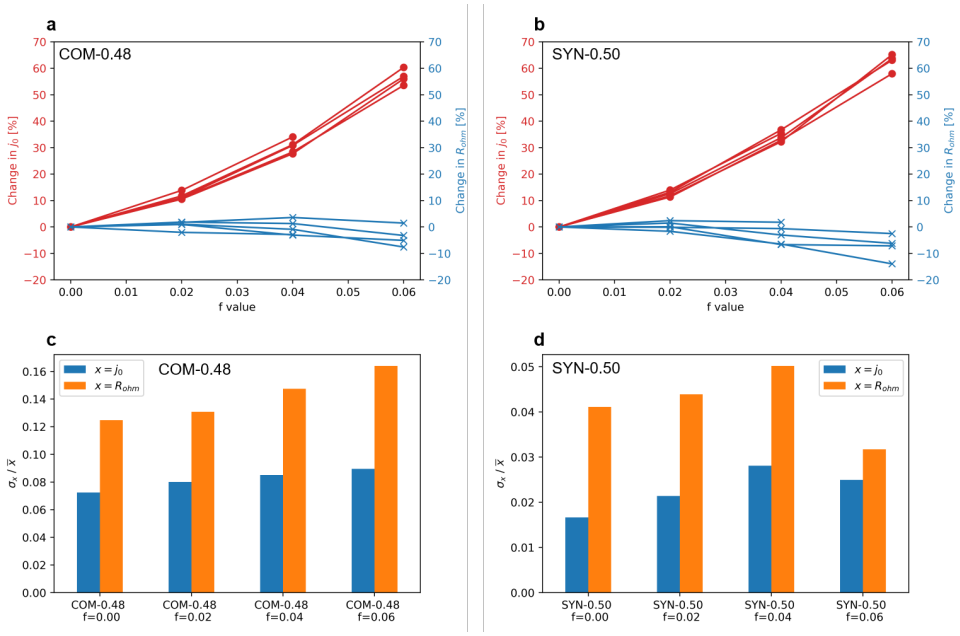

Figure 5.4.2: (a-b) Changes in the effective performance descriptors, j_0 and R_{ohm}, for COM-0.48 and SYN-0.50 upon infiltration. (c-d) Mean-normalized standard deviation of j_0 and R_{ohm} for COM-0.48 and SYN-0.50 upon infiltration.

exact values owing to the stochastic nature of infiltration and the internal variability of backbones. Importantly, infiltration does not lead to converged overall performances across different subvolumes, which one might expect if the original TPB density was poorly distributed with respect to the ionic transport paths.

5.4.3 Local activation overpotentials at TPBs

Thus far, only effective electrochemical quantities have been discussed. Here, at an global overpotential of $\eta = 0.2$ V, the values of local overpotentials at active TPBs (η_{TPB}) are investigated. For ease of visualizing and quantifying local variations of η_{TPB}, 3D fields of η_{TPB} were binned into a uniform grid of $1 \times 1 \times 1$ µm^3 cubic spacing. In each bin, the median value was determined, resulting in a 3D grid of the medians, with the Z axis being the through-thickness direction. Figure 5.4.3 shows the average of these median values at different Z ranges for (a) COM-0.48 and (b) SYN-0.50. The

electrolyte–cathode interface is at Z = 0. It can be seen that η_{TPB} is the highest at the electrolyte–cathode interface and decreases with increasing Z. Further, upon infiltration, local values of η_{TPB} decrease with increasing f. The general shape of the η_{TPB} curves and their magnitudes were previously discussed in [49]. Note that any TPB location, the local activation overpotential and the local ohmic overpotential must sum up to the global overpotential (0.2 V). Thus, an increased ohmic overpotential will suppress the activation overpotential, and vice versa.

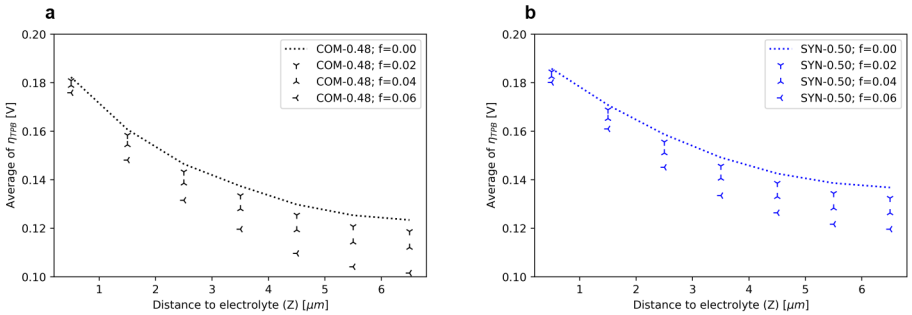

Figure 5.4.3: Average of median values of η_{TPB} along the cathode thickness for (a) COM-0.48 and (b) SYN-0.50. Note that these values are based on a global overpotential of 0.2 V across the simulation domain.

It was already shown in our previous work [49] that an increase in ρ_{TPB} effectively suppresses η_{TPB} at all Z values, primarily because of the increased j values at all Z, which require more Ohmic overpotential to drive the increased current. This is supported by Figure 5.4.3. It can be interpreted that the infiltration increases the TPB density, which increases local current densities and, therefore, the associated local ohmic overpotential at a given TPB. The result is a suppressed distribution of η_{TPB} due to an increased ohmic overpotential. In Figure 5.4.2a-b one sees that the effective (overall) ohmic resistance is mostly unaffected (or slightly decreased) upon infiltration. There it was argued that the decrease may arise from decreased transport paths (on average) for the ionic current. This is consistent with Figure 5.4.3 where, after infiltration and under a fixed global overpotential (0.2 V), the more dense TPB network needs less driving force to deliver increased current values. This continues to build a consistent interpretation of

infiltration in these backbones: that infiltration of LSM increases TPB densities, increases the TPB current density through the cathode, and the ionic current through the same transport pathways that were important prior to infiltration.

5.4.4 Local current density hotspot distributions

In our previous simulation work on these cathode backbones [49], one of the more significant differences in ionic transport between the different types of cathode microstructures was the number density and local volume of current constrictions or hotspots: regions of very high values of local current density in YSZ (j_{YSZ}). To investigate the effect of infiltration on the local hotspots, their distributions were investigated using an identical approach to that in the previous work [49], focusing on the overall number and the number of large volume hotspots. Figure 5.6.3 shows spatial distributions of the local hotspots within a COM-0.48 subvolume as a function of infiltration values f. In any image, the color of a hotspot serves to separate individual hotspots. A cursory visual comparison of the plots at different f values indicates there are very few changes of the hotspot distributions upon infiltration. More careful inspection reveals that, at $f = 0.06$, a few additional small hotspots were formed, although this is not immediately obvious. The same set of observations can be made for SYN-0.50. Figure 5.4.4 shows the number of hotspots for each subvolume (backbone or otherwise infiltrated) as a function of ρ_{TPB}. Figure 5.4.4a plots the number of all hotspots, or all regions whose j_{YSZ} value is more than five standard deviations above the mean value, and Figure 5.4.4b only includes those hotspots whose volumes are bigger than $0.5V_s$, where V_s is the volume of a spherical particle of the mean particle size (0.46 µm). For the backbones themselves, increased homogeneity leads to increased TPB densities and increased (decreased) numbers of total (large) hotspots. It can be seen, however, that the number of total or number of large hotspots were not impacted by the infiltration, despite increased TPB density. Figure 5.6.4 shows the volume distribution of the hotspots in a standard boxplot; the local hotspots were also not impacted with respect to the volume distribution.

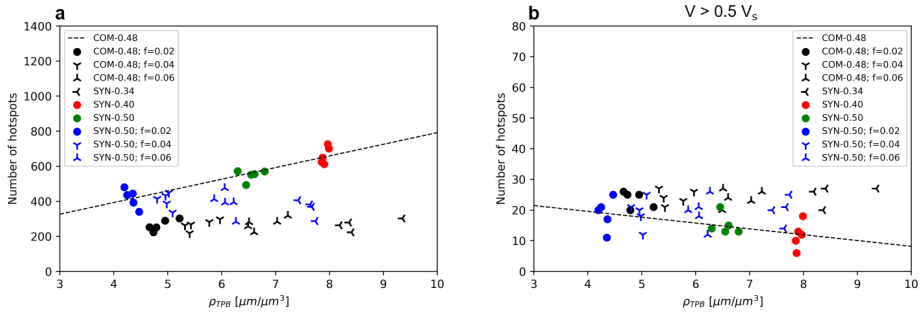

Figure 5.4.4: Number of hotspots plotted against ρ_{TPB} for all subvolumes. The dotted lines are linear fits applied to synthetic backbone microstructures only, (a) Number of all hotspots plotted. (b) Number of larger hotspots ($> 0.5V_s$) plotted.

Since the formation of hotspots is due to local constrictions and local ionic current transport, Figure 5.4.4 suggests that the hotspot distributions, or equivalently the distributions of local ionic current transport, were not influenced by the infiltration. In other words, the ionic current transport remain largely unchanged. This supports the idea that the infiltration primarily influences the activation contribution rather the Ohmic contribution, and that the local distributions of η_{TPB} were more likely to be affected by relative decrease in local electrochemical activities.

5.4.5 Summary Discussion

In this work, we investigated the effects of various loading amounts of electronically conducting infiltrates into LSM/YSZ/pore cathodes, and compared these values to baseline un-infiltrated cells. 50 subvolumes were investigated for statistical and comparison purposes, and 48 led to readily converged solutions to the numerical models simulated. Two major observations were made. First, the primary improvement in performance comes from increased TPB density, lowering the overall activation overpotential owing to the increased number of active sites. Second, the ionic transport paths remain largely unchanged from the backbone, leading to a significant impact of the original microstructure on the performance of the infiltrated microstructures.

Because infiltration increases the TPB density almost by a factor of two,

for $f = 0.06$, it may be a cost-effective method to fabricating a high-performing electrode from a low TPB density electrode backbone, such as the COM-0.48 or SYN-0.50. The question comes down to: is it cheaper to synthesize a highly uniform, monodisperse microstructure, such as SYN-0.34, or to fabricate an infiltrated system upon a heterogeneous backbone, such as SYN-0.50? If one only considers TPB density, the answer to this should be readily determined.

However, a significant signature of the ionic phase in the backbone persists in the infiltrated cathodes, indicating that infiltration does not erase entirely heterogeneities in the microstructure, which may be good or bad for performance. Both the COM-0.48 and SYN-0.50 remain heterogeneous after infiltration, as suggested by the increased standard deviations and constant number of hotspots. This is most clearly seen in the underperformance of the infiltrated COM-0.48 from the average synthetic performance: the infiltration studied here does not render the heterogeneous cathode performance equal to that of the homogeneous synthetic ones, even if the TPB densities approach one another.

Nevertheless, changes do occur within the cathode. Overall the current density increases, indicating larger currents flowing through the microstructure, but generally through the same paths. The increased current density, from increased site populations, requires TPBs to operate at lower activation overpotentials (increased Ohmic overpotentials) to drive the higher total local current density through the cathode YSZ channels. This reduction in local activation overpotential could influence positively local degradation modes, such as chromium poisoning, that are related to local activation overpotentials [67, 92, 122]. Unfortunately, we cannot currently make a one-to-one assignment between microstructure, electrochemistry, and degradation: this work is a step in the direction of achieving this goal.

Finally, the collective discussions thus far provide a key insight into the effect of infiltration on local electrochemistry, and more importantly, microstructure-based cell reliability and durability. The infiltration process clearly improves the overall performance without any significant or negative impacts on local electrochemistry. In fact, the lowered local activities may contribute to a more stable electrochemical load inside the microstructures, and subse-

quently a more durable/reliable performance.

5.5 Conclusions

In this work, a high-throughput, high-performance finite element computation approach was used to simulate electrochemcial performance of SOFC electrodes as a function of microstructural features, focusing on the impact of synthetically generated nano-scale infiltrates of an electron conductor. The simulations retain 3D microstructural morphologies and local materials parameters whilst computing local reaction-transport fluxes of relevant electrochemical species. A total of 48 microstructure subvolumes—the size of each is $10 \times 10 \times 10$ µm (the average particle size is 0.46 µm)—were successfully simulated using 140 cores each on a supercomputer. The 48 subvolumes consist of both experimentally collected and synthetically generated microstructures with a varying degree of microstructural heterogeneity. Analysis of the simulated performance metrics from the model—both on the ensemble level (averaged over subvolumes) and the local level (locally evaluated within subvolumes)–results in the following conclusions.

- For all microstructures, infiltration significantly increases TPB density and improves current density output at a fixed global overpotential.
- Infiltration mainly impacts the activation contribution of the overall performance, through the increased TPB density, and has limited impact on the Ohmic and concentration overpotentials.
- Importantly, the ionic transport paths in the infiltrated cathodes remain nearly identical to those of the initial backbone, indicating that new paths are not opened up via infiltration, but higher current densities flow through the same channels. Thus, underperforming cathodes improve by infiltration, but remain underperforming relative to microstructures having similar TPB density and improved ion flow through YSZ.
- A higher infiltration load is observed to lead to increased scatter in effective performance metrics, suggesting that the stochastic nature of

infiltration adds to the inherent scatter within backbones, and demonstrating that this type of infiltration does not have the effect of converging effective performance of different microstructures.

- The local current density hotspots, which are largely dependent on local ionic current constriction and transport, are unaffected by the infiltration. This supports the idea that the infiltration mostly impacts the activation contribution and not ionic transport.

- Within the microstructure subvolumes, the increased net current densities owing to infiltration lead to higher local Ohmic overpotentials and lower effective activation overpotentials, despite leading to higher overall performance. This observation provides a valuable insight into how the infiltration may alleviate local electrochemical degradation modes while increasing net performance.

5.6 Supplementary Materials

5.6.1 Degree of infiltration loading

As described before, three different levels of infiltrate loading were applied to two sets of microstructures: COM-0.48 and SYN-0.50. The infiltration algorithm takes the value of f (a measure of infiltrate density) as the input and outputs a microstructure volume with synthetically generated nanoscale particles on the solid surfaces. Here the value of f is converted to two physical measures that better represent the extent of the infiltration: decrease in pore volume and increase in solid weight. The change in pore volume was computed simply by accounting for the number of voxels that became the infiltrate phase, while the change in solid weight was computed by assuming an LSM density of 6.5 $\mathrm{g\,cm^{-3}}$. Figure 5.6.1 shows these values as a function of f.

For the COM-0.48 microstructures, the average decrease (increase) in pore volume (solid weight) from the uninfiltrated microstructures was 3.2 , 6.1, and 8.5 % (2.3, 4.0, and 4.7 %) for f = 0.02, 0.04, and 0.06, respectively. For the COM-0.50 microstructures, the average decrease (increase) in pore

volume (solid weight) from the uninfiltrated microstructures was 3.8, 7.5, and 10.1 % (2.4, 3.9, and 4.8 %) for $f = 0.02$, 0.04, and 0.06, respectively. Note that the values for the solid weight changes are similar, since this reflects the infiltrate weight. The pore volume changes slightly less for the COM-0.48, because the original pore volume is larger. Also, as the infiltration value f increases, the slope begins to decrease for both values (but more-so for the solid weight increase). This arises as an outcome of nuclei overlapping in the synthetic infiltration algorithm.

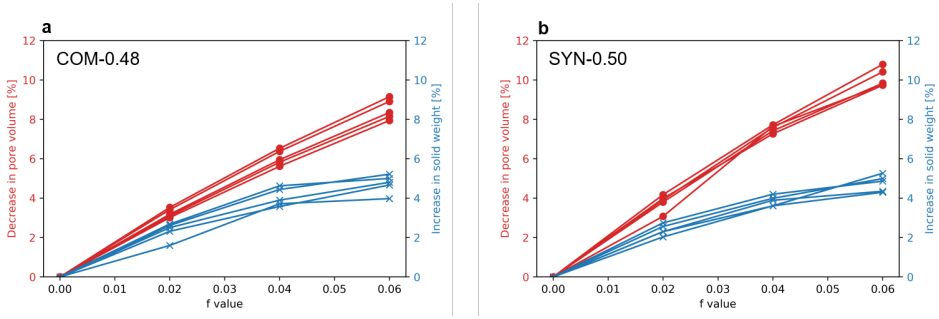

Figure 5.6.1: Degree of infiltration loading as represented by the decrease in pore volume (red curves) and increase in solid weight (blue curves) for (a) COM-0.48 and (b) SYN-0.50.

5.6.2 Effective overpotential-current density plots

For each of the 48 converged simulations, the global (effective) current density (j) is plotted across the input range of overpotential (η = 0–0.4 V), as shown in Figure 5.6.2. (a) only contains un-infiltrated microstructures plotted as thin lines, (b) only contains COM-0.48 data, and (c) only contains SYN-0.50 data. The markers represent the infiltrated subvolumes. Color indicates microstructure type. The curves of the original, un-infiltrated subvolumes are consistent with the results of our previous study [49] (these were all simulated again, for consistency sake). Note that the shape of these curves indicate the overpotentials consist primarily of activation and Ohmic contributions, without a significant concentration contribution (which is verified through the observation that the local concentrations do not vary significantly from the input values). Overall, improved performance curves are observed for the infiltrated subvolumes.

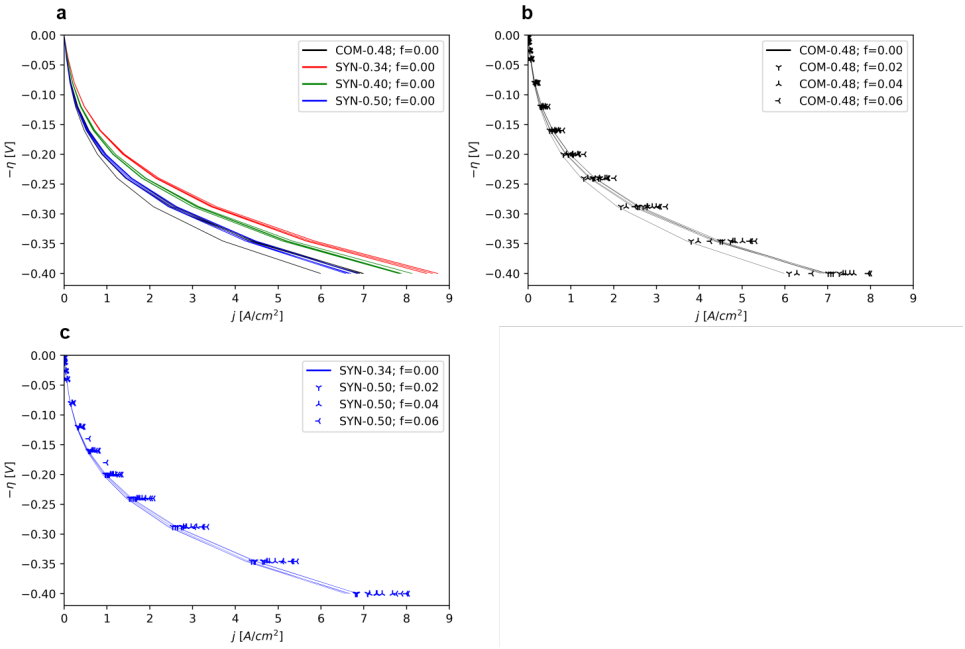

Figure 5.6.2: Effective η-j curve plots for all 48 converged subvolumes. For ease of visualization, (a) only contains un-infiltrated mirostructures, (b) only contains COM-0.48 data, and (c) only contains SYN-0.50 data. Thin lines represent original, un-infiltrated microstructures, while markers represent infiltrated ones. Color indicates microstructure type.

5.6.3 Spatial distributions of local hotspots

Figure 5.6.3 shows the spatial distributions of local hotspots for one COM-0.48 at different infiltration loads. Color indicates invidual hotspots, and is arbitrarily assigned. The primary observation to be made is that there are very little differences in the hotspot shapes and spatial distributions with infiltration, besides the difference in color (owing to the arbitary assignments). With more careful inspection, it can be seen that high values of f result in additional smaller hotspots, hotspots similar to the small hotspots observed in the highly active backbones.

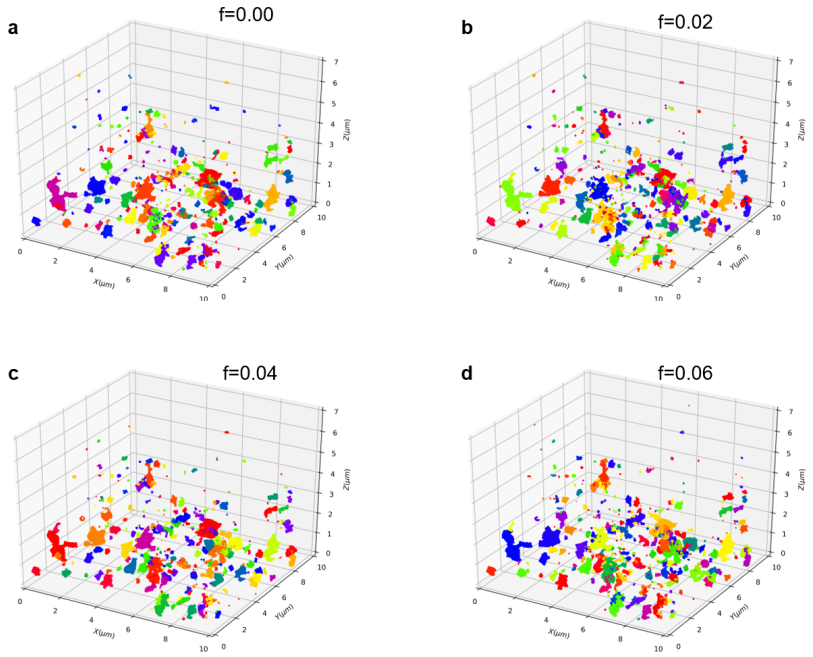

Figure 5.6.3: Spatial distributions of local hotspots for one COM-0.48 subvolume that is (a) un-infiltrated, and infiltrated at $f = 0.02,\ 0.04,\ 0.06$ for (b), (c), and (d), respectively. Color indicates individual hotspots.

5.6.4 Hotspot volume distributions

Combining all the hotspots for the COM-0.48 and SYN-0.50 subvolumes, the volume distributions of the hotspots are plotted against the value of f in the standard boxplot, as shown in Figure 5.6.4. Note that the y axis is in log scale, and any small changes in the log scale are much smaller in the absolute scale. Infiltration does not lead to significant changes on hotspot volumes in terms of the mean, the interquartile range (IQR), or the outlier distributions, for either backbone.

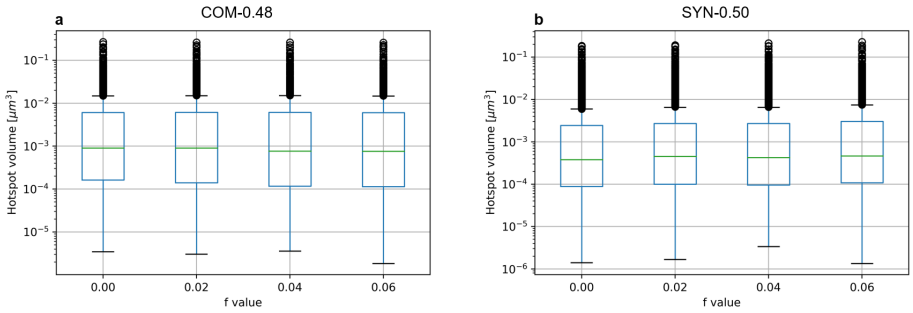

Figure 5.6.4: Standard boxplots of the hotspot volume distributions plotted against the value of f. The box represents the interquartile range (IQR), and the outliers are circle markers whose values are greater than $Q_3 + 1.5\text{IQR}$ or less than $Q_3 - 1.5\text{IQR}$, where $Q1$ is the first quartile, and $Q3$ is the third quartile.

6

Overall Conclusions and Future Work

This thesis embodies a comprehensive methodology for an end-to-end, sample-to-simulation workflow that characterizes, reconstructs, processes, meshes, and finally simulates electrochemistry (reaction and transport) within solid oxide fuel cell (SOFC) electrode microstructures. An emphasis is placed on reconstructing high-definition, locally-resolved complex microstructures over large scales and applying high-performance, high-throughput simulations to extract a large amount of performance data that reflects statistical trends and/or significance. The long-term goal relative to SOFCs is to develop an understanding between local microstructure and performance that will inform future investigations of cell reliability and durability, and will aid process engineers improve such performance measures. The scope of the current work first demonstrates the plausibility of carrying out such work, and then uses preliminary analysis techniques and findings to gain insight into how microstructural heterogeneities directly impact both local and global performance.

The main motivation for emphasizing large-scale reconstructions and high

performance computing (HPC) platforms is to move forward from current conventional computational approaches, which are overly limited with respect to total volume and complexity of physics for relevant SOFC simulations. Many of the works in the literature have not utilized large-scale characterization or high performance computations. Further, many such works have only considered effective medium theory (EMT) models that compute the ensemble/effective performance metrics averaged over a given microstructure subvolume. In doing so, valuable information regarding local performance quantities is lost. These quantities (e.g., local current density constrictions) have been shown to significantly influence the ensemble performance. Thus, to understand cell durability and reliability on a higher level, one must consider that the microstructure dictates local performance/degradation, which in turn dictates ensemble performance/degradation. Naturally, capturing distributions of local performance quantities over large-scale microstructure volumes (for statistical significance) necessitates high performance resources.

The model/workflow developed herein has the following characteristics:

- High-resolution, large-scale microstructure acquisition
- Straightforward image-based volumetric meshing that conforms to complex, multi-phased microstructures
- Computation of local electrochemical fields in morphology-resolved microstructures at considerable length scales
- Modular nature of user-defined physics; addition or modification of physics requires minimal programming effort
- Implementation on HPC platforms, leading to fast, high-throughput computations

Such characteristics allow for flexible modification or addition of physics codes, portability between different HPC platforms (for larger scaling), and opportunities to generalize and simulate other microstructurally complex energy device materials. There are many possibilities for the future work.

For example, one can apply or append degradation models into the current model architecture to correlate microstructure with local degradation. Adding thermal conduction to investigate thermally-driven microstructural evolution/failure is also another promising future direction.

In the first publishable study of this work, ERMINE (the name of the model developed in this work) was used to explore the effect of microstructural heterogeneity on local and global performance metrics. This work was novel because of the computational power and the amount of datasets utilized relative to the current literature. A total of 47 subvolumes of meshed three-phase cathode microstructures were simulated. Each subvolume is at considerable length scale and was computed with > 100 cores on a supercomputer. Additionally, both experimentally characterized and synthetically generated microstructures were used that consist of a range of heterogeneity. The conclusions from the study are as follows:

- The average performance simulated from the locally-resolved model compares favorably to the EMT models, indicating the local physics are accurately captured.
- The largest discrepancy between the locally-resolved simulations and the EMT models arises from the local ionic (Ohmic) transport in the YSZ phase of the active cathode. Analysis of local activation overpotential at TPB sites and local current density in YSZ reinforce this.
- Constriction of local current density was shown by the locally-resolved simulations to be widespread in all microstructures, but this is not accounted for by either EMT model. Thus, high-throughput locally-resolved simulations offer a path to informing/improving the accuracy of EMT models.
- The ability of the locally-resolved model to compute fields of activation overpotentials and current density hotspots demonstrates the potential for using locally-resolved simulations to better inform models of local degradation mechanisms.
- The distinctive heterogeneity of the commercial cathode, previously captured as variations in local volume fractions, clearly impacts the

electrochemical properties simulated by the locally-resolved models; the commercial microstructure results in distinctive distributions of (1) effective voltage-current performance output, (2) local activation overpotentials at TPB sites, and (3) local current densities in YSZ.

- The distinctive distributions of local electrochemical quantities contribute unfavorably to the ionic transport terms, resulting in the commercial microstructure having the worst overall performance relative to the synthetic microstructures, despite not having the lowest values of TPB density.

- Many of these findings can be attributed to the high-performance, high-throughput nature of the presented computational approach, allowing locally-resolved simulations of many microstructural volumes, with each having large enough size to compute accurate local properties. Such methods offer a large-data, statistical approach to understanding fuel cell performance characteristics, which will underpin the development of high-durability, high-reliability electrochemical cells.

As a final demonstration and exploration of SOFC microstructure-performance relationship, the effects of infiltration on local/global performance metrics were investigated using ERMINE. This was the first time local electrochemistry of synthetically generated nanoscale infiltration was modeled in a complex microstructure. Similar to the previous study, a combination of experimentally captured and synthetic microstructures was used to constitute of range of heterogeneity. A total of 47 subvolumes—infiltrated or not—were simulated for meaningful statistical observation. These subvolumes originated from the converged sets in the study described above. The conclusions from the work are as follows:

- For all microstructures, infiltration significantly increases TPB density and improves current density output at a fixed global overpotential.

- Infiltration mainly impacts the activation contribution of the overall performance, through the increased TPB density, and has limited impact on the Ohmic and concentration overpotentials.

- Importantly, the ionic transport paths in the infiltrated cathodes remain nearly identical to those of the initial backbone, indicating that new paths are not opened up via infiltration, but higher current densities flow through the same channels. Thus, underperforming cathodes improve by infiltration, but remain underperforming relative to microstructures having similar TPB density and improved ion flow through YSZ.

- A higher infiltration load is observed to lead to increased scatter in effective performance metrics, suggesting that the stochastic nature of infiltration adds to the inherent scatter within backbones, and demonstrating that this type of infiltration does not have the effect of converging effective performance of different microstructures.

- The local current density hotspots, which are largely dependent on local ionic current constriction and transport, are unaffected by the infiltration. This supports the idea that the infiltration mostly impacts the activation contribution and not ionic transport.

- Within the microstructure subvolumes, the increased net current densities owing to infiltration lead to higher local Ohmic overpotentials and lower effective activation overpotentials, despite leading to higher overall performance. This observation provides a valuable insight into how the infiltration may alleviate local electrochemical degradation modes while increasing net performance.

Together, these studies demonstrate that ERMINE shows great promise for providing insight and observations that are not possible in current effective medium theory approaches, which are limited in accounting for locally varying electrochemical quantities. The findings of both aforementioned studies are mainly attributed to the high-performance computational approach that enables a robust statistical inspection of the simulation data. However, this work has not fully explored some of the more statistically advanced and rigorous models that can potentially benefit greatly from the massive amounts of data that can be generated from this work. Methodologically, ERMINE is only the beginning for how future SOFC studies should

conduct investigations into microstructure-driven performance/failure metrics. To further the understanding of cell durability and reliability with respect to electrode microstructures, ERMINE offers many possibilities for future work due to the flexible and automated nature of the established workflow. One may introduce degradation physics into the current existing model, convert material properties for an entirely different cathode composition, or even scale up current simulation production for massive data generation and advanced statistical analysis.

A

ERMINE Source Codes

A.1 The Input File

The input files, which can be found under `/inputs` of the ERMINE directory, control all necessary simulation options on the highest level. These options include the path of the mesh file, the physics to be simulated, model parameters, the type of the numerical solver, output format, etc. The input file itself is passed as an option for the command that runs parallel processes using ERMINE's compiled executable. For example, the following command instantiates an MPI parallel process with `input_file.i` on 32 cores:

```
mpiexec --n 32 ./executable -i input_file.i
```

Below is an example of an input file that instantiates the ERMINE model:

```
[Mesh]
  file = meshes/micro/russiandoll/s4/MSRI_CAT_box10_shrink4.inp
[]

[MeshModifiers]
  [./meshScale]
```

```
    type = Transform
    transform = SCALE
    vector_value = '1e-4 1e-4 1e-4' # from um to cm
  [../]

  [./phase_12_interface]
    type = SideSetsBetweenSubdomains
    depends_on = meshScale
    master_block = 'PT_MASK_1_TET4'
    paired_block = 'PT_MASK_2_TET4'
    new_boundary = 'interface_12'
  [../]
  [./phase_21_interface]
    type = SideSetsBetweenSubdomains
    depends_on = meshScale
    master_block = 'PT_MASK_2_TET4'
    paired_block = 'PT_MASK_1_TET4'
    new_boundary = 'interface_21'
  [../]

  [./phase_23_interface]
    type = SideSetsBetweenSubdomains
    depends_on = meshScale
    master_block = 'PT_MASK_2_TET4'
    paired_block = 'PT_MASK_3_TET4'
    new_boundary = 'interface_23'
  [../]

  [./phase_32_interface]
    type = SideSetsBetweenSubdomains
    depends_on = meshScale
    master_block = 'PT_MASK_3_TET4'
    paired_block = 'PT_MASK_2_TET4'
    new_boundary = 'interface_32'
  [../]
[]

#============================================================#

[GlobalParams]
# E_rev   = 1.028   # (V)
```

```
# phi_LSM = 0.928   # (V)
  pO2_CE  = 1e-20   # (atm)
[../]

[Functions]
  [./funcPotentialLSM]
    type = ParsedFunction
    value = 'E_rev - eta*t'
    vars = 'E_rev eta'
    vals = '1.028 0.4'
  [../]
[]

[Materials]
  # PT_MASK_1_TET4 = pore
  # PT_MASK_2_TET4 = LSM
  # PT_MASK_3_TET4 = YSZ
  # PT_MASK_4_TET4 = TPB
  [./gasDiffFluxCoefficient]
    type  = ParsedMaterial
    block = 'PT_MASK_1_TET4 PT_MASK_4_TET4'
    f_name = 'gasDiffFluxCoef'
    constant_names        = 'D_O2  R          T'        # (cm^2/s)
    , (J/K/mol), (K)
    constant_expressions  = '0.64  8.3144598  1073.0'
    function = 'D_O2/R/T*101325'
  [../]

  [./vacancyDiffFluxCoefficient]
    type  = ParsedMaterial
    block = 'PT_MASK_2_TET4 PT_MASK_4_TET4'
    f_name = 'vacDiffFluxCoef'
    constant_names        = 'D_O      a         NA'     # (cm^2/s)
    , (cm), (1/mol), .
    constant_expressions  = '7.5e-7   3.893e-8  6.022e23'
    function = 'D_O/(a^3)/NA*1e6'
  [../]

  [./vacancyDriftFluxCoefficient]
    type  = GenericConstantMaterial
    block = 'PT_MASK_3_TET4 PT_MASK_4_TET4'
```

```
    prop_names  = 'sigma_YSZ' # (S/cm)
    prop_values = '4e-2'
  [../]
[]

#============================================================#

[Variables]
  [./p_O2]
    block = 'PT_MASK_1_TET4 PT_MASK_4_TET4'
    initial_condition = 0.21 # (atm)
    scaling = 1e5
  [../]

  [./V_O]
    block = 'PT_MASK_2_TET4 PT_MASK_4_TET4'
    initial_condition = 2.580947226225166e-08 # (.) pO2 = 0.21 atm
    scaling = 1e8
  [../]

  [./phi_YSZ]
    block = 'PT_MASK_3_TET4 PT_MASK_4_TET4'
    initial_condition = -0.00000 # (V)
    scaling = 1e7
  [../]
[]

#============================================================#

[Kernels]
  [./gasDiffusion]
    type  = DiffMatKernel
    block = 'PT_MASK_1_TET4 PT_MASK_4_TET4'
    variable  = p_O2
    diff_coef = 'gasDiffFluxCoef'
  [../]

  [./vacancyDiffusion]
    type  = DiffMatKernel
    block = 'PT_MASK_2_TET4 PT_MASK_4_TET4'
    variable  = V_O
```

```
    diff_coef = 'vacDiffFluxCoef'
  [../]

  [./vacancyIonicDrift]
    type  = DiffMatKernel
    block = 'PT_MASK_3_TET4 PT_MASK_4_TET4'
    variable  = phi_YSZ
    diff_coef = 'sigma_YSZ'
  [../]

  [./tpbReactionOxygenPore]
    type = CoupledTPBOxygenPressurePoreQS
    block = 'PT_MASK_4_TET4'
    variable = p_O2
    phi_YSZ = phi_YSZ
    s0 = 136 # (A/cm^3) (6.8 * 20)
    function_phi_LSM = 'funcPotentialLSM'
  [../]

  [./tpbReactionPotentialYSZ]
    type = CoupledTPBPotentialYSZQS
    block = 'PT_MASK_4_TET4'
    variable = phi_YSZ
    p_O2 = p_O2
    s0 = 136 # (A/cm^3) (6.8 * 20)
    function_phi_LSM = 'funcPotentialLSM'
  [../]
[]

#============================================================#

[InterfaceKernels]
  [./interfaceSurfaceExchangeFullyCoupled]
    type = InterfaceSurfExchangeFullyCoupled
    variable = p_O2
    neighbor_var = V_O
    boundary = 'interface_12'
    k = 6.14e-6 # (cm/s)
  [../]

  [./interfaceChargeTransferFullyCoupled]
```

```
    type = InterfaceChargeTransferFullyCoupledQS
    variable = V_O
    neighbor_var = phi_YSZ
    boundary = 'interface_23'
    j0 = 0.193  # (A/cm^2)
    function_phi_LSM = 'funcPotentialLSM'
  [../]
[]

#============================================================#

[BCs]
  [./oxygenPartialPressure_top]
    type = DirichletBC
    variable = p_O2
    boundary = 'SF_MASK_1_WITH_ZMIN'
    value = 0.21 # (atm)
  [../]

  [./potentialYSZ_bottom]
    type = DirichletBC
    variable = phi_YSZ
    boundary = 'SF_MASK_3_WITH_ZMAX'
    value = 0.00000 # (V)
  [../]
[]

#============================================================#

[AuxVariables]
  [./aux_pO2_LSM]
    block = 'PT_MASK_2_TET4 PT_MASK_4_TET4'
  [../]

  [./aux_Erev_LSM]
    block = 'PT_MASK_2_TET4 PT_MASK_4_TET4'
  [../]

  #[./aux_phi_YSZ_gradNorm]
  #  block = 'PT_MASK_4_TET4'
  #  order = CONSTANT
```

```
  #  family = MONOMIAL
  #[../]
[]

[AuxKernels]
  [./pO2_LSM]
    type = ParsedAux
    variable = aux_pO2_LSM
    block = 'PT_MASK_2_TET4 PT_MASK_4_TET4'
    function = '10^(-2.173913*log10(V_O) - 17.173913)'
    args = 'V_O'
  [../]

  [./Erev_LSM]
    type = ParsedAux
    variable = aux_Erev_LSM
    block = 'PT_MASK_2_TET4 PT_MASK_4_TET4'
    function = '-R*T/4/F * log(1e-20 / aux_pO2_LSM)'
    constant_names = 'R T F'
    constant_expressions = '8.3144598 1073 96485.33289' # (J/K/mol
    ), (K), (C/mol)
    args = 'aux_pO2_LSM'
  [../]

  #[./phi_YSZ_gradNorm]
  #  type = VariableGradientNorm
  #  block = 'PT_MASK_4_TET4'
  #  variable = aux_phi_YSZ_gradNorm
  #  gradient_variable = 'phi_YSZ'
  #[../]
[]

#============================================================#

[Postprocessors]
  [./I_YSZ_bottom]
    type = SideFluxIntegral
    variable = phi_YSZ
    diffusivity = 'sigma_YSZ'
    boundary = 'SF_MASK_3_WITH_ZMAX'
    outputs = 'console csv'
```

```
  [../]

  [./j_YSZ_bottom]
    type = SideFluxAverage
    variable = phi_YSZ
    diffusivity = 'sigma_YSZ'
    boundary = 'SF_MASK_3_WITH_ZMAX'
    outputs = 'console csv'
  [../]

  [./phi_LSM]
    type = FunctionValuePostprocessor
    function = 'funcPotentialLSM'
    outputs = 'console csv'
  [../]
[]

#============================================================#

[Preconditioning]
  [./smp]
    type = SMP
    full = true
    petsc_options = '-snes_converged_reason -ksp_converged_reason'
  [../]
[]

#============================================================#

[Executioner]
  type = Transient
  start_time = 0.0
  end_time = 1.0
  dtmin = 1e-4
  nl_rel_tol = 1e-7
  nl_abs_tol = 1e-10
  l_tol = 1e-04
  l_max_its = 2000
  [./TimeStepper]
    type = FunctionDT
    time_t =  '0.0  0.1 0.5 1.0'
```

```
    time_dt = '0.01 0.1 0.1 0.2'
  [../]
  solve_type = 'NEWTON'
  #petsc_options_iname = '-pc_type -pc_hypre_type'
  #petsc_options_value = 'hypre boomeramg'
  petsc_options_iname = '-ksp_gmres_restart -pc_type'
  petsc_options_value = '100 bjacobi'
[]

#============================================================#

[Outputs]
  exodus = true
  csv = true
  file_base = outputs/micro/russiandoll/s4/MSRI_CAT_box10_shrink4
  append_date = true
  append_date_format = '%Y-%m-%d'
  #print_perf_log = true
[]

[Debug]
  show_var_residual_norms = true
[]
```

A.2 The Kernels

In the MOOSE framework, a *kernel* generally refers to a mathematical term, or an operator, that operates on variables in a partial differential equation (PDE). In other words, a kernel may be considered as a piece of physics. In some cases, it may be favorable to use a kernel to represent multiple operators or terms in a PDE. Since MOOSE is an objected-orientated environment, all kernels (as well as all other objects) are written as C++ classes that inherit from parent classes already defined within the framework. In other words, users who wish to add their own physics may simply create custom kernels to construct the PDEs; but they need to follow a set of rules inherited from parent classes in order to interface with MOOSE and the core libraries (PETSc and libMesh).

The source codes for the physics discussed in the second chapter, particularly the surface exchange, the charge transfer, and the TPB reaction, are shown here. No custom kernels were necessary for the bulk transports, since they all follow a common diffusion-type operator, as shown in

$$\nabla \cdot (D \nabla u), \tag{A.1}$$

that one would expect from a continuity equation. This diffusion-type operator is readily available in the MOOSE framework.

A.2.1 The Surface Exchange Kernel

```
#include "InterfaceSurfExchangeFullyCoupled.h"
#include <cmath>

template<>
InputParameters validParams<InterfaceSurfExchangeFullyCoupled>()
{
  InputParameters params = validParams<InterfaceKernel>();
  params.addClassDescription("InterfaceKernel that sets the flux
    of u as J = k * (neighbor_value_inf - neighbor_value)");
  params.addRequiredParam<Real>("k","Exchange coefficient (cm/s)")
    ;
  params.addParam<Real>("R", 8.3144598, "Gas constant (J/K/mol)");
```

```
  params.addParam<Real>("T", 1073.0, "Temperature (T)");
  return params;
}

InterfaceSurfExchangeFullyCoupled::
    InterfaceSurfExchangeFullyCoupled(const InputParameters &
    parameters) :
    InterfaceKernel(parameters),
    _k(getParam<Real>("k")),
    _R(getParam<Real>("R")),
    _T(getParam<Real>("T"))
{
  if (!parameters.isParamValid("boundary"))
  {
    mooseError("In order to use the InterfaceSurfExchange dgkernel
    , you must specify a boundary where it will live.");
  }
}

Real
InterfaceSurfExchangeFullyCoupled::computeQpResidual(Moose::
    DGResidualType type)
{
  Real a    = 3.893e-8;   // LSM unit cell edge lenth (cm)
  Real NA   = 6.022e23;   // Avogadro number (1/mol)
  Real logP = log10(_u[_qp]);
  Real logV = -0.46*logP - 7.9;
  Real V_p  = pow(10.0,logV);

  Real res = 1e6 / pow(a,3.0) / NA * _k * (_neighbor_value[_qp] -
    V_p);

  switch (type)
  {
    case Moose::Element:
      res *= 0.5 * _test[_i][_qp];        // flux outwards of
    phase1
      break;

    case Moose::Neighbor:
      res *= _test_neighbor[_i][_qp];    // flux inwards into
```

```
    phase2
      break;
  }

  return res;
}

Real
InterfaceSurfExchangeFullyCoupled::computeQpJacobian(Moose::
    DGJacobianType type)
{
  Real a    = 3.893e-8;   // LSM unit cell edge lenth (cm)
  Real NA   = 6.022e23;   // Avogadro number (1/mol)
  Real logP = log10(_u[_qp]);
  Real logV = -0.46*logP - 7.9;

  Real logV_prime = -0.46;

  Real jac = 0.0;

  switch (type)
  {
    case Moose::ElementElement:
      jac = -1e6 / pow(a,3.0) / NA * _k * pow(10,logV) *
    logV_prime / _u[_qp]
            * 0.5 * _test[_i][_qp] * _phi[_j][_qp];

    case Moose::ElementNeighbor:
      jac = 1e6 / pow(a,3.0) / NA * _k
            * 0.5 * _test[_i][_qp] * _phi_neighbor[_j][_qp];
      break;

    case Moose::NeighborNeighbor:
      jac = 1e6 / pow(a,3.0) / NA * _k
            * _test_neighbor[_i][_qp] * _phi_neighbor[_j][_qp];
      break;

    case Moose::NeighborElement:
      jac = -1e6 / pow(a,3.0) / NA * _k * pow(10,logV) *
    logV_prime / _u[_qp]
            * _test_neighbor[_i][_qp] * _phi[_j][_qp];
```

```
83          break;
84      }
85
86      return jac;
87  }
```

A.2.2 The Charge Transfer Kernel

```
#include "InterfaceChargeTransferFullyCoupledQS.h"
#include "Function.h"
#include <cmath>

template<>
InputParameters validParams<InterfaceChargeTransferFullyCoupledQS
    >()
{
  InputParameters params = validParams<InterfaceKernel>();
  params.addClassDescription("InterfaceKernel that sets the charge
     transfer flux as j = 2 * j0 * sinh(0.5 * beta * eta_ct).
    Master block is phase2 (LSM)");
  params.addRequiredParam<Real>("j0", "Charge transfer exchange
    current density (A/cm^2)");
  params.addParam<Real>("z", 4.0, "electron number (num of
    electrons transferred)");
  params.addParam<Real>("F", 96485.33289, "Faraday constant (C/mol
    )");
  params.addParam<Real>("R", 8.3144598, "Gas constant (J/K/mol)");
  params.addParam<Real>("T", 1073.0, "Temperature (T)");
  params.addRequiredParam<FunctionName>("function_phi_LSM", "
    Function for the LSM potential");
  params.addRequiredParam<Real>("pO2_CE", "Oxygen Partial Pressure
     at the Counter Electrode (atm)");
  return params;
}

InterfaceChargeTransferFullyCoupledQS::
    InterfaceChargeTransferFullyCoupledQS(const InputParameters &
    parameters) :
    InterfaceKernel(parameters),
    _j0(getParam<Real>("j0")),
    _z(getParam<Real>("z")),
    _F(getParam<Real>("F")),
    _R(getParam<Real>("R")),
    _T(getParam<Real>("T")),
    _func_phi_LSM(getFunction("function_phi_LSM")),
    _pO2_CE(getParam<Real>("pO2_CE"))
{
```

```
30   if (!parameters.isParamValid("boundary"))
31   {
32     mooseError("In order to use the InterfaceChargeTransfer
       dgkernel, you must specify a boundary where it will live.");
33   }
34 }
35
36 Real
37 InterfaceChargeTransferFullyCoupledQS::computeQpResidual(Moose::
       DGResidualType type)
38 {
39   Real b    = _z * _F / _R / _T;
40   Real logV = log10(_u[_qp]);
41   Real logP = -2.173913*logV - 17.173913;
42   Real pO2  = pow(10.0,logP);
43   Real E_conc = - _R * _T / _z / _F * log(_pO2_CE / pO2);
44   Real phi_LSM = _func_phi_LSM.value(_t, _q_point[_qp]);
45   Real eta_ct = E_conc - (phi_LSM - _neighbor_value[_qp]);
46
47   Real res  = 2.0 * _j0 * sinh(0.5*b*eta_ct);
48
49   switch (type)
50   {
51     case Moose::Element:
52       res *= -1e6 / _z / _F * _test[_i][_qp];   // vacancy flux
       inwards of phase2 (master)
53       break;
54
55     case Moose::Neighbor:
56       res *= _test_neighbor[_i][_qp];           // electric flux
       outwards of phase3 (paired)
57       break;
58   }
59
60   return res;
61 }
62
63 Real
64 InterfaceChargeTransferFullyCoupledQS::computeQpJacobian(Moose::
       DGJacobianType type)
65 {
```

```
  Real b    = _z * _F / _R / _T;
  Real logV = log10(_u[_qp]);
  Real logP = -2.173913*logV - 17.173913;
  Real pO2  = pow(10.0,logP);
  Real E_conc = - _R * _T / _z / _F * log(_pO2_CE / pO2);
  Real phi_LSM = _func_phi_LSM.value(_t, _q_point[_qp]);
  Real eta_ct = E_conc - (phi_LSM - _neighbor_value[_qp]);

  Real logP_prime = -2.173913;

  Real jac = 0.0;

  switch (type)
  {
    case Moose::ElementElement:
      jac = _j0 * cosh(0.5*b*eta_ct) * logP_prime / _u[_qp]
            * -1e6 / _z / _F * _phi[_j][_qp] * _test[_i][_qp];
      break;

    case Moose::ElementNeighbor:
      jac = b * _j0 * cosh(0.5*b*eta_ct)
            * -1e6 / _z / _F * _phi_neighbor[_j][_qp] * _test[_i][
    _qp];
      break;

    case Moose::NeighborNeighbor:
      jac = b * _j0 * cosh(0.5*b*eta_ct)
            * _phi_neighbor[_j][_qp] * _test_neighbor[_i][_qp];
      break;

    case Moose::NeighborElement:
      jac = _j0 * cosh(0.5*b*eta_ct) * logP_prime / _u[_qp]
            * _phi[_j][_qp] * _test_neighbor[_i][_qp];
      break;
  }

  return jac;
}
```

A.2.3 The TPB Reaction Kernel

```
#include "CoupledTPBOxygenPressurePoreQS.h"
#include "Function.h"
#include <cmath>


template<>
InputParameters validParams<CoupledTPBOxygenPressurePoreQS>()
{
  InputParameters params = validParams<Kernel>();
  params.addClassDescription("Fully Coupled TPB reaction source kernel in sinh() form for oxygen concentration in pore. j = 2 * j0 * sinh(coef * eta)");
  params.addRequiredParam<Real>("s0", "Exchange volumetric current density rate (A/cm^3)");
  params.addParam<Real>("z", 4.0, "electron number (num of electrons transferred)");
  params.addParam<Real>("F", 96485.33289, "Faraday constant (C/mol)");
  params.addParam<Real>("R", 8.3144598, "Gas constant (J/K/mol)");
  params.addParam<Real>("T", 1073.0, "Temperature (T)");
  params.addRequiredParam<FunctionName>("function_phi_LSM", "Function for the LSM potential");
  params.addRequiredParam<Real>("pO2_CE", "Oxygen partial pressure at the counter electrode (atm)");
  params.addRequiredCoupledVar("phi_YSZ", "The coupled potential variable in eta = potential_rev - (phi_LSM - phi_YSZ)");
  return params;
}

CoupledTPBOxygenPressurePoreQS::CoupledTPBOxygenPressurePoreQS(
    const InputParameters & parameters) :
    Kernel(parameters),
    _s0(getParam<Real>("s0")),
    _z(getParam<Real>("z")),
    _F(getParam<Real>("F")),
    _R(getParam<Real>("R")),
    _T(getParam<Real>("T")),
    _func_phi_LSM(getFunction("function_phi_LSM")),
    _pO2_CE(getParam<Real>("pO2_CE")),
```

```
    _num_phi_YSZ(coupled("phi_YSZ")),
    _phi_YSZ(coupledValue("phi_YSZ"))
{
}

Real
CoupledTPBOxygenPressurePoreQS::computeQpResidual()
{
  Real b    = _z * _F / _R / _T;
  Real E_conc = - _R * _T / _z / _F * log(_pO2_CE / _u[_qp]);
  Real phi_LSM = _func_phi_LSM.value(_t, _q_point[_qp]);
  Real eta  = E_conc - (phi_LSM - _phi_YSZ[_qp]);

  Real res  = 1e6 / _z / _F * 2 * _s0 * sinh(0.5 * b * eta);

  return  res * _test[_i][_qp];
}

Real
CoupledTPBOxygenPressurePoreQS::computeQpJacobian()
{
  Real b    = _z * _F / _R / _T;
  Real E_conc = - _R * _T / _z / _F * log(_pO2_CE / _u[_qp]);
  Real phi_LSM = _func_phi_LSM.value(_t, _q_point[_qp]);
  Real eta  = E_conc - (phi_LSM - _phi_YSZ[_qp]);

  Real jac  = 1e6 / _z / _F * _s0 * cosh(0.5 * b * eta) / _u[_qp];

  return jac * _test[_i][_qp] * _phi[_j][_qp];
}

Real
CoupledTPBOxygenPressurePoreQS::computeQpOffDiagJacobian(unsigned
    int jvar)
{
  Real b    = _z * _F / _R / _T;
  Real E_conc = - _R * _T / _z / _F * log(_pO2_CE / _u[_qp]);
  Real phi_LSM = _func_phi_LSM.value(_t, _q_point[_qp]);
  Real eta  = E_conc - (phi_LSM - _phi_YSZ[_qp]);

  Real jac  = 1e6 / _z / _F * b * _s0 * cosh(0.5 * b * eta);
```

```
71
72   if (jvar == _num_phi_YSZ)
73     return jac * _test[_i][_qp] * _phi[_j][_qp];
74   else return 0.0;
75 }
```

References

[1] S. B. Adler, J. Lane, and B. Steele. Electrode kinetics of porous mixed-conducting oxygen electrodes. *Journal of the Electrochemical Society*, 143(11):3554–3564, 1996.

[2] A. Atkinson, S. Barnett, R. J. Gorte, J. Irvine, A. J. McEvoy, M. Mogensen, S. C. Singhal, and J. Vohs. Advanced anodes for high-temperature fuel cells. *Nature materials*, 3(1):17–27, 2004.

[3] A. Belzner, T. M. Gür, and R. A. Huggins. Oxygen chemical diffusion in strontium doped lanthanum manganites. *Solid State Ionics*, 57(3-4): 327–337, 1992.

[4] A. Bertei, V. Yufit, F. Tariq, and N. Brandon. A novel approach for the quantification of inhomogeneous 3d current distribution in fuel cell electrodes. *Journal of Power Sources*, 396:246–256, 2018.

[5] R. B. Bird, J. O. Hirschfelder, and C. F. Curtiss. *Molecular theory of gases and liquids*. John Wiley, 1954.

[6] Q. Cai, C. S. Adjiman, and N. P. Brandon. Investigation of the active thickness of solid oxide fuel cell electrodes using a 3d microstructure model. *Electrochimica Acta*, 56(28):10809–10819, 2011.

[7] Q. Cai, C. S. Adjiman, and N. P. Brandon. Modelling the 3d microstructure and performance of solid oxide fuel cell electrodes: computational parameters. *Electrochimica Acta*, 56(16):5804–5814, 2011.

[8] T. Carraro, J. Joos, B. Rüger, A. Weber, and E. Ivers-Tiffée. 3d finite element model for reconstructed mixed-conducting cathodes: I. performance quantification. *Electrochimica Acta*, 77:315–323, 2012.

[9] T. Carraro, J. Joos, B. Rüger, A. Weber, and E. Ivers-Tiffée. 3d finite element model for reconstructed mixed-conducting cathodes: Ii. parameter sensitivity analysis. *Electrochimica Acta*, 77:309–314, 2012.

[10] S. Chan, X. Chen, and K. Khor. Cathode micromodel of solid oxide fuel cell. *Journal of the Electrochemical Society*, 151(1):A164–A172, 2004.

[11] C.-C. Chao, M. Motoyama, and F. B. Prinz. Nanostructured platinum catalysts by atomic-layer deposition for solid-oxide fuel cells. *Advanced Energy Materials*, 2(6):651–654, 2012.

[12] X. Chen, S. Chan, and K. Khor. Simulation of a composite cathode in solid oxide fuel cells. *Electrochimica Acta*, 49(11):1851–1861, 2004.

[13] Y.-c. K. Chen-Wiegart, J. S. Cronin, Q. Yuan, K. J. Yakal-Kremski, S. A. Barnett, and J. Wang. 3d non-destructive morphological analysis of a solid oxide fuel cell anode using full-field x-ray nano-tomography. *Journal of Power Sources*, 218:348–351, 2012.

[14] S. Choi, S. Yoo, J.-Y. Shin, and G. Kim. High performance sofc cathode prepared by infiltration of la n+ 1ni n o3 n+ 1 (n= 1, 2, and 3) in porous ysz. *Journal of the Electrochemical Society*, 158(8):B995–B999, 2011.

[15] G. W. Coffey, L. R. Pederson, and P. C. Rieke. Competition between bulk and surface pathways in mixed ionic electronic conducting oxygen electrodes. *Journal of the Electrochemical Society*, 150(8):A1139–A1151, 2003.

[16] J. S. Cronin, J. R. Wilson, and S. A. Barnett. Impact of pore microstructure evolution on polarization resistance of ni-yttria-stabilized zirconia fuel cell anodes. *Journal of Power Sources*, 196(5):2640–2643, 2011.

[17] J. S. Cronin, K. Muangnapoh, Z. Patterson, K. J. Yakal-Kremski, V. P. Dravid, and S. A. Barnett. Effect of firing temperature on lsm-ysz composite cathodes: a combined three-dimensional microstructure and impedance spectroscopy study. *Journal of the Electrochemical Society*, 159(4):B385–B393, 2012.

[18] J. S. Cronin, Y.-c. K. Chen-Wiegart, J. Wang, and S. A. Barnett. Three-dimensional reconstruction and analysis of an entire solid oxide fuel cell by full-field transmission x-ray microscopy. *Journal of Power Sources*, 233:174–179, 2013.

[19] R. E. Cunningham and R. Williams. *Diffusion in gases and porous media*, volume 1. Springer, 1980.

[20] E. L. Cussler. *Diffusion: mass transfer in fluid systems*. Cambridge university press, 2009.

[21] J. Deseure, Y. Bultel, L. Dessemond, E. Siebert, and P. Ozil. Modelling the porous cathode of a sofc: oxygen reduction mechanism effect. *Journal of applied electrochemistry*, 37(1):129–136, 2007.

[22] S. J. Dillon, L. Helmick, H. M. Miller, L. Wilson, R. Gemman, R. V. Petrova, K. Barmak, G. S. Rohrer, and P. A. Salvador. The orientation distributions of lines, surfaces, and interfaces around three-phase boundaries in solid oxide fuel cell cathodes. *Journal of the American Ceramic Society*, 94(11):4045–4051, 2011.

[23] K. Eguchi, N. Kamiuchi, J.-Y. Kim, H. Muroyama, T. Matsui, M. Kishimoto, M. Saito, H. Iwai, H. Yoshida, N. Shikazono, et al. Microstructural change of ni–gdc cermet anode in the electrolyte-supported disk-type sofc upon daily start-up and shout-down operations. *Fuel Cells*, 12(4):537–542, 2012.

[24] N. Epstein. On tortuosity and the tortuosity factor in flow and diffusion through porous media. *Chemical engineering science*, 44(3):777–779, 1989.

[25] W. K. Epting, J. Gelb, and S. Litster. Resolving the three-dimensional microstructure of polymer electrolyte fuel cell electrodes using nanometer-scale x-ray computed tomography. *Advanced Functional Materials*, 22(3):555–560, 2012.

[26] W. K. Epting, Z. Mansley, D. B. Menasche, P. Kenesei, R. M. Suter, K. Gerdes, S. Litster, and P. A. Salvador. Quantifying intermediate-frequency heterogeneities of sofc electrodes using x-ray computed tomography. *Journal of the American Ceramic Society*, 100(5):2232–2242, 2017.

[27] M. Ester, H.-P. Kriegel, J. Sander, X. Xu, et al. A density-based algorithm for discovering clusters in large spatial databases with noise. In *Kdd*, volume 96, pages 226–231, 1996.

[28] Y. Fan, X. Song, H. Abernathy, Y. Chen, R. Pineault, J. Liu, K. Gerdes, S. Lee, T. Kalapos, and G. A. Hackett. Long term performance stability tests of ba-fe-o infiltrated lsm/ysz solid oxide fuel cells under high steam and high current. *ECS Transactions*, 78(1): 1003–1010, 2017.

[29] Y. Fan, Y. Chen, H. Abernathy, R. Pineault, X. Song, J. Liu, K. Gerdes, S. Lee, T. Yang, T. Kalapos, et al. Improved long term performance stability of sr-fe-o infiltrated lsm/ysz solid oxide fuel cells under high steam and high temperature. *ECS Transactions*, 85(13): 1277–1287, 2018.

[30] J. Fleig. On the width of the electrochemically active region in mixed conducting solid oxide fuel cell cathodes. *Journal of Power Sources*, 105(2):228–238, 2002.

[31] S. Gamble. Fabrication–microstructure–performance relationships of reversible solid oxide fuel cell electrodes–review. *Materials Science and Technology*, 27(10):1485–1497, 2011.

[32] J. Gao, Y. Meng, S. Lee, J. Tong, and K. S. Brinkman. Effect of infiltration of barium carbonate nanoparticles on the electrochemical performance of la 0.6 sr 0.4 co 0.2 fe 0.8 o 3- δ cathodes for protonic ceramic fuel cells. *JOM*, 71(1):90–95, 2019.

[33] D. Gaston, C. Newman, G. Hansen, and D. Lebrun-Grandie. Moose: A parallel computational framework for coupled systems of nonlinear equations. *Nuclear Engineering and Design*, 239(10):1768–1778, 2009.

[34] D. R. Gaston, C. J. Permann, J. W. Peterson, A. E. Slaughter, D. Andrš, Y. Wang, M. P. Short, D. M. Perez, M. R. Tonks, J. Ortensi, et al. Physics-based multiscale coupling for full core nuclear reactor simulation. *Annals of Nuclear Energy*, 84:45–54, 2015.

[35] C. Geuzaine and J.-F. Remacle. Gmsh: A 3-d finite element mesh generator with built-in pre-and post-processing facilities. *International Journal for Numerical Methods in Engineering*, 79(11):1309–1331, 2009.

[36] M. Gong, R. S. Gemmen, and X. Liu. Modeling of oxygen reduction mechanism for 3pb and 2pb pathways at solid oxide fuel cell cathode from multi-step charge transfer. *Journal of Power Sources*, 201:204–218, 2012.

[37] D. Gostovic, J. Smith, D. Kundinger, K. Jones, and E. Wachsman. Three-dimensional reconstruction of porous lscf cathodes. *Electrochemical and solid-state letters*, 10(12):B214–B217, 2007.

[38] K. N. Grew, Y. S. Chu, J. Yi, A. A. Peracchio, J. R. Izzo, Y. Hwu, F. De Carlo, and W. K. Chiu. Nondestructive nanoscale 3d elemental

mapping and analysis of a solid oxide fuel cell anode. *Journal of the Electrochemical Society*, 157(6):B783–B792, 2010.

[39] M. Groeber, S. Ghosh, M. D. Uchic, and D. M. Dimiduk. A framework for automated analysis and simulation of 3d polycrystalline microstructures. part 2: Synthetic structure generation. *Acta Materialia*, 56(6): 1274–1287, 2008.

[40] Y. Guan, W. Li, Y. Gong, G. Liu, X. Zhang, J. Chen, J. Gelb, W. Yun, Y. Xiong, Y. Tian, et al. Analysis of the three-dimensional microstructure of a solid-oxide fuel cell anode using nano x-ray tomography. *Journal of Power Sources*, 196(4):1915–1919, 2011.

[41] Y. Guan, Y. Gong, G. Liu, X. Song, X. Zhang, Y. Xiong, H. Wang, and Y. Tian. Analysis of impact of sintering time on microstructure of lsm-ysz composite cathodes by x-ray nanotomography. *Materials Express*, 3(2):166–170, 2013.

[42] A. Häffelin, J. Joos, M. Ender, A. Weber, and E. Ivers-Tiffée. Time-dependent 3d impedance model of mixed-conducting solid oxide fuel cell cathodes. *Journal of The Electrochemical Society*, 160(8):F867–F876, 2013.

[43] W. M. Harris and W. K. Chiu. Determining the representative volume element size for three-dimensional microstructural material characterization. part 1: Predictive models. *Journal of Power Sources*, 282: 552–561, 2015.

[44] W. M. Harris and W. K. Chiu. Determining the representative volume element size for three-dimensional microstructural material characterization. part 2: Application to experimental data. *Journal of Power Sources*, 282:622–629, 2015.

[45] J. O. Hirschfelder, R. B. Bird, and E. L. Spotz. The transport properties of gases and gaseous mixtures. ii. *Chemical Reviews*, 44(1): 205–231, 1949.

[46] L. Holzer, D. Wiedenmann, B. Münch, L. Keller, M. Prestat, P. Gasser, I. Robertson, and B. Grobéty. The influence of constrictivity on the effective transport properties of porous layers in electrolysis and fuel cells. *Journal of materials science*, 48(7):2934–2952, 2013.

[47] T. Hsu, R. Mahbub, W. K. Epting, H. Abernathy, G. A. Hackett, A. D. Rollett, S. Litster, and P. A. Salvador. Towards quantification of local

electrochemical parameters in microstructures of solid oxide fuel cell electrodes using high performance computations. *ECS Transactions*, 78(1):2711–2722, 2017.

[48] T. Hsu, W. K. Epting, R. Mahbub, N. T. Nuhfer, S. Bhattacharya, Y. Lei, H. M. Miller, P. R. Ohodnicki, K. R. Gerdes, H. W. Abernathy, et al. Mesoscale characterization of local property distributions in heterogeneous electrodes. *Journal of Power Sources*, 386:1–9, 2018.

[49] T. Hsu, J. H. Mason, R. Mahbub, W. K. Epting, H. W. Abernathy, G. A. Hackett, A. D. Rollett, S. Litster, and P. A. Salvador. High performance computation of local electrochemistry in heterogeneous microstructures of solid oxide fuel cells. *In preparation*, 2019.

[50] H. J. Hwang, J.-W. Moon, S. Lee, and E. A. Lee. Electrochemical performance of lscf-based composite cathodes for intermediate temperature sofcs. *Journal of Power Sources*, 145(2):243–248, 2005.

[51] H. Iwai, N. Shikazono, T. Matsui, H. Teshima, M. Kishimoto, R. Kishida, D. Hayashi, K. Matsuzaki, D. Kanno, M. Saito, et al. Quantification of sofc anode microstructure based on dual beam fib-sem technique. *Journal of Power Sources*, 195(4):955–961, 2010.

[52] Y. Ji, J. Kilner, and M. Carolan. Electrical properties and oxygen diffusion in yttria-stabilised zirconia (ysz)–la 0.8 sr 0.2 mno 3± (lsm) composites. *Solid State Ionics*, 176(9):937–943, 2005.

[53] S. P. Jiang. Nanoscale and nano-structured electrodes of solid oxide fuel cells by infiltration: advances and challenges. *International journal of hydrogen energy*, 37(1):449–470, 2012.

[54] Z. Jiao, N. Shikazono, and N. Kasagi. Quantitative characterization of sofc nickel-ysz anode microstructure degradation based on focused-ion-beam 3d-reconstruction technique. *Journal of The Electrochemical Society*, 159(3):B285–B291, 2012.

[55] Z. Jiao, T. Shimura, and N. Shikazono. Numerical assessment of sofc anode polarization with microstructure evolution. *ECS Transactions*, 68(1):1281–1289, 2015.

[56] J. Joos, T. Carraro, A. Weber, and E. Ivers-Tiffée. Reconstruction of porous electrodes by fib/sem for detailed microstructure modeling. *Journal of Power Sources*, 196(17):7302–7307, 2011.

[57] J. Joos, M. Ender, T. Carraro, A. Weber, and E. Ivers-Tiffée. Representative volume element size for accurate solid oxide fuel cell cathode reconstructions from focused ion beam tomography data. *Electrochimica Acta*, 82:268–276, 2012.

[58] P. S. Jørgensen, K. Yakal-Kremski, J. Wilson, J. R. Bowen, and S. Barnett. On the accuracy of triple phase boundary lengths calculated from tomographic image data. *Journal of Power Sources*, 261:198–205, 2014.

[59] P. S. Jørgensen, S. L. Ebbehøj, and A. Hauch. Triple phase boundary specific pathway analysis for quantitative characterization of solid oxide cell electrode microstructure. *Journal of Power Sources*, 279: 686–693, 2015.

[60] V. Julie, L. Jérôme, C. Peter, B. Pierre, D. Gérard, S. Heikki, and U.-V. François. 3d phase mapping of solid oxide fuel cell ysz/ni cermet at the nanoscale by holographic x-ray nanotomography. *Journal of Power Sources*, 243:841–849, 2013.

[61] D. Kanno, N. Shikazono, N. Takagi, K. Matsuzaki, and N. Kasagi. Evaluation of sofc anode polarization simulation using three-dimensional microstructures reconstructed by fib tomography. *Electrochimica Acta*, 56(11):4015–4021, 2011.

[62] B. Kenney, M. Valdmanis, C. Baker, J. Pharoah, and K. Karan. Computation of tpb length, surface area and pore size from numerical reconstruction of composite solid oxide fuel cell electrodes. *Journal of Power Sources*, 189(2):1051–1059, 2009.

[63] M. Kishimoto, H. Iwai, M. Saito, and H. Yoshida. Quantitative evaluation of solid oxide fuel cell porous anode microstructure based on focused ion beam and scanning electron microscope technique and prediction of anode overpotentials. *Journal of Power Sources*, 196(10): 4555–4563, 2011.

[64] M. Kishimoto, H. Iwai, M. Saito, and H. Yoshida. Three-dimensional simulation of sofc anode polarization characteristics based on sub-grid scale modeling of microstructure. *Journal of The Electrochemical Society*, 159(3):B315–B323, 2012.

[65] M. Kishimoto, K. Miyawaki, H. Iwai, M. Saito, and H. Yoshida. Effect of composition ratio of ni-ysz anode on distribution of effective three-phase boundary and power generation performance. *Fuel Cells*, 13(4): 476–486, 2013.

[66] T. Klemensø, K. Thydén, M. Chen, and H.-J. Wang. Stability of ni–yttria stabilized zirconia anodes based on ni-impregnation. *Journal of Power Sources*, 195(21):7295–7301, 2010.

[67] M. Krumpelt, T. A. Cruse, B. J. Ingram, J. L. Routbort, S. Wang, P. A. Salvador, and G. Chen. The Effect of Chromium Oxyhydroxide on Solid Oxide Fuel Cells. *Journal of The Electrochemical Society*, 157(2):B228, 2010. ISSN 00134651. doi: 10.1149/1.3266930. URL http://jes.ecsdl.org/cgi/doi/10.1149/1.3266930.

[68] M. Krumpelt, T. A. Cruse, B. J. Ingram, J. L. Routbort, S. Wang, P. A. Salvador, and G. Chen. The effect of chromium oxyhydroxide on solid oxide fuel cells. *Journal of The Electrochemical Society*, 157 (2):B228–B233, 2010.

[69] J. Laurencin, R. Quey, G. Delette, H. Suhonen, P. Cloetens, and P. Bleuet. Characterisation of solid oxide fuel cell ni–8ysz substrate by synchrotron x-ray nano-tomography: from 3d reconstruction to microstructure quantification. *Journal of Power Sources*, 198:182–189, 2012.

[70] S. Lee and K. Gerdes. Functional nanostructure engineering of sofc cathode by solution infiltration. *ECS Electrochemistry Letters*, 4(3): F17–F20, 2015.

[71] S. Lee, M. Bevilacqua, P. Fornasiero, J. Vohs, and R. Gorte. Solid oxide fuel cell cathodes prepared by infiltration of lani0. 6fe0. 4o3 and la0. 91sr0. 09ni0. 6fe0. 4o3 in porous yttria-stabilized zirconia. *Journal of Power Sources*, 193(2):747–753, 2009.

[72] S. Lee, N. Miller, H. Abernathy, K. Gerdes, and A. Manivannan. Effect of sr-doped lacoo3 and lazro3 infiltration on the performance of sdc-lscf cathode. *Journal of the Electrochemical Society*, 158(6):B735–B742, 2011.

[73] S. Lee, N. Miller, M. Staruch, K. Gerdes, M. Jain, and A. Manivannan. Pr0. 6sr0. 4coo3- δ electrocatalyst for solid oxide fuel cell cathode introduced via infiltration. *Electrochimica Acta*, 56(27):9904–9909, 2011.

[74] S. Lee, N. Miller, and K. Gerdes. Long-term stability of sofc composite cathode activated by electrocatalyst infiltration. *Journal of the Electrochemical Society*, 159(7):F301–F308, 2012.

[75] Y. Leng, S. H. Chan, and Q. Liu. Development of lscf–gdc composite cathodes for low-temperature solid oxide fuel cells with thin film gdc electrolyte. *International Journal of Hydrogen Energy*, 33(14):3808–3817, 2008.

[76] L. Liang, Q. Li, J. Hu, S. Lee, K. Gerdes, and L.-Q. Chen. Phase field modeling of microstructure evolution of electrocatalyst-infiltrated solid oxide fuel cell cathodes. *Journal of Applied Physics*, 117(6):065105, 2015.

[77] S. Litster, W. Epting, E. Wargo, S. Kalidindi, and E. Kumbur. Morphological analyses of polymer electrolyte fuel cell electrodes with nano-scale computed tomography imaging. *Fuel Cells*, 13(5):935–945, 2013.

[78] M. Liu, D. Ding, K. Blinn, X. Li, L. Nie, and M. Liu. Enhanced performance of lscf cathode through surface modification. *international journal of hydrogen energy*, 37(10):8613–8620, 2012.

[79] X. Liu, H. Wu, Z. He, J. Gao, X. Meng, T. Luo, C. Chen, and Z. Zhan. Hebb-wagner polarization assessment of enhanced oxygen permeability for surface modified oxygen transport membranes. *International Journal of Hydrogen Energy*, 42(29):18410–18416, 2017.

[80] Y.-L. Liu, A. Hagen, R. Barfod, M. Chen, H.-J. Wang, F. W. Poulsen, and P. V. Hendriksen. Microstructural studies on degradation of interface between lsm–ysz cathode and ysz electrolyte in sofcs. *Solid State Ionics*, 180(23):1298–1304, 2009.

[81] M. E. Lynch, D. Ding, W. M. Harris, J. J. Lombardo, G. J. Nelson, W. K. Chiu, and M. Liu. Flexible multiphysics simulation of porous electrodes: Conformal to 3d reconstructed microstructures. *Nano Energy*, 2(1):105–115, 2013.

[82] R. Mahbub, T. Hsu, W. K. Epting, N. T. Nuhfer, G. A. Hackett, H. Abernathy, A. D. Rollett, M. De Graef, S. Litster, and P. A. Salvador. A method for quantitative 3d mesoscale analysis of solid oxide fuel cell microstructures using xe-plasma focused ion beam (pfib) coupled with sem. *ECS Transactions*, 78(1):2159–2170, 2017.

[83] R. Mahbub, T. Hsu, W. K. Epting, N. T. Nuhfer, G. A. Hackett, H. Abernathy, A. D. Rollett, M. De Graef, S. Litster, and P. A. Salvador. A method for quantitative 3d mesoscale analysis of solid oxide

fuel cellmicrostructures using xe-plasma focused ion beam (pfib) coupled with sem. *ECS Transactions*, 2017(in press).

[84] J. Maier. *Physical chemistry of ionic materials: ions and electrons in solids*. John Wiley & Sons, 2004.

[85] J. Mason, I. Celik, S. Lee, H. Abernathy, and G. Hackett. Performance degradation predictions based on microstructural evolution due to grain coarsening effects in solid oxide fuel cell electrodes. *Journal of The Electrochemical Society*, 165(2):F64–F74, 2018.

[86] J. H. Mason, I. B. Celik, H. Abernathy, and G. A. Hackett. Modified butler-volmer type model which accounts for triple and double phase boundary reaction pathways. *ECS Transactions*, 78(1):2855–2864, 2017.

[87] T. Matsui, R. Kishida, J.-Y. Kim, H. Muroyama, and K. Eguchi. Performance deterioration of ni–ysz anode induced by electrochemically generated steam in solid oxide fuel cells. *Journal of The Electrochemical Society*, 157(5):B776–B781, 2010.

[88] T. Matsui, J.-Y. Kim, H. Muroyama, M. Shimazu, T. Abe, M. Miyao, and K. Eguchi. Anode microstructural change upon long-term operation for the cathode-supported tubular-type sofc. *Solid State Ionics*, 225:50–54, 2012.

[89] K. Matsuzaki, N. Shikazono, and N. Kasagi. Three-dimensional numerical analysis of mixed ionic and electronic conducting cathode reconstructed by focused ion beam scanning electron microscope. *Journal of Power Sources*, 196(6):3073–3082, 2011.

[90] C. Metcalfe, O. Kesler, T. Rivard, F. Gitzhofer, and N. Abatzoglou. Connected three-phase boundary length evaluation in modeled sintered composite solid oxide fuel cell electrodes. *Journal of the Electrochemical Society*, 157(9):B1326–B1335, 2010.

[91] N. Q. Minh and T. Takahashi. *Science and technology of ceramic fuel cells*. Elsevier, 1995.

[92] K. Miyoshi, H. Iwai, M. Kishimoto, M. Saito, and H. Yoshida. Chromium poisoning in (La,Sr)MnO3 cathode: Three-dimensional simulation of a solid oxide fuel cell. *Journal of Power Sources*, 326: 331–340, 2016. ISSN 03787753. doi: 10.1016/j.jpowsour.2016.06.110. URL http://dx.doi.org/10.1016/j.jpowsour.2016.06.110.

[93] K. Miyoshi, T. Miyamae, H. Iwai, M. Saito, M. Kishimoto, and H. Yoshida. Exchange current model for (la 0.8 sr 0.2) 0.95 mno 3 (lsm) porous cathode for solid oxide fuel cells. *Journal of Power Sources*, 315:63–69, 2016.

[94] A. Nakajo, A. Cocco, M. DeGostin, A. Peracchio, B. Cassenti, M. Cantoni, W. Chiu, et al. Accessible triple-phase boundary length: A performance metric to account for transport pathways in heterogeneous electrochemical materials. *Journal of Power Sources*, 325:786–800, 2016.

[95] G. J. Nelson, W. M. Harris, J. J. Lombardo, J. R. Izzo, W. K. Chiu, P. Tanasini, M. Cantoni, C. Comninellis, J. C. Andrews, Y. Liu, et al. Comparison of sofc cathode microstructure quantified using x-ray nanotomography and focused ion beam–scanning electron microscopy. *Electrochemistry Communications*, 13(6):586–589, 2011.

[96] G. J. Nelson, K. N. Grew, J. R. Izzo, J. J. Lombardo, W. M. Harris, A. Faes, A. Hessler-Wyser, S. Wang, Y. S. Chu, A. V. Virkar, et al. Three-dimensional microstructural changes in the ni–ysz solid oxide fuel cell anode during operation. *Acta Materialia*, 60(8):3491–3500, 2012.

[97] M. Ni, M. K. Leung, and D. Y. Leung. Micro-scale modelling of solid oxide fuel cells with micro-structurally graded electrodes. *Journal of Power Sources*, 168(2):369–378, 2007.

[98] N. A. Nystrom, M. J. Levine, R. Z. Roskies, and J. R. Scott. Bridges: A uniquely flexible hpc resource for new communities and data analytics. In *Proceedings of the 2015 XSEDE Conference: Scientific Advancements Enabled by Enhanced Cyberinfrastructure*, XSEDE '15, pages 30:1–30:8, New York, NY, USA, 2015. ACM. ISBN 978-1-4503-3720-5. doi: 10.1145/2792745.2792775. URL http://doi.acm.org/10.1145/2792745.2792775.

[99] R. P. O'Hayre, S.-W. Cha, W. Colella, and F. B. Prinz. *Fuel cell fundamentals*. John Wiley & Sons New York, 2006.

[100] S. Pakalapati, K. Gerdes, H. Finklea, M. Gong, X. Liu, and I. Celik. Micro scale dynamic modeling of lsm/ysz composite cathodes. *Solid State Ionics*, 258:45–60, 2014.

[101] H. Parikh, N. Hilli, M. R. De Guire, A. H. Heuer, Z. Liu, and R. Goettler. Long-term microstructural changes in solid oxide fuel cell anodes:

3d reconstruction. *Journal of the American Ceramic Society*, 100(4): 1653–1660, 2017.

[102] T. Poulet, M. Paesold, and M. Veveakis. Multi-physics modelling of fault mechanics using redback: a parallel open-source simulator for tightly coupled problems. *Rock Mechanics and Rock Engineering*, 3 (50):733–749, 2016.

[103] F. W. Poulsen. Defect chemistry modelling of oxygen-stoichiometry, vacancy concentrations, and conductivity of (la 1− x sr x) y mno 3± . *Solid State Ionics*, 129(1):145–162, 2000.

[104] T. Prokop, K. Berent, J. Szmyd, and G. Brus. A three-dimensional numerical assessment of heterogeneity impact on a solid oxide fuel cell's anode performance. *Catalysts*, 8(11):503, 2018.

[105] B. Rüger, A. Weber, and E. Ivers-Tiffee. 3d-modelling and performance evaluation of mixed conducting (miec) cathodes. *ECS Transactions*, 7(1):2065–2074, 2007.

[106] B. Rüger, J. Joos, A. Weber, T. Carraro, and E. Ivers-Tiffée. 3d electrode microstructure reconstruction and modelling. *ECS Transactions*, 25(2):1211–1220, 2009.

[107] Y. Shao-Horn et al. Oxygen surface exchange kinetics on sr-substituted lanthanum manganite and ferrite thin-film microelectrodes. *Journal of The Electrochemical Society*, 156(7):B816–B824, 2009.

[108] P. Shearing, Q. Cai, J. Golbert, V. Yufit, C. Adjiman, and N. Brandon. Microstructural analysis of a solid oxide fuel cell anode using focused ion beam techniques coupled with electrochemical simulation. *Journal of Power Sources*, 195(15):4804–4810, 2010.

[109] P. Shearing, J. Gelb, J. Yi, W.-K. Lee, M. Drakopolous, and N. Brandon. Analysis of triple phase contact in ni–ysz microstructures using non-destructive x-ray tomography with synchrotron radiation. *Electrochemistry Communications*, 12(8):1021–1024, 2010.

[110] P. R. Shearing, J. Gelb, and N. Brandon. Characterization of sofc electrode microstructure using nano-scale x-ray computed tomography and focused ion beam techniques: a comparative study. *ECS Transactions*, 19(17):51–57, 2009.

[111] N. Shikazono, D. Kanno, K. Matsuzaki, H. Teshima, S. Sumino, and N. Kasagi. Numerical assessment of sofc anode polarization based on three-dimensional model microstructure reconstructed from fib-sem images. *Journal of The Electrochemical Society*, 157(5):B665–B672, 2010.

[112] F. Si, G. Zhang, and K. Huang. Communication—improving intermediate-temperature performance of a screen-printed lscf cathode with infiltrated lscf nanoparticles. *Journal of The Electrochemical Society*, 163(7):F626–F628, 2016.

[113] A. M. Svensson, S. Sunde, and K. Nisşancioğlu. Mathematical modeling of oxygen exchange and transport in air-perovskite-ysz interface regions i. reduction of intermediately adsorbed oxygen. *Journal of The Electrochemical Society*, 144(8):2719–2732, 1997.

[114] A. M. Svensson, S. Sunde, K. Nis, et al. Mathematical modeling of oxygen exchange and transport in air-perovskite-yttria-stabilized zirconia interface regions ii. direct exchange of oxygen vacancies. *Journal of the Electrochemical Society*, 145(4):1390–1400, 1998.

[115] C. W. Tanner, K.-Z. Fung, and A. V. Virkar. The effect of porous composite electrode structure on solid oxide fuel cell performance i. theoretical analysis. *Journal of The Electrochemical Society*, 144(1): 21–30, 1997.

[116] E. technical services. Fuel cell handbook. Technical report, U.S. Department of Energy, Office of Fossil Energy, National Energy Technology Laboratory, 2004.

[117] A. Tkachuk, F. Duewer, H. Cui, M. Feser, S. Wang, and W. Yun. X-ray computed tomography in zernike phase contrast mode at 8 kev with 50-nm resolution using cu rotating anode x-ray source. *Zeitschrift für Kristallographie-Crystalline Materials*, 222(11/2007):650–655, 2007.

[118] N. Vivet, S. Chupin, E. Estrade, T. Piquero, P. Pommier, D. Rochais, and E. Bruneton. 3d microstructural characterization of a solid oxide fuel cell anode reconstructed by focused ion beam tomography. *Journal of Power Sources*, 196(18):7541–7549, 2011.

[119] J. M. Vohs and R. J. Gorte. High-performance sofc cathodes prepared by infiltration. *Advanced Materials*, 21(9):943–956, 2009.

[120] J. Wang, Z. Zhou, W. Zhang, T. M. Garoni, and Y. Deng. Bond and site percolation in three dimensions. *Physical Review E*, 87(5):052107, 2013.

[121] S. Wang, T. Cruse, M. Krumpelt, B. Ingram, and P. Salvador. Microstructural degradation of (la, sr) mno3/ ysz cathodes in solid oxide fuel cells with uncoated e-brite interconnects. *Journal of The Electrochemical Society*, 158(2):B152–B158, 2011.

[122] S. Wang, T. A. Cruse, M. Krumpelt, B. J. Ingram, and P. A. Salvador. Microstructural Degradation of (La,Sr)MnO[sub 3]/YSZ Cathodes in Solid Oxide Fuel Cells with Uncoated E-Brite Interconnects. *Journal of The Electrochemical Society*, 158(2):B152, 2011. ISSN 00134651. doi: 10.1149/1.3515073. URL http://jes.ecsdl.org/cgi/doi/10.1149/1.3515073.

[123] J. R. Wilson, W. Kobsiriphat, R. Mendoza, H.-Y. Chen, J. M. Hiller, D. J. Miller, K. Thornton, P. W. Voorhees, S. B. Adler, and S. A. Barnett. Three-dimensional reconstruction of a solid-oxide fuel-cell anode. *Nature materials*, 5(7):541–544, 2006.

[124] J. R. Wilson, A. T. Duong, M. Gameiro, H.-Y. Chen, K. Thornton, D. R. Mumm, and S. A. Barnett. Quantitative three-dimensional microstructure of a solid oxide fuel cell cathode. *Electrochemistry Communications*, 11(5):1052–1056, 2009.

[125] J. R. Wilson, J. S. Cronin, A. T. Duong, S. Rukes, H.-Y. Chen, K. Thornton, D. R. Mumm, and S. Barnett. Effect of composition of (la 0.8 sr 0.2 mno 3–y 2 o 3-stabilized zro 2) cathodes: Correlating three-dimensional microstructure and polarization resistance. *Journal of Power Sources*, 195(7):1829–1840, 2010.

[126] J. R. Wilson, J. S. Cronin, and S. A. Barnett. Linking the microstructure, performance and durability of ni-yttria-stabilized zirconia solid oxide fuel cell anodes using three-dimensional focused ion beam–scanning electron microscopy imaging. *Scripta Materialia*, 65 (2):67–72, 2011.

[127] L. Yan, B. Kavaipatti, K.-C. Chang, H. You, and P. Salvador. Microstructural effects on the oxygen exchange kinetics of la0. 7sr0. 3mno3 thin films. *ECS Transactions*, 35(1):2063–2075, 2011.

[128] T. Yang, I. B. Celik, H. Sezer, S. Lee, and K. Gerdes. Investigation of infiltration via multi-physics simulation tool with realistic microstructure properties. *ECS Transactions*, 66(2):137–142, 2015.

[129] T. Yang, S. Lee, W. Li, Y. Lin, J. Liu, X. Liu, H. Abernathy, and G. A. Hackett. Combined experimental and numerical analysis of surface-modified solid oxide fuel cell cathodes. *ECS Transactions*, 85(13): 1289–1305, 2018.

[130] T. Yang, J. Liu, H. Finklea, S. Lee, W. K. Epting, R. Mahbub, T. Hsu, P. A. Salvador, H. W. Abernathy, and G. A. Hackett. An efficient approach for prediction of warburg-type resistance under working currents. *International Journal of Hydrogen Energy*, 43(32):15445–15456, 2018.

[131] Y. Yi, A. D. Rao, J. Brouwer, and G. S. Samuelsen. Fuel flexibility study of an integrated 25kw sofc reformer system. *Journal of Power Sources*, 144(1):67–76, 2005.

[132] H. Yokokawa, H. Tu, B. Iwanschitz, and A. Mai. Fundamental mechanisms limiting solid oxide fuel cell durability. *Journal of Power Sources*, 182(2):400–412, 2008.

[133] P. Young, T. Beresford-West, S. Coward, B. Notarberardino, B. Walker, and A. Abdul-Aziz. An efficient approach to converting three-dimensional image data into highly accurate computational models. *Philosophical Transactions of the Royal Society of London A: Mathematical, Physical and Engineering Sciences*, 366(1878):3155–3173, 2008.

[134] Y. Zhang, Y. Chen, Y. Lin, M. Yan, W. M. Harris, W. K. Chiu, M. Ni, and F. Chen. Electrochemical fields within 3d reconstructed microstructures of mixed ionic and electronic conducting devices. *Journal of Power Sources*, 331:167–179, 2016.